VOLCANO DEFORMATION AND SUBDAILY GPS PRODUCTS

By

Ronni Grapenthin

RECOMMENDED:
_____

_____

_____

_____
Advisory Committee Chair

_____
Chair, Department of Geology and Geophysics

APPROVED:
_____
Dean, College of Natural Science and Mathematics

_____
Dean of the Graduate School

_____
Date

VOLCANO DEFORMATION AND SUBDAILY GPS PRODUCTS

A

DISSERTATION

Presented to the Faculty

of the University of Alaska Fairbanks

in Partial Fulfillment of the Requirements

for the Degree of

DOCTOR OF PHILOSOPHY

By

Ronni Grapenthin, Dipl.-Inf.

Fairbanks, Alaska

August 2012

Abstract

Volcanic unrest is often accompanied by hours to months of deformation of the ground that is measurable with high-precision GPS. Although GPS receivers are capable of near continuous operation, positions are generally estimated for daily intervals, which I use to infer characteristics of a volcano's plumbing system. However, GPS based volcano geodesy will not be useful in early warning scenarios unless positions are estimated at high rates and in real time.

Visualization and analysis of dynamic and static deformation during the 2011 Tohoku-oki earthquake in Japan motivates the application of high-rate GPS from a GPS seismology perspective. I give examples of dynamic seismic signals and their evolution to the final static offset in 30 s and 1 s intervals, which demonstrates the enhancement of subtle rupture dynamics through increased temporal resolution. This stresses the importance of processing data at recording intervals to minimize signal loss.

Deformation during the 2009 eruption of Redoubt Volcano, Alaska, suggested net deflation by 0.05 km^3 in three distinct phases. Mid-crustal aseismic precursory inflation began in May 2008 and was detected by a single continuous GPS station about 28 km NE of Redoubt. Deflation during the explosive and effusive phases was sourced from a vertical ellipsoidal reservoir at about 7-11.5 km. From this I infer a model for the temporal evolution of a complex plumbing system of at least 2 sources during the eruption. Using subdaily GPS positioning solutions I demonstrate that plumes can be detected and localized by utilizing information on phase residuals.

The GPS network at Bezymianny Volcano, Kamchatka, records network wide subsidence at rapid rates between 8 and 12 mm/yr from 2005-2010. I hypothesize this to be caused by continuous deflation of a $\sim$30 km deep sill under Kluchevskoy Volcano. Interestingly, 1-2 explosive events per year cause little to no deformation at any site other than the summit site closest to the vent. I derive evidence for a very shallow source, likely within the edifice. This work shows that network design and individual plumbing system characteristics affect the ability to detect motion on subdaily and even weekly time scales, which stresses the importance of network scale considerations.

Table of Contents

List of Figures

List of Tables

List of Other Materials

List of Appendices

Acknowledgements

Hidden away in the trusty corner of my cubicle, I realize that my fifth Alaskan Summer has begun outside and my dissertation is about to be concluded. People always seem to say this, but time indeed passed rather quickly – which must mean it was worthwhile: packed with work and adventure, many new friends and things I never thought I'd get into. Thanks to all who contributed to this wonderful and memorable time of my life!

I somewhat stumbled into this situation. My transformation from Computer Scientist to Geophysicist started with an exchange semester in Iceland in 2005 (which really should have been Sweden, but there weren't any Erasmus spots available, so I picked the only other available Scandinavian country . . . how fortunate!) during which Páll Einarsson and Thor Thordarson taught an amazing Volcanology course. They got me hooked on this business with red hot stuff, ash plumes, explosions, and bombs of volcanic nature. During a follow-up visit for project work in 2006, Freysteinn Sigmundsson's support and incredibly enthusiastic work attitude reeled me fully into the pool of Geophysicists. The openness and support of my friends and collaborators in Iceland during this time was outstanding and made me feel very welcome in the community. So much that I thought I should pursue a Ph.D. – in Alaska. Thanks to Freysteinn, Sigrún, Þóra, Dóri, Benni, Birgir, Björg, Alex, Niels, Tanja for the excellent time, and continued collaboration and friendship! Additional thanks to Björg for housing me all those times I got a chance to come back!

Here in Alaska I owe a lot to my advisor, Jeff Freymueller. He gave me all the freedom and support I could ever want to explore ideas, run into walls, and develop independent thinking. At the same time he pushed me to follow through with the less exciting stuff and guided me towards the accomplishments of my goals. Of course, Jeff also taught me how to travel: Fairbanks – Petropavlovsk-Kamchatskii via Moscow $\times$ 4 will be a good story for decades to come. I also want to thank the rest of my committee: Chris Larsen, who helped me with kinematic GPS processing, Doug Christensen who explained seismology to me and keeps the social life of the department going, and Mike West, who helped with more seismology, and was always generous giving advice on academic and real-life issues. I also learned a lot from the many, welcoming colleagues at the Alaska Volcano Observatory, north and south – a great environment to approach volcanoes from so many different disciplines.

Although not on my committee, I am deeply indebted to Pavel Izbekov. His office was always open for me to storm into and find very honest opinions on my sometimes rather ridiculous ideas on volcanism. His enthusiasm about petrology and volcanology is a great inspiration and I treasure the discussions we had in the field while he carried my equipment. Many of the adventures during the last 5 years would never have happened without Pavel's exceptional commitment to students and field work: "Болшое спасибо!"

The visits to Kamchatka were always outstanding! I want to thank Sergey Serovetnikov, Slava Pilipenko, Sergey Ushakov, Oxana Evdokimova, and Oksana Krivomazova, and of course Pavel Izbekov for making field work such a grandiose experience. The times at Bezy, Karymsky, Mutnovsky and Gorely were spectacular and I hope I get to go back one day! Thanks to all the friends I made at the various cabins. I keep some very special memories – like invading Camp Kaspersky dressed up as pirates. "На жизнь!"

Before I entered graduate school I had the grandiose plan to develop my own course while working on my degree. Little did I know how uncommon this is! Yet, all the stars aligned and I got my wish fulfilled. I taught "Beyond the Mouse: Programming for Geoscientists" 4 times in various incarnations. This was a fantastic experience and I am very grateful for all the support from Jeff Freymueller (who taught a few lectures himself and kept the bureaucracy in order). The Department of Geology and Geophysics found financial support for this experiment, and Branden Christensen voiced the need for some instruction in this field (fortunately very loudly) and helped organizing the initial seminar series. Glenn Thompson, Celso Reyes, and Matt Gardine volunteered time to teach some of the initial seminars and provided their materials for later lectures. Bernie Coakley deserves special thanks for supporting this from the Department side and providing his insights into GMT since version 0.1. Bernie also provided invaluable critisism on the first draft of the Eos Forum piece on the experience ("You're trying to be too clever - write how it actually happened!")

I am thankful for all the help in the office, fun times outside, runs up and down mountains (with or without skis), the fishing and non-fishing trips; all of which made the Alaska-time very pleasant! Yuning, Lissy, Julie, Max, and Summer made for an excellent Geodesy Lab. The West-Ridge-Runners kept me running whether I wanted or not. The glaciers group included me in their coffee club and – to some degree – tolerated my completely

Chapter 1

Introduction

Although beautiful and inspiring, in times of unrest volcanoes pose a hazard not only to nearby population centers, but also to global freight and civil air traffic. The global economic network is optimized to just–in–time delivery to minimize storage cost, and civil aviation industry tries to maximize the throughput of passengers and cargo on a minimal number of aircraft. This makes our society very vulnerable to any delays in aviation (e.g., Lund and Benediktsson, 2011).

Explosive volcanic eruptions often cause prolonged airport and airspace closures; the latest, most widely felt disruption was without doubt the 2010 Eyjafjallajökull eruption in Iceland (e.g., Sigmundsson et al., 2010). However, such eruptions are not rare events. Just in the year before the Eyjafjallajökull eruption the airport in Anchorage, Alaska, a large cargo hub, had to be closed several times during the 2009 eruption of Redoubt Volcano. In 2011 another Icelandic volcano, Grímsvötn Volcano, erupted and caused more – albeit not as intense – disruption of European air traffic (Donovan and Oppenheimer, 2012).

This small sample of the many explosive eruptive events during the last few years (see reports from Global Volcanism Program[1]) caused cancellation or re-routing of numerous flights due to the hazard of volcanic ash in the air. Costs for such efforts range into the millions of dollars for aircraft maintenance due to ash cloud encounters (e.g., Tuck et al., 1992); the cost of airspace closures due to Eyjafjallajökull in 2010 was estimated to be 1.7 billion US dollars (IATA, 2010). This does not take into account the impact of such events on non-aviation industry (e.g., Lund and Benediktsson, 2011, and references therein). In light of the above impacts and costs, increasing our understanding of volcanoes is of tremendous benefit to our society.

Volcanic unrest is often accompanied by deformation of the ground; eruptions are frequently preceded by hours to months of observable surface deformation (e.g., Dzurisin, 2003, and references therein). GPS based geodesy has evolved to provide sub-centimeter precision estimation of locations, and hence position change, over the last decade and is therefore a very useful tool for volcano monitoring. Although capable of near continuous operation, the most common application of GPS is the estimation of 24–hour average po-

---

[1]http://www.volcano.si.edu

sitions for each benchmark (e.g., Larson et al., 2001). It is much less common to estimate positions at the recording interval of the receivers, which are usually 30 s and less (e.g., Larson et al., 2010). Hence, the use of GPS at volcanoes so far has been limited to the study of the long-term evolution of displacements. While this strategy is helpful to detect pre-eruptive intrusions that last for days to weeks, many volcanoes show much shorter precursory activity on the order of hours (e.g., Hekla Volcano, Iceland, Höskuldsson et al., 2007). Unless positions are estimated at higher temporal resolution, GPS based volcano geodesy will not be useful in early warning. This, however, would be a waste of potential as similar analytical tools used for analysis of long-term displacements can be readily applied to analyze subdaily displacements.

This dissertation addresses the following main questions with a focus on temporal and spatial scaling of GPS:

1. Can we infer new or refine existing magma source models from the available GPS data?

2. Does GPS capture the evolution of such inferred sources during an eruption?

3. Are we missing signals in GPS data when averaging to daily solutions?

4. Can we find transient signals related to explosions and learn about conduit processes?

5. Are there scaling issues? E.g.:

   - temporal – 1 Hz vs. standard 15-30 s sampling intervals
   - spatial – near field vs. far field, i.e. shallow sources vs. deep sources

6. What monitoring products can be developed based on this work?

Chapter 2 motivates these questions from a GPS seismology perspective for the 2011 Tohoku-oki earthquake in Japan. This work, which was published in *Geophysical Research Letters*, gives examples of dynamic seismic signals and their evolution to the final static offset, which is the GPS product commonly used to estimate finite fault slip models that represent cumulative motion of a fault due to an earthquake (for the 2011 Tohoku-oki event,

e.g., Simons et al., 2011; Pollitz et al., 2011). The GPS data in Chapter 2 were processed at 30 s intervals and presented in map-view which maintains both temporal and spatial correlation of the signals. Appendix A expands on Chapter 2 and presents the same signals in 1 Hz resolution for a subset of the stations. The gain in temporal resolution enhances subtle rupture dynamics and stresses the importance of routinely processing data at recording intervals to minimize signal loss.

Chapter 3 was published in the *Journal of Volcanology and Geothermal Research* and addresses questions (1)-(4). This work presents source models derived from GPS data for the various phases of the eruption (weeks to months time scale), from which the evolution of the source system over the course of the eruption can be inferred when it is combined with observations from seismology and petrology. The subdaily records of this event contain explosion related signals that are linked to volcanic plumes that interfere with the signals from the GPS satellites, which provides an example for question (3). This volcanic plume related work is furthered in Appendix B, which presents results of different processing strategies, that would allow not only for plume detection but also to gain more insight in plume properties. Appendix C adds an example of clear short-term pre-eruptive deformation for the 2011 Grímsvötn eruption in Iceland resolved in the 1 Hz GPS record, which addresses questions (2) and (3) and provides evidence that GPS qualifies as an early warning tool for certain volcanoes.

Chapter 4 was submitted for publication in the *Journal of Volcanology and Geothermal Research* and shows that although a volcano may be very active with 1-2 explosive eruptions per year, the deformation record does not have to be equally dynamic. The tools developed in Chapter 3 do not produce useful results and the only signals recorded at Bezymianny Volcano, Kamchatka, turn out to be long-term, long-wavelength subsidence of the entire network, and slight explosion-related deformation in the north component at the summit station. This addresses question (4) and (5) as spatial scaling becomes an issue with these signals: The network samples the broad subsidence very localized, yet most stations are too far away from the summit to record shallow co-eruptive source dynamics.

Chapter 5 summarizes the findings of this dissertation and presents an outlook on problems that need to be investigated in the future to improve on this work.

Appendix D, which was published in *Eos Transactions of the American Geophysical Union*,

does not directly connect to the questions above. Rather, it represents a plea to Earth Science Departments (and other departments where work on large data sets is necessary) to establish specific courses that teach their students how to instruct a computer to do the heavy lifting in data analysis and presentation of results such that they are able to effectively explore their growing data sets and connect them to observations from other fields.

Bibliography

Donovan, A. M., Oppenheimer, C., 2012. The aviation sagas: geographies of volcanic risk. The Geographical Journal 178 (2), 98–103.

Dzurisin, D., 2003. A Comprehensive Approach to Monitoring Volcano Deformation as a Window on the Eruption Cycle. Reviews of Geophysics, 1–29.

Höskuldsson, A., Óskarsson, N., Pedersen, R., Grönvold, K., Vogfjörd, K., Ólafsdóttir, R., 2007. The millennium eruption of Hekla in February 2000. Bull. Volcanol. 70 (14), 169–182.

IATA, 2010. IATA Economic Briefing: The Impact of Eyjafjallajokull's Volcanic Ash Plume.

Larson, K. M., Cervelli, P., Lisowski, M., Miklius, A., Segall, P., Owen, S., 2001. Volcano monitoring using the Global Positioning System: Filtering Strategies. Journal of Geophysical Research 106, 1–12.

Larson, K. M., Poland, M., Miklius, A., 2010. Volcano monitoring using GPS: Developing data analysis strategies based on the June 2007 Kilauea Volcano intrusion and eruption. Journal of Geophysical Research 115, B07406.

Lund, K. A., Benediktsson, K., 2011. Inhabiting a risky Earth - The Eyjafjallajokull eruption in 2010 and its impacts. Anthropology Today 27 (1), 6–9.

Pollitz, F. F., Bürgmann, R., Banerjee, P., 2011. Geodetic slip model of the 2011 M9.0 Tohoku earthquake. Geophys. Res. Lett. 38, L00G08.

Sigmundsson, F., Hreinsdóttir, S., Arnadottir, T., Hooper, A., Pedersen, R., Roberts, M. J., Oskarsson, N., Auriac, A., Decriem, J., Einarsson, P., Hensch, M., Ofeigsson, B. G., Sturkell, E., Sveinbjornsson, H., Feigl, K. L., 2010. Eyjafjallajokull Intrusion triggering of the 2010 explosive eruption. Nature 468, 426–432.

Simons, M., Minson, S. E., Sladen, A., Ortega, F., Jiang, J., Owen, S. E., Meng, L., Ampuero, P., Wei, S., Chu, R., Helmberger, D. V., Kanamori, H., Hetland, E., Moore, A. W., Webb, F. H., 2011. The 2011 Magnitude 9.0 Tohoku-Oki Earthquake: Mosaicking the Megathrust from Seconds to Centuries. Science 332, 1421–1425.

Tuck, B. H., Hustkey, L., Talbot, L., 1992. The Economic Consequences of the 1989-90 Mt. Redoubt Eruptions.

Chapter 2

The Dynamics of a Seismic Wave Field: Animation and Analysis of Kinematic GPS Data Recorded during the 2011 Tohoku-oki Earthquake, Japan[1,2]

Abstract

During rupture, earthquakes induce permanent and dynamic ground displacements that can be measured by GPS. More than 1200 continuous GPS stations distributed throughout Japan recorded the displacements due to the March 11, 2011, $M_w 9.0$ Tohoku-oki earthquake. We animate these data, which shows the growth of the earthquake rupture over time and illustrates differences of earthquake magnitude through two smaller aftershocks. We also identify dynamic ground motion due to S-waves (body waves), Love waves and Rayleigh waves (surface waves) in this data set. Real time availability of such displacements could be of great use in earthquake response and tsunami warning, and to some degree in earthquake early warning. We find that the length of the ruptured fault can be approximated from displacements which could allow rapid identification of areas prone to large aftershocks. We outline a method that integrates real time displacements into an earthquake alarm system. The animated displacements in map view are easily understandable by specialists and non-specialists alike and hence provide a valuable education and outreach tool.

2.1 Introduction

Earthquakes displace the ground during rupture and create seismic waves, which induce dynamic displacements that travel around the globe. Within the last decade, high-rate kinematic Global Positioning System (GPS) methods (*Larson et al.*, 2003) have been developed to provide ground displacements complementary to seismic records. However, due to sparse station coverage, such data are traditionally presented as time series for a few GPS stations, which neglects spatial correlation in the signal presentation. The uniquely dense Japanese GPS Earth Observation System (GEONET)(*Sagiya*, 2004) pro-

---

[1]Published as: Grapenthin, R. and J. T. Freymueller (2011), The dynamics of a seismic wave field: Animation and analysis of kinematic GPS data recorded during the 2011 Tohoku-oki earthquake, Japan, *Geophys. Res. Lett.*, *38*, L18308, doi:10.1029/2011GL048405.

[2]Chosen as GRL Editors' Highlight / AGU Research Spotlight: Schultz, C. (2011), Earthquake data visualization shows ground motion in real time, Eos Trans. AGU, 92(49), 464, doi:10.1029/2011EO490013.

vided an impressive amount of data for the 05:46:23 UTC, March 11, 2011, M_w9.0 Tohoku-oki earthquake (source: USGS[3]). Here, we visualize and analyze the vector field of directly measured dynamic and permanent displacements induced by this event and recorded by GEONET. The result is a map view movie of an earthquake (Figure 2.1, Animations S1-S3), which proves to be a valuable education and outreach tool as confirmed by early users and from our own experience.

Basic tools such as direct visualization of displacements in near real time can be crucial to estimate characteristics of big earthquakes such as magnitude and rupture length, which helps to identify regions that might be subject to large aftershocks. Furthermore, automated analysis of real time displacements could be useful in: (1) earthquake response to create products such as damage potential maps; (2) earthquake early warning (*Fleming et al.*, 2009; *Crowell et al.*, 2009), when geocorrelated permanent displacements near the epicenter are used for event detection; and (3) tsunami warning as the onshore static deformation field indicates changes in topography and bathymetry as soon as the body waves have passed (Figure 2.1B,C, Animation S3) and hence informs about the tsunami generation mechanism.

2.2   Data and Processing

The GEONET raw data is currently not generally accessible from outside Japan, but the immediate implementation of the Tohoku-oki event website (GEO Supersites[4]) allowed us to access three-dimensional 30 s kinematic position estimates produced by the ARIA project (*Simons et al.*, 2011) for all available GEONET sites. This open process enhanced opportunities for scientific collaboration and allowed for timely outreach to the general public.

The ARIA team used the GIPSY software developed at NASA's Jet Propulsion Laboratory (JPL) to compute the kinematic displacements based on RINEX data provided to Caltech by the Geospatial Information Authority (GSI) of Japan. They provided a time series of displacements relative to the first epoch solution (2011/03/11, 00:00:00 UTC). We visualized displacements from 05:40:00-06:25:00 UTC using the complete dataset except

---

[3]http://earthquake.usgs.gov/earthquakes
[4]http://supersites.earthobservations.org/sendai.php

stations 0197, 0228, 0550, and 0616, which appear noisy throughout the day. We reduced site specific jitter resulting from poorly determined epochs by setting the displacements at a station to zero if the provided uncertainty of an epoch position exceeds 0.25 m. The displacements were then reformatted for compatibility with the Generic Mapping Tools (GMT) (*Wessel and Smith*, 1995), which we used to create the individual frames of the animations. The resulting Postscript files were rasterized using ImageMagick's convert program. We cloned each frame 7 times to support the minimum frame rate of 12 frames per second required by some video players as well as to accommodate our wish for a slow animation. We concatenated the frames into animations with the software mencoder using the video codec msmpeg4v2 at a bit rate of 5320 kb. The movies were converted from avi to mp4 (Quicktime) format with the ffmpeg software. All software used is freely available and licensed under the GNU General Public License version 2. Generating a single rasterized frame takes about 2 seconds on a laptop with a 2.2 GHz Duo Core CPU processor and 2 GB memory. Half of this time is required for rasterization of the Postscript file. This is acceptable for the used 30 s solutions, but some optimization is necessary when 1 Hz real time data are used.

In addition to animating the filtered data (Animation S1), which could be done in near real time, we provide two animations in which we remove the permanent displacements due to the mainshock (Figure 2.1A) at 05:55:30 UTC (Animation S2) and 05:49:30 UTC (Animation S3), respectively. These highlight aftershocks and seismic wave propagation, respectively, but potentially introduce distortions in the near field while permanent displacements are still accumulating. We advise comparison to Animation S1 before drawing conclusions about near-field features from Animations S2 and S3.

2.3   Results

Some key features of the animations are illustrated in Figure 2.1. The permanent displacements (Figure 2.1A) caused by the M_w9.0 main shock are subtracted in Figure 2.1B,C to show vertical (Figure 2.1B) and horizontal (Figure 2.1C) dynamic displacement fields from 187 s–367 s after rupture initiation. We can clearly identify S-waves (body waves), Love waves and Rayleigh waves (surface waves) (Figures 2.2, 2.3). The S-waves are best resolved in the horizontal field (Figure 2.2A). They radiate outwards from the source at an

apparent velocity of 6-8 km/s in a swath of about 250 km width. This apparent velocity is not the actual S-wave propagation velocity ($\sim$4.5 km/s in upper mantle), as the waves arriving at each point on the surface took different paths. However, from these values we can infer that each individual point is affected by large amplitude S-waves for at least 31-42 s while the wavetrain traverses Japan in 4.5-5 minutes. The S-wave duration of 31-42 s may be underestimated as the high moment-rate lasted about 50 s (*Ide et al.*, 2011), which should be proportional to body-wave excitation. Some stations may be in a phase similar to their reference position, so a single snapshot at a 30 s sample rate may not accurately show the full extent of the region where S-wave amplitudes are large. The Love wave that follows is also clearly resolved in the horizontal field. It displays a distinctive wave-front defined by its 'snake like' motion transverse to the direction of wave propagation. This wave-front travels about 270 km in 60 s at an estimated velocity of 4-5 km/s (Figure 2.2B). As Love waves cause horizontal displacements only, GPS data naturally separate them from the slower Rayleigh waves (Figure 2.2B-D), which induce ellipsoidal particle motion up and parallel to the propagation direction. We estimate the Rayleigh wave to be about 0.35-0.42 km/s slower than the Love wave, which traveled 130 km farther in 367 s (Figure 2.2D). The surface waves take about 8.5-9 minutes to fully traverse Japan.

The animations also capture the main rupture in 6 frames (Figure 2.3), which show the displaced region growing to the south as the rupture propagates. Surface displacement on land begins between 37 s and 67 s after rupture initiation (Origin time USGS[5]). Large displacements are not observed until the epoch 97 s after rupture initiation. Since the propagation delay from the hypocenter to the nearest coastal sites is only about 15-20 s, we infer that the earthquake did not involve large slip for several tens of seconds after rupture initiation. This is confirmed by *Ide et al.* (2011), who show that the moment rate increased steeply from about 40-50 s after the rupture onset. At 67 s we see maximum horizontal and vertical offsets of 1.17 m and -0.31 m, respectively. Over the following 150 seconds the permanent displacement builds up to its maximum final displacement of 4.04 m of horizontal displacement and about 0.69 m of subsidence (see final displacements at 517 s in Figure 2.1A). Further details of the rupture process could be resolved from higher rate (e.g., 1 Hz) displacements. The induced dynamic displacements separate spatially from

[5]http://earthquake.usgs.gov/earthquakes

the permanent displacements from 217 s onwards, which shows that the significant permanent displacements are settled at the time the body waves have moved though and the rupture zone is defined (Figure 2.1, Animation S3). At this time the NE and SW locations where the dynamic displacements intersect the coastline give an upper bound on the ruptured fault length. From this we can infer that the rupture process finished between 187 and 217 s and estimate a rupture zone length of about 530 km which compares well with *Simons et al.* (2011) who model a slip zone of about 500 km length. Given the rupture length and endpoints, a rapid inversion for rupture width and average slip, and thus seismic moment, is simple and could be done automatically.

Following the main rupture at least two other events induce visible displacements (Figure 2.2E,F). At 06:09:30 UTC, 23:07 minutes after the M_w9.0 event, a small earthquake (likely M_b6.7, NEIC catalog[6]), induces significant horizontal displacement at several sites 200 km north of the main shock. This dynamic horizontal displacement reduces to considerably smaller, yet visible, permanent displacement in the next frame. The second event is M_w7.9 which ruptured at 06:15:40 UTC offshore of Tokyo. Identification of individual wave patterns is difficult, but S-waves and surface waves clearly propagate across the network.

2.4   Discussion and Conclusions

We visualized for the first time the vector field of displacements induced by a large earthquake and associated aftershocks. We showed that map view visualizations of displacements recorded by dense, high-rate GPS networks can be used to directly estimate key characteristics of great earthquakes in near real-time. These time series of positions show the development of permanent and dynamic displacements related to long-period seismic waves. We acknowledge that some variations due to shorter-period seismic waves are likely aliased into the time-dependent displacement field and also note that seismic instrumentation is indispensable to fully understand the dynamics of events like the Tohoku-oki earthquake. We do, however, suggest automation of our approach and inclusion of the presented first order methods into subduction zone monitoring where dense GPS instrumentation exists. We hope the presented work will foster support of the work needed

---

[6]http://earthquake.usgs.gov/earthquakes/eqarchives/epic

to expand dense GPS instrumentation along subduction zones following the example of Japan, Cascadia and California. Real time availability of these data is particularly important as induced ground displacements could be of great use in tsunami warning (*Blewitt et al.*, 2006, 2009), earthquake response, and perhaps earthquake early warning. In particular, the permanent displacements measured by GPS do not saturate at some maximum magnitude, as do the magnitude estimates typically used for rapid magnitude estimation in seismology. The feasibility to use real time GPS for such applications has been discussed and demonstrated in a number of studies. Using only real-time products for the analysis of the 2003 Tokachi-oki earthquake, *Yamagiwa et al.* (2006) demonstrate positioning precision on the order of a few centimeters. *Genrich and Bock* (2006) show that instantaneous, single-epoch positioning using ultra-rapid orbits yields horizontal precision of 6–10 mm and vertical precision of 40–50 mm for inter-station baselines of tens of kilometers, clearly demonstrating the fit of GPS for seismology applications. Such measured displacements displayed in map view in near real time give a direct first order estimate of the affected area. Convolution of dynamic and static displacements with functions that express, for example, ground composition or population density, will result in products similar to the Shake Maps created by the USGS which can be used in hazard response.

The map view display of displacement data allows for instantaneous estimates of rupture duration (smaller than 217 s) and ruptured fault length (smaller than 530 km). The latter estimate is important to identify areas prone to large aftershocks as shown by the two strongest near coast aftershocks recorded within 30 minutes of the main event (Figure 2.2E,F). This length estimate, of course, scales with distance between landmass and thrust fault zone and will always be an overestimate when not corrected for this distance.

After the body waves have moved through the near field at about 217 s, well before the tsunami hit the coast, we could have known that Japan's east coast subsided up to 60 cm, which puts the hinge line that separates subsidence from uplift offshore. This almost instantly suggests a complex mix of subsidence and uplift of the sea floor, which gives rapid insight into the tsunami potential as a large amount of energy went into water column displacement. The vertical displacements presented in map view also allow for a fast identification of the parts of the coastline now exposed to a raised mean sea level. Such changes in coastal topography have immediate implications for tsunami hazard mitigation

as protective levees were effectively lowered by up to 60 cm. Furthermore, the M_{wp} earthquake magnitude scale used in some tsunami warning applications saturates at M_{wp} 8.0, but visualization of real-time GPS displacements would provide an immediate visual and quantitative indication of the difference between an earthquake of that size and an M_w9.0 event (Figure 2.2E,F). From this it would have been obvious that the initial estimate of M_w7.9 calculated about 3 minutes after onset of the rupture was a gross underestimate.

Automation of our manual quantitative assessment is not hard to imagine. Combined with a self-organizing ad-hoc network approach as described by *Fleming et al.* (2009) a displacement based alarm system could be implemented. Alarm triggering would depend on evaluation of spatial and temporal consistency of the data. For temporal consistency a station needs to compare its current position to its displacement history, i.e., continuously increasing displacement in one direction between epochs suggests a physical process rather than noise. In parallel to this spatial consistency can be evaluated, which means a station could negotiate with its nearest neighbors whether they experience comparable position changes. Once consistency in displacements is assured an alarm can be triggered across the network providing redundancy to seismically triggered alarms.

Lastly, showing three earthquakes of different magnitudes in one animation creates an accessible visualization of the meaning of earthquake size. Because displacements presented as vector fields in map view are more intuitive than velocities or accelerations shown in seismograms, visualizations like these can increase the understanding of earthquake mechanics and inform and educate policy makers, educators, and scholars alike.

which enabled timely data and result exchange in the days and weeks after the earthquake.
Financial support by the Alaska Volcano Observatory is acknowledged.

Bibliography

Blewitt, G., C. Kreemer, W. C. Hammond, H. P. Plag, S. Stein, and E. Okal (2006), Rapid determination of earthquake magnitude using GPS for tsunami warning systems, *Geophys. Res. Lett.*, *33*, L11,309, doi:10.1029/2006GL026145.

Blewitt, G., W. C. Hammond, C. Kreemer, H.-P. Plag, S. Stein, and E. Okal (2009), GPS for real-time earthquake source determination and tsunami warning systems, *J. Geod.*, *83*, 335–343, doi:10.1007/s00190-008-0262-5.

Crowell, B. W., Y. Bock, and M. B. Squibb (2009), Demonstration of Earthquake Early Warning Using Total Displacement Waveforms from Real-time GPS Networks, *Seismological Research Letters*, *80*(5), 772–782, doi:10.1785/gssrl.80.5.772.

Fleming, K., M. Picozzi, C. Milkereit, F. Kühnlenz, B. Lichtblau, J. Fischer, C. Zulfikar, and O. Özel (2009), The Self-organizing Seismic Early Warning Information Network (SOSEWIN), *Seismological Research Letters*, *80*(5), 755–771, doi:10.1785/gssrl.80.5.755.

Genrich, J. F., and Y. Bock (2006), Instantaneous geodetic positioning with 10 - 50 Hz GPS measurements: Noise characteristics and implications for monitoring networks, *Journal of Geophysical Research*, *111*, B03,403, doi:10.1029/2005JB003617.

Ide, S., A. Baltay, and G. C. Beroza (2011), Shallow Dynamic Overshoot and Energetic Deep Rupture in the 2011 Mw 9.0 Tohoku-Oki Earthquake, *Science*, *332*, 1426–1428, doi:10.1126/science.1207020.

Larson, K. M., P. Bodin, and J. Gomberg (2003), Using 1-Hz GPS Data to Measure Deformations Caused by the Denali Fault Earthquake, *Science*, *300*, 1421–1424, doi:10.1126/science.1084531.

Sagiya, T. (2004), A decade of GEONET: 1994-2003 - The continuous GPS observation in Japan and its impact on earthquake studies, *Earth Planets Space*, *56*, xxix–xli.

Simons, M., et al. (2011), The 2011 Magnitude 9.0 Tohoku-Oki Earthquake: Mosaicking the Megathrust from Seconds to Centuries, *Science*, *332*, 1421–1425, doi:10.1126/science.1206731.

Wessel, P., and W. H. F. Smith (1995), New version of the Generic Mapping Tools released, *Eos Trans. AGU*, *76*(33), 329, doi:10.1029/95EO00198.

Yamagiwa, A., Y. Hatanaka, T. Yutsudo, and B. Miyahara (2006), Real-time capability of GEONET system and its application to crust monitoring, *Bull. Geogr. Surv.*, *53*, 27–33.
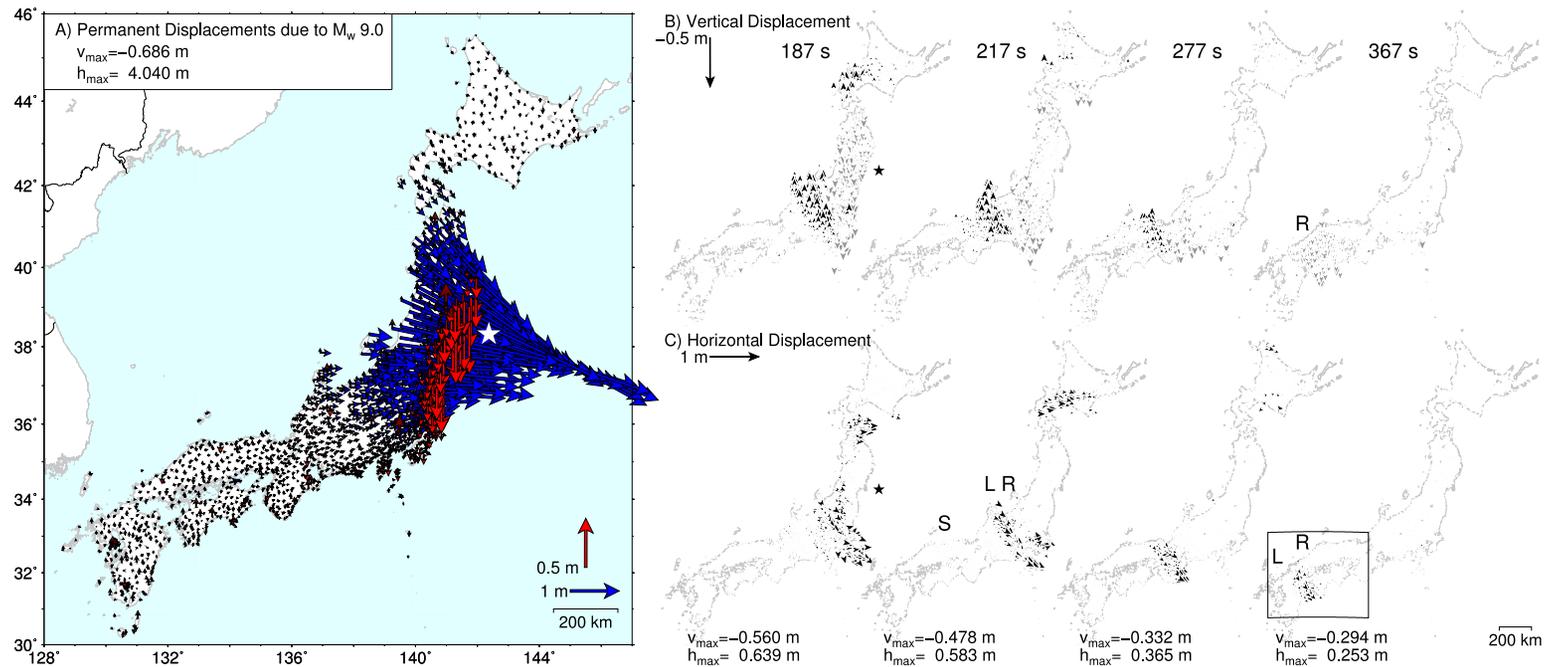
Figure 2.1: Permanent and dynamic displacements due to the $M_w 9.0$ Tohoku-oki Earthquake. (**A**) Permanent displacements after the $M_w 9.0$ earthquake (star marks epicenter). Maximum horizontal (blue arrows) and vertical (red arrows) displacements are given in inset. Vertical displacements are almost all subsidence, which means that all slip-induced uplift occurred off-shore. These permanent displacements are subtracted from panels (B) and (C) to highlight the propagating seismic waves. (**B,C**) Vertical displacements (black: uplift, gray: subsidence) and horizontal displacements from 187-367 s after rupture initiation. Note that the full rupture took about 180 s (Figure 2.3). 'S', 'L', and 'R' indicate S-wave, Love wave, and Rayleigh wave, respectively. For each time maximum horizontal and vertical displacements are given below the respective panel. Box in (C) indicates the location for Figure 2.2A-D.
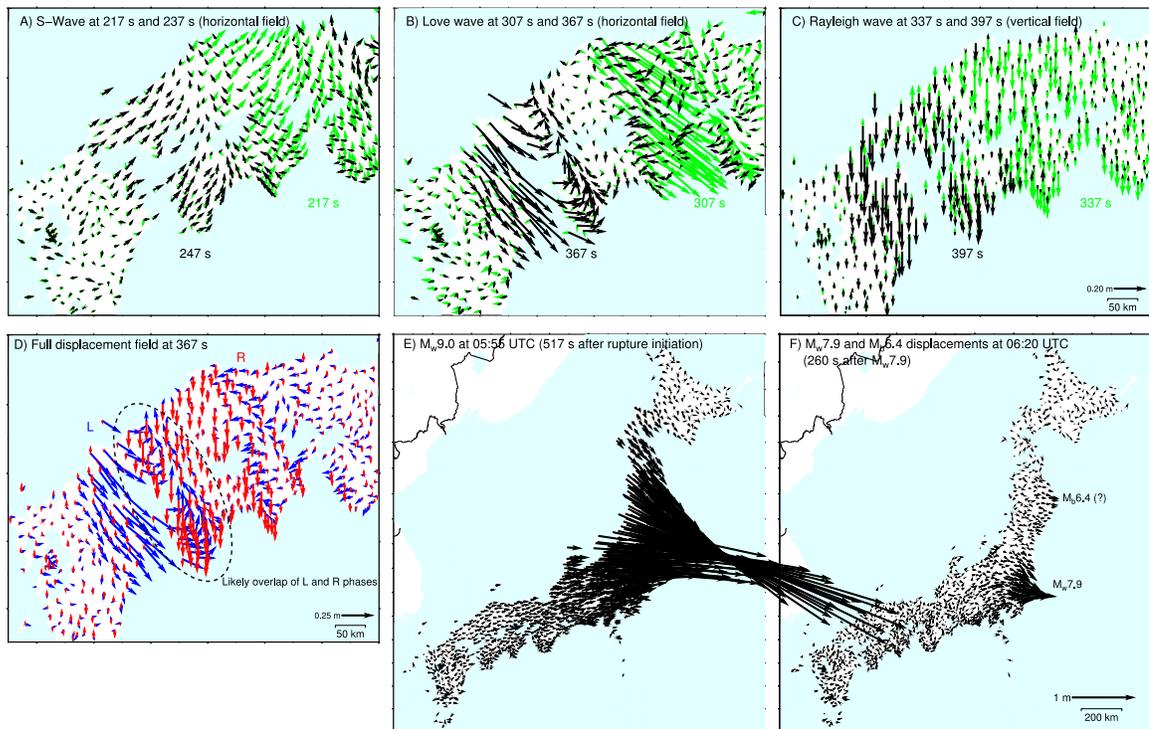
Figure 2.2: (**A-C**) 3 wave patterns observed in the kinematic GPS data. The 3 observed wave patterns as they propagate through the box in Figure 2.1C; times are relative to origin time. Early records are green, later ones are black. (**A**) S-wave. (**B**) Love wave; note the well-defined displacements perpendicular to the propagation direction. The trailing smaller black arrows indicate the following Rayleigh wave (see Figure 2.2D). (**C**) Rayleigh wave. (**D**) The Love wave ('L') and Rayleigh Wave ('R'). Horizontal displacements (blue) and vertical displacements (red) 367 s after rupture initiation (location indicated in Figure 1C). The Love wave ('L') dominates horizontal motion inducing displacements perpendicular to the propagation direction (SW). The Rayleigh wave ('R') dominates vertical motion inducing slight horizontal displacements parallel to propagation direction. We might see a superposition of surface waves due to multiple source asperities (dashed ellipse). (**E-F**) Permanent horizontal displacements of the earthquakes. (**E**) $M_w9.0$ (**F**) $M_w7.9$ and $M_b6.7$. Displacement in (F) is subtracted.
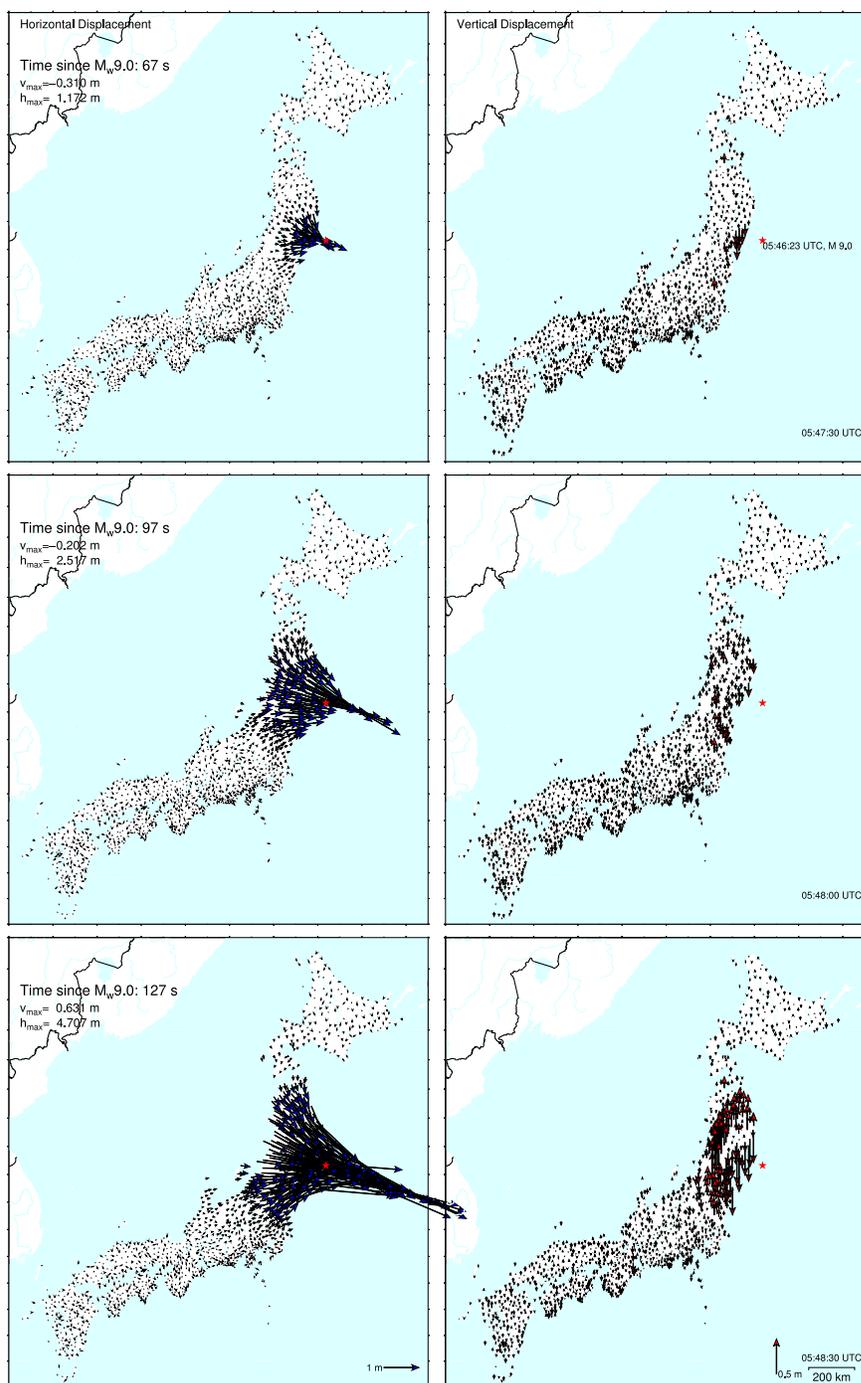
Figure 2.3
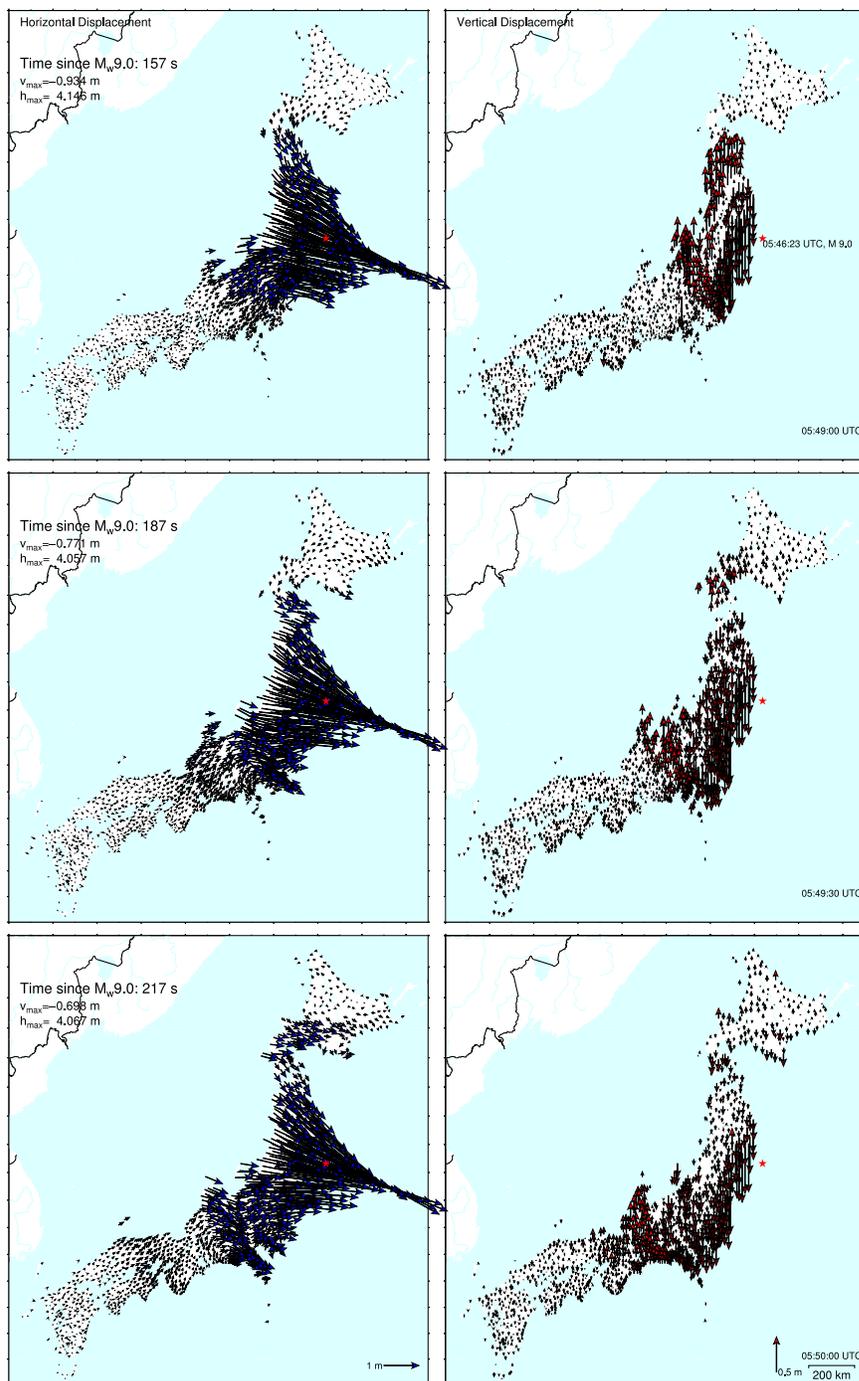
Figure 2.3: continued.

Figure 2.3: Evolution of permanent displacements due to the M_w9.0 rupture. Times are given relative to rupture initiation time. Blue and red arrows are horizontal and vertical displacements, respectively. Dark and light red indicate subsidence and uplift, respectively. Maximum vertical and horizontal displacements are given in the upper left corner of each row. First displacements appear at **67 s**. At **97 s** we see hardly any vertical deformation. The surface waves might mask permanent displacements of opposite direction. The vertical displacements at **127 s** support this as the waves radiate outward inducing uplift as their first motion. Furthermore, horizontal motion reaches its maximum displacement at 4.707 m. At **157 s** and **187 s** the horizontal dynamic wave pattern clearly separate from the permanent field. Vertical displacement reaches a maximum of -0.934 m at **157 s** indicating the negative phase of the Rayleigh wave passing through. At **217 s** the fully developed permanent displacement field is completely separated from the seismic waves (compare to Figure 2.1A).

Chapter 3

Geodetic Observations during the 2009 Eruption of Redoubt Volcano, Alaska[1]

Abstract

In March 2009 Redoubt Volcano, about 160 km to the SW of Anchorage, Alaska, began its most recent explosive eruption. Deformation induced by this event was recorded by a GPS campaign network consisting of 14 benchmarks, which had been established in 1991 after the previous eruption. The network was partially reoccupied in 2001 and 2008 and no volcanic deformation was detected during that period. In response to precursory unrest starting in January 2009, the Alaska Volcano Observatory temporarily deployed continuously recording GPS instruments at four of the campaign benchmarks only days before the onset of explosive activity in March 2009.

The only GPS instrument recording continuously during the months prior to the eruption was the Plate Boundary Observatory (PBO) station AC17, about 28 km northeast of the volcano's summit. Data from this station reveals subtle motion radially outward from the volcano beginning as early as May 2008, which reversed with the onset of explosive activity.

Using simple analytical models we link the precursory activity to a point source intrusion of $0.0194\,^{0.0092}_{0.0340}$ km^3 in volume at $13.50\,^{10.17}_{17.33}$ km below sea level (bsl, superscripts and subscripts refer to upper and lower ends of confidence intervals at the 95% level). During the explosive phase about $0.05\,^{0.028}_{>0.1}$ km^3 of magma was evacuated from a prolate spheroid with its centroid at $9.17\,^{6.92}_{15.17}$ km bsl, a semimajor axis of $4.50\,^{1.25}_{>10.00}$ km length and a semiminor axis of $0.475\,^{0.3}_{>4.0}$ km. The effusive activity is inferred to come from the same source, decreasing in volume by $0.0167\,^{0.0106}_{0.0228}$ km^3.

Including observations from seismology and petrology, we hypothesize a mid-crustal two reservoir system with material sourced from >20 km flowing in at about 13.5 km depth and reheating residual material in the proposed spheroid. The mixture migrated to shallower depth (2-4.5 km bsl) and reheated material there. As this residual magma erupted, it was replaced by the material from the spheroidal reservoir at 7 to 11.5 km depth, which renders the shallow source undetectable for geodetic instruments.

In addition to long term displacements we investigate sub-daily kinematic positioning solutions and find that large, short-term positioning offsets correlate with large explosive events. Spikes in phase residuals plotted along the sky tracks of individual satellites can be related to individual plumes given favorable satellite–station–geometry, which may be of use in volcano monitoring.

3.1 Introduction

Redoubt Volcano lies in the Cook Inlet region on the northeastern segment of the Aleutian arc. It is about 160 km southwest of Anchorage inside the Lake Clark National Park and Preserve (Figure 3.1, left) and about 400 km northwest of the Aleutian Megathrust (Figure 3.1, inset), where the Pacific Plate subducts beneath Alaska. The last eruption prior to the 2009 event occurred in 1989–1990 and is described in detail in Miller and Chouet (1994). The region is volcanically active with historic eruptions at the neighboring volcanoes Augustine and Mt. Spurr.

Mt. Redoubt is a 3108 m high stratovolcano with a diameter of 10–12 km at its base at about 1200–1500 m above sea level. The ice filled summit crater is about 1.5 km in diameter and is breached to the north, which allows Drift Glacier to stretch up to 5 km down slope and into the Drift River Valley. Other smaller glaciers radiate from the summit region and dissect the volcanic edifice (Figure 3.1, left). The overall largest mass of ice in the region is the Double Glacier ice cap, which covers Double Glacier Volcano (Reed et al., 1992) on the northern side of the Drift River Valley.

In the years since the 1989–90 eruption, surface deformation studies of volcanoes have made significant contributions to the field of volcanology. We can use simple models to link surface displacements to subsurface motion of material and thus infer knowledge of the plumbing system, displaced volumes and source depths as well as the general state of the volcano. These techniques have been applied successfully to a wide range of volcanoes worldwide (Dzurisin, 2003, and references therein).

At Redoubt Volcano surface deformation is measured with high-precision GPS in a network of 14 geodetic benchmarks. InSAR based studies are generally difficult, because the glaciated, steep terrain affects signal coherence and the strongest deformation signal related to the 2009 eruption spreads over a wide region with an amplitude much smaller

than the SAR wavelength. From 1991 to 2008, 4 GPS campaigns were carried out, each occupying a set of benchmarks for a few days (Figure 3.1). In response to observed changes in activity of the volcano (e.g., Bull and Buurman, 2012, this volume) 4 temporary continuous GPS stations (DUMM, RBED, RGBY, RVBM; Figure 3.1) were installed several weeks prior to the 2009 eruption.

An overview of the event, summarizing key observations from various disciplines, is given by Bull and Buurman (2012, this volume). They separate the eruption into three distinct phases: precursory (July 2008-15 March 2009), explosive (15 March – 04 April 2009), and effusive phase (April 4–July 2009). The precursory phase is characterized by sulfur odors (Schaefer, 2012), increased melting of Drift River glacier showing collapse pits (Bleick et al., 2012, this volume) and deep seismicity beginning in December 2008 (Power et al., 2012, this volume). For the explosive phase, Bull and Buurman (2012, this volume, Figure 2) describe a complex interplay of dome growth, collapse and explosive activity, and count 28 explosions with plumes reaching up to >18 km above sea level (asl) (Table 1 in Bull and Buurman, 2012, this volume). The final, persisting lava dome was extruded during the effusive phase. Its initial rapid growth slowed during the final stage of dome building through lava intrusions into the dome (Bull and Buurman, 2012; Diefenbach et al., 2012, this volume).

Here, we present the first geodetic study of Redoubt Volcano and focus on observations during the 2009 eruption. We start with an overview of the geodetic network and data recorded at Redoubt since 1991. We investigate GPS time series for the different phases of the eruption, from which we infer source geometry, location and volume change for each phase of the eruption. Since deep pre-eruptive long period earthquakes indicate migration of material below 20 km depth (Power et al., 2012, this volume) and petrologists suggest that the magma of this event was sourced relatively shallow at 2-4.5 km bsl (Coombs et al., 2012, this volume), we are particularly interested in the question whether Redoubt presents us with a multi-source system. Furthermore, we investigate whether subdaily, kinematic positioning solutions can resolve any deformation that correlates with explosive activity.

3.2 GPS Data

3.2.1 GPS Network History and Site Description

The geodetic network at Redoubt Volcano consists of 14 markers (Figure 3.1, Table 3.1); most of these were installed in response to the 1989 eruption and were first occupied during a campaign in 1991. The network was reoccupied in 2001, 2008, 2009, and 2010 (Figure 3.1, right). No continuous sites were present in the region until 2006, when the Plate Boundary Observatory (PBO) site AC17 was installed about 28 km to the NE of the volcano near the Drift River Oil Terminal. In response to the elevated levels of seismicity at Redoubt Volcano beginning January 2009 (Buurman et al., 2012, this volume), the Alaska Volcano Observatory (AVO) converted the campaign sites DUMB, RBED, RVBR, and RGBY to temporary continuous deployments using fixed height mast installations. During this effort RVBM and DUMM were installed as secondary survey marks suitable for deployment with a mast. The original DUMB benchmark could not be found under the late February snow cover and RVBR is a benchmark on a pole, only suitable for use with a tripod. DUMM and RVBM were installed on February 27 and 28, 2009, respectively. The RBED installation did not occur until March 18, 2009; 5 days before the onset of explosive magmatic activity (Figure 3.1, right). These sites were equipped with Trimble 5700 receivers and Zephyr Geodetic antennas. The station on Gorby's Summit, RGBY, was installed on February 10, 2009 and equipped with a Trimble NetRS receiver and a Zephyr Geodetic antenna. This was the only digitally telemetered station during the 2009 eruption as it is co-located with the telemetered seismic station RDJH (Buurman et al., 2012). Data from the other temporary continuous deployments were recovered by AVO during times of relative quiescence of the volcano. The limited GPS real-time monitoring capability was completely eliminated when the RGBY antenna was hit by volcanic lightning. The lighting strike occurred within an hour of the last data download at about 10:00:00 UTC on March 23, 2009. Hence, it likely originated from the plume of event 04 (9:39 UTC) (Table 1 in Bull and Buurman, 2012, this volume).

RGBY shows inexplicable seasonal behavior similar to a sawtooth function (Figure 3.2), which may result either from site specific freezing extension of water in cracks of the bedrock, or loading deformation due to its location close to a cliff near a Double Glacier

outlet glacier (Figure 3.1, left). The setting close to a cliff could lead to amplification of horizontal motion induced by seasonal loading of the glacier. However, first order attempts to remove such a contribution by modeling snow load effects on the position of the tip of a very long antenna pole (an approximation for the cliff) failed. To mitigate any site specific effects, the new GPS site RDJH was installed on August 20, 2010; the new monument, however, shows similar seasonal motion. We therefore report displacements at RGBY in figures and tables for completeness, but we ignore these values in analyses.

3.2.2 Static GPS Data Processing

We use the GIPSY–OASIS II software (Gregorius, 1996) developed at NASA's Jet Propulsion Laboratory (JPL) to compute Precise Point Positioning solutions (Zumberge et al., 1997) for the GPS data and then generate a time series of daily positions (Figure 3.2A). We use the JPL reprocessed satellite orbit and clock products. Details on parameter estimation are given in Freymueller et al. (2008) and Freymueller and Kaufman (2010). Our processing strategy follows the general outline in Freymueller et al. (2008). Differences are that we use the IGS05 absolute antenna phase center models, GMF troposphere mapping function, and we apply ocean tidal loading based on the ocean tide model TPXO.7 computed with respect to the center of mass of the Earth system (Fu et al., 2012). We also transform site positions into the International Terrestrial Reference Frame (ITRF) 2008.

To eliminate effects of non-volcanic deformation we subtract the solutions of local reference stations from our network. We use this approach rather than a regional tectonic model because the tectonic motion in this region is complex and time-dependent, and published models leave unacceptable residual errors (Suito and Freymueller, 2009). The specific reference site varies depending on data availability during the investigated time span, but we use one of the continuous PBO stations whenever possible. We attempted using the PBO station AC59, about 100 km to the SW of Redoubt, as a reference station, because the closest continuous GPS station on the western side of Cook Inlet, AC17, shows deformation of volcanic origin during the studied period (Figure 3.2). However, seasonal signals due to snow loading are different at AC59 compared to the Redoubt network, so we can use AC59 as reference station only over short time intervals such as the explosive phase (see Section 3.4.3), or over yearly intervals when surface loads are comparable. All

models are computed relative to the appropriate reference site, so the choice of reference site mainly affects display of the data.

Displacements at the stations are estimated for time intervals by first calculating velocities from daily solutions, and using these to compute displacements over the investigated time periods (Table 3.2, exact date ranges given in Section 3.4). The uncertainties of the displacements are the scaled uncertainties of the velocities, which are based on a white noise model only. This could be too optimistic for longer time series of continuous stations as these also include colored noise. However, except for the interval from August 2008 to June 2009, the other periods are at most 56 days long and rescaling the uncertainties is not a problem. For the 9 month long period, we used only the days of the GPS campaigns at either end of the observation period for both campaign and continuous stations, which avoids this problem and also avoids the need to model the full time dependence of the continuous time series. Because of this approach, the uncertainties for the continuous GPS sites in Table 3.2 (column "Full Eruption") are roughly the same as for campaign sites.

To highlight the volcanic signals in the time series, we estimated and removed long term linear and seasonal models for the PBO and temporary continuous GPS stations. We first eliminated outliers using a 3σ test and then estimated trends based on post-eruption data from decimal year 2009.4 (May 26, 2009) to the present, shown as gray dots in Figure 3.2A. The estimated trends were extrapolated into the past and removed from the time series, which should preserve volcanic signals. For the seasonal signal we estimated annual and semi-annual cosine and sine functions; only at RGBY we allowed an additional saw-tooth function to be estimated (Figure 3.2). This highlights the different phases of deformation in relation to the eruptive phases.

3.2.3 Kinematic GPS Data Processing and Phase Residuals

We estimate kinematic solutions for the time period of the explosive phase to determine subdaily position estimates. In the kinematic solutions, we have to assume that all stations are in motion with respect to a fixed base station. To estimate kinematic station trajectories we use the software `track`, which is part of the GAMIT–GLOBK GPS processing package (Herring et al., 2010). Here, we use IGS satellite orbits (Dow et al., 2009) and estimate tropospheric delay based on the global pressure/temperature and global mapping func-

tions (Boehm et al., 2006, 2007; Kouba, 2009) implemented in `track`. As our focus for the kinematic solutions is on short term displacements in relation to individual events during the explosive period, we assume that AC17 remains stable during these events and use it as base station. This gives baselines of generally less than 40 km between rover and base station, and allows us to assume similar travel paths for the satellite signals arriving at the stations.

During kinematic processing we found systematic positioning outliers/spikes (as described in Section 3.5) which we try to explain using satellite phase residual values (RMS) as reported by the GIPSY software using a kinematic network processing mode. To plot the phase residuals, we use the `cf2sky` code by Hilla (2004); `cf2sky` visualizes `teqc` (Estey and Meertens, 1999) plot files along a satellite's trajectory in a skyplot. We modified `cf2sky` to run on a Linux platform and translated GIPSY postfit data into UNAVCO COMPACT format readable by `cf2sky`.

3.3 Modeling

3.3.1 Volcanic Source Models

Because of the limited data available and the lack of previous geodetic studies for Redoubt, we have to make several assumptions to simplify the system. Assuming the magma source is embedded in an elastic, isotropic and homogeneous half space is without doubt the most drastic simplification (Masterlark, 2007). Elasticity is justified by the short timescale of our investigation. Isotropy is justified by the symmetry seen in the data (see Section 3.4). Homogeneity is the least likely assumption, but no adequate 3D model of elastic moduli exists. Consequently, these assumptions allow us to use simple analytical models instead of heavily underdetermined systems of equations or poorly constrained finite element models.

As the data shows a radially symmetric deformation pattern (see Section 3.4), we limit our modeling efforts to radially symmetric pressure sources: a pressure point source considering topography (Mogi model) (Anderson, 1936; Yamakawa, 1955; Mogi, 1958), and prolate spheroids in a flat half-space (reference surface is shifted to sea level). Of the prolate spheroids, we test two types: a degenerate version with a semimajor axis much larger than the semiminor axes (from here on referred to as open/closed conduit) (Bonaccorso

and Davis, 1999; Segall, 2010), and a general formulation that does not assume a certain axes aspect ratio (Yang et al., 1988; Newman et al., 2006; Battaglia et al., 2012), which we keep vertical and radially symmetric, though.

The Mogi model has 4 parameters: horizontal location, depth and source strength of the pressure point source. A conversion from source strength to volume change is given, for example, by Sigmundsson (2006, Equation 5.11) assuming incompressible magma. The conduit and spheroid models share these parameters, but replace the single depth with the upper and lower ends of the vertically elongated source. The general formulation of the prolate spheroid requires solving for the length of the semiminor axis, which results in 6 free parameters for this model.

The source strength, C, of a conduit is given in terms of pressure change, ΔP, conduit radius, a, and shear modulus, G (e.g., Segall, 2010).

$$C = \frac{a^2 \Delta P}{4G} \tag{3.1}$$

To express the source strength in terms of volume change, which is what we are ultimately interested in, we first solve the fluid pressure formula in terms of ΔP:

$$\Delta P = K\frac{\Delta V}{V} \tag{3.2}$$

where K, is the bulk modulus, and V is volume.

The volume of a spheroid is $V = 4/3\pi a^2(c_2 - c_1)$ where c_1 and c_2 are upper and lower ends, respectively. If we express the bulk modulus in terms of Poisson ratio ν and shear modulus G, we get the source strength in Equation 3.1 in terms of volume change as:

$$C = \frac{1+\nu}{2(1-2\nu)}\frac{\Delta V}{4\pi(c_2 - c_1)} \tag{3.3}$$

In addition to the single source cases, we also tested cases with 2 sources using combinations of two Mogi sources as well as a shallow conduit and a deep Mogi source. However, the improvement in fit to the data for these models was never significant based on an F-Test, so we do not report results of these tests.

To find a source that fits the data, we implement a two-stage grid search over the spatial domain; although computationally more costly than other non-linear inversion methods, this is straightforward to implement and practical considering the sparse data. We start

on a coarse grid with an area of $10 \, \text{km} \times 10 \, \text{km}$ centered on the location of the final dome of the 2009 eruption (Diefenbach et al., 2012, this volume). On this grid we search for sources between 1 and $40 \, \text{km}$ depth. The grid node spacing for both, horizontal and depth search is $1 \, \text{km}$. All best fitting source models were located within a $5 \, \text{km}$ radius from the last dome, so we densified the search grid over the center area of $5 \, \text{km} \times 5 \, \text{km}$. We search again for sources between 1 and $40 \, \text{km}$ depth with a grid node spacing of $250 \, \text{m}$ in every direction. We estimate the volume change, ΔV, over the respective time period using least squares inversions for each set of geometric parameters. For conduits and spheroids we also assume that the lower end is at least one grid cell below the upper end.

The best source parameter combinations are found by minimizing χ^2 (Press et al., 2007), which compares measured and modeled displacements and provides a quantitative measure of misfit for each set of parameters. We select the best fitting source within the search space corresponding to a physically reasonable local minimum of χ^2. Confidence intervals for each parameter are picked based on $\Delta\chi^2$ values assuming one degree of freedom projected on the axis of the respective free parameter (Press et al., 2007). We give confidence intervals at the 95% level.

To reduce computational cost, we only search for a general prolate spheroid when a conduit model provides a better fit than the Mogi source and the pressure change in the conduit would be greater than lithostatic stress, as conduit models in that case would be unphysical. We search over semimajor axis lengths from $1 \, \text{km}$ to $7 \, \text{km}$ in $250 \, \text{m}$ increments and over semiminor axis lengths from $0.1 \, \text{km}$ to $1 \, \text{km}$ in $25 \, \text{m}$ increments assuming a crustal shear modulus of $26.6 \, \text{GPa}$ (Turcotte and Schubert, 2002).

3.3.2 Network Sensitivity Analysis

A question seldomly addressed when interpreting geodetic signals at active volcanoes is which signals a network cannot resolve, i.e., what is the smallest source at a given depth we can possibly infer from the data? This has important implications on the interpretations of the signals actually resolved in the data, the plumbing system of a volcano we infer from these data, and how geodetic observations can be incorporated into observations of other disciplines.

Let us assume we can detect position changes greater than $5 \, \text{mm}$ in the data, which is

just above GPS noise. We apply the Mogi model (topography corrected, see Yamakawa (1955)), the closed and open conduit model and try to find the smallest, shallowest source between 0 and 30 km depths (100 m steps) that induces detectable displacements (>5 mm). For the purpose of this analysis the source is assumed to be centered under the location of the final dome of Redoubt's 2009 eruption (Diefenbach et al., 2012). The pipes are defined as 15 km long since the lower end has only small effects on the deformation field. Figure 3.3 shows the results: each line indicates the depth-volume change dependence for each station that would produce significant displacements. Solid and dotted lines represent horizontal and vertical 5 mm iso-displacement lines, respectively. The colors are the same for each station in all three panels as indicated in the legend. The gray lines in the panels for the Mogi source and the closed conduit assist in interpreting this plot. For the Mogi source we see that a volume change of $0.01\,\text{km}^3$ at 21.6 km will induce 5 mm of vertical displacement at RBED and RVBM. No displacements above the 5 mm threshold will be recorded at any of the other stations for this source. Similarly, we can see that a volume change of $0.04\,\text{km}^3$ in a Mogi source at 15 km will induce displacements above the threshold in both components at all sites except AC17 where it only affects the horizontal component. For a closed conduit we can see that the network will not show displacements induced by volume changes smaller than $0.01\,\text{km}^3$ at depths greater than 7.5 km. An open conduit will be detected only if it is shallower than 10 km with volume changes greater than $0.02\,\text{km}^3$.

3.4 Long Term Displacements: Estimating Volcanic Source Parameters

The first GPS campaign measurements at Redoubt were done in January and June of 1991; the latter producing most of the data (Figure 3.1). Half of the receivers used in June 1991 produced questionable L2 phase data, so several sites had to be excluded. The uncertainties associated with such early GPS data are much larger than for current measurements. This complicates precise estimation of displacements to infer volcanic deformation. However, the bigger issue with these data is that only very few stations defined the global reference frame at that time. These stations also differ from those defining the current ITRF. It is possible to align the earlier measurements to the current reference frame by applying station ties between old and current stations realizing the reference frame. However, at the

time of this writing, this process could not be completed to sufficient precision. Analysis of baselines between stations shows no evidence for volcanic deformation larger than the noise level, so these data are not discussed further.

Based on the intervals of GPS data collection as well as activity of the volcano, we look at displacements over various periods of time. Bull and Buurman (2012, this volume) separated the eruption into distinct phases based on changes in activity. However, we cannot follow their dates exactly due to the times at which the GPS sites were reoccupied (Figure 3.1). For example, we define the end of the effusive phase as the time of a survey in June 2009 while Bull and Buurman (2012, this volume) define July 2009 as the end. We also see no deformation associated with the explosive event on March 15, which is why our precursory phase extends to March 22, 2009, after which juvenile material was extruded. The displacement values for the individual phases of the eruption as displayed in Figures 3.4–3.8 are compiled in Table 3.2.

3.4.1   Inter-eruptive Period (06/2001–08/2008)

We use 17 daily positioning solutions to constrain displacements with respect to CRSC and POLL (Figure 3.4) from June 19, 2001 to August 09, 2008. Neither AC59 nor AC17 was operational in 2001 and they could therefore not be used as reference stations. The maximum displacements over a period of 7 years remain below 15 mm in the horizontal and vertical with uncertainties of 4-6 mm and 12-14 mm, respectively. The spatial signature of the signal seems largely non-volcanic with local effects at POLL likely due to tectonic deformation. NUNA shows uplift, likely due to melting of the Double Glacier ice cap.

3.4.2   Precursory Phase (08/2008–03/2009)

As the first explosion containing juvenile material was reported on March 23, 2009 (Schaefer, 2012; Bull and Buurman, 2012, this volume), we consider the time between the campaign in 2008 and this event the precursory phase. At this time, however, only 4 stations of the Redoubt network were operating due to their conversion to temporary continuous sites. However, in addition to this, the continuously recording station AC17 gives a good record of far field deformation indicating the reversal of the subtle pre-eruptive deforma-

tion trend with the onset of explosive activity (see Figure 3.2).

The time series of AC17 (Figure 3.2) gives the most insight into the timing of deformation during the precursory phase. The horizontal time series shows a clear deviation from the long term trend during this phase when compared to the trend of the post-eruption data. The onset of this change in motion is hard to pin-point to a specific date, but with some confidence we estimate it to be approximately May 2008. The north component shows this change in trend more clearly than the east component; the combined horizontal motion is toward the NE. Generally speaking, this motion is consistent with a deep intrusion under Redoubt.

The vertical component at AC17 contains interesting, but mostly non-volcanic motion. Given the large distance of about 28 km from the volcano most analytical source models suggest no or very little vertical deformation at the station. Figure 3.2, however, shows small relative subsidence from the beginning of 2008 through the end of the effusive period in 2009. The mean of the detrended vertical data for AC17 (dashed line in Figure 3.2) highlights this observation. Rather than a volcanic signal, it is likely loading due to residual snow from an unusually cold summer in 2008 (Anthony Arendt, pers. comm., unpublished GRACE data). Grapenthin et al. (2006, 2010) and Pinel et al. (2007) show that surface loading hardly affects the horizontal signal when the vertical signal is this small, which assures us that the horizontal signal is volcanic. We do not have enough data to model and remove the snow effect and hence do not use vertical motion at AC17 to model volcanic effects.

We attempted to evaluate the displacements at AC17, DUMM, RBED, and RVBM during the precursory phase with respect to AC59. However, a difference in snow loading obscures the small volcanic signal in horizontal displacements at DUMM, RBED, and RVBM. We remove this by displaying these data with respect to AC17 (Figure 3.5), which results in vectors pointing radially away from the volcano consistent with influx of material underneath. Compared to the total deformation from 2001 to 2008, these displacements are significantly larger over the short period of about half a year.

Although the horizontal data suggests a volcanic source, vertical displacements are small or zero (Figure 3.5). This is likely due to seasonal loading, which is more prominent at higher elevations. Given the topography and assuming a volcanic source under the

volcano, this counteracts an inflationary vertical signal. However, as mentioned above loading does not affect horizontal motion as much as volcanic sources, which gives us confidence in the volcanic origin of this signal.

As a result of these seasonal loading effects, searching for a source using the vertical displacements (Figure 3.5) could result in a biased model. Therefore we attempt to find a source using only the horizontal displacements at DUMM, RVBM, and RBED relative to AC17. While the best fitting model for these horizontal displacements is a closed conduit (Figure 3.3), an F-Test suggests that the smaller χ^2 value for this source does not justify the additional free parameter above that of the Mogi model. Hence, we consider the Mogi source at 21.75 km bsl with a volume increase of 0.1018 km^3 about 3.25 km to the W and 4.00 km to the S of the last dome to be the best model (Figure 3.5). We will reassess this source model at a later point using data that span all phases, at this point we will also derive confidence intervals for the parameters.

3.4.3 Explosive Phase (03/2009–04/2009)

The explosive phase spans only 14 days, which renders tectonic and seasonal effects negligible, and we can use AC59 as a reference site. From the onset of the first explosion on March 23, 2009, to the last explosion on April 4, 2009, we see clear displacements at AC17, DUMM, RVBM, and RBED (Figure 3.2, 3.6). All sites move down and toward the vent, and give the largest signal of the sequence with up to 2 cm horizontal and 2.5 cm vertical motion (see Table 3.2).

We use the displacements at these 4 sites to estimate the source parameters. A closed conduit model fits better than a Mogi model. However, the inferred volume change of $\Delta V = -0.0275$ km^3 for this model suggests a conduit radius of about 38 m and a pressure change of 44 GPa, several orders of magnitude higher than lithostatic stress at these depths (0.26-0.29 GPa, (Turcotte and Schubert, 2002)). This stress regime is unphysical for a conduit, i.e. a dike would form to reduce such high pressures which a conduit could not withstand. Since the deformation pattern does not support the formation of a dike, we reject this model and search for a prolate spheroid with an unknown semimajor-semiminor-aspect ratio using an implementation provided by Battaglia et al. (2012). We limit the maximum pressure change to the lithostatic stress (when not limiting the pressure change

to lithostatic stress, the preferred source is a conduit with approx. 35 m radius, similar to the conduit model presented above). The best fitting source is offset by 0.5 km to the East from the last dome. Its centroid is at 9.17 $^{6.92}_{15.17}$ km bsl, the semimajor axis is 4.5 $^{1.25}_{>10}$ km long and the radius is 0.475 $^{0.30}_{>4.00}$ km (superscripts and subscripts refer to upper and lower ends of confidence intervals at the 95% level). The inferred volume change is -(0.05 $^{0.028}_{>0.1}$) km^3. Note that the unconstrained values in the confidence intervals indicate that the bottom end of the source is not well constrained by the data. The model fit is given in Table 3.3 and shown in Figure 3.6); an F-Test confirms that the improvement in fit warrants the use of two additional free parameters compared to the Mogi model.

3.4.4 Effusive Phase (04/2009–06/2009)

After April 4, 2009, explosive activity ceased and the final, persisting dome was built. As Figure 3.2 indicates, AC17 is moving at pre-eruptive rates after the explosive phase. Hence, we assume no volcanic signal at this station and give the displacements relative to this site (Figure 3.7). Small displacements measured at RVBM and RBED likely indicate the evacuation of small amounts of material from shallow to mid-crustal depths. However, interpretation of these displacements is difficult, as the dome emplacement creates a loading signal at the surface which in turn is also obscured by uplift due to seasonal melt as indicated by displacements at RGBY. DUMM shows the largest subsidence signal which is likely related to significant lahar deposits in the Drift River Valley (Waythomas et al., 2012, this volume). This is supported by slight up-valley horizontal motion toward the thicker deposits of the lahars.

Due to the site specific motion at DUMM and RGBY we use only RVBM, and RBED to infer source parameters. The best fitting source is a Mogi source at a depth of d =8.75 $^{3.50}_{18.00}$ km bsl with a volume change of $\Delta V = -(0.0034\ ^{0.0012}_{0.0148})$ km^3. It is horizontally offset to the North and to the East respectively by 1.75 km (Table 3.3). The conduit model gives almost as good a fit, but the upper and lower end are basically at the same depth, suggesting the extra parameter is not warranted by the data.

Since the depth of the Mogi source coincides with the centroid of the prolate spheroid inferred for the explosive phase, we test whether using the explosive source with a different volume change provides an acceptable fit. Indeed, the explosive source with a volume

change of $\Delta V = -(0.0167\ ^{0.0106}_{0.0228})\,\text{km}^3$ provides almost as good a fit ($\chi^2 = 0.7468$) as the Mogi source ($\chi^2 = 0.1470$). An F-Test shows the slight difference in χ^2 does not justify the necessary 3 additional free parameters for the Mogi model. Therefore, we favor the simple interpretation that activity continued from the source of the explosive phase (Table 3.3, Figure 3.7), given the very small amount of data for this phase.

3.4.5   Full Period of Unrest (08/2008–06/2009)

As the whole network was remeasured in a campaign in June 2009, we show the displacements between August 06, 2008, and June 10, 2009 with respect to AC59 (Figure 3.8A). The figure shows a clear volcanic signal, which suggests that the necessity to use AC17 as reference station for the 2-6 months periods investigated above was mainly due to seasonal effects. This time period, however, spans most of the intrusion of material as well as the explosive and effusive activities; the displacements, in turn, reflect the superposition of motion resolved in the individual phases above. This gives a very undifferentiated view in terms of temporal evolution of the system, but clearly shows that the motion at all stations is consistent with a net evacuation of material. To confirm the robustness of our source estimates, we compare the sum of individually modeled displacements for each phase (precursory phase: Mogi source at 21.75 km, explosive and effusive phases: prolate spheroid at 10.25 km with respective volume changes listed in Table 3.3) to the larger dataset with respect to AC59 (Figure 3.8A).

   The full model significantly overestimates the vertical displacements at all sites, predicting uplift while most sites show subsidence. The horizontal displacements are overestimated in magnitude for some and underestimated for others; the azimuths of horizontal displacements are significantly off at many sites. Generally, we can say that the combined model does not predict the measured displacements well. We believe this is mainly due to the poor constraints we have on the precursory model. To extend our data set for that period we predict the displacements at all sites using the source models for the explosive and effusive periods (Table 3.3, Figure 3.8B). Removing these predicted displacements from the data, we get residuals that contain the precursory signal plus any other non-volcanic signals (Figure 3.8C,E). While the vertical residuals in Figure 3.8C,E are likely affected by non-volcanic signals, the horizontal components at most stations indicate an inflation sig-

nal. We use almost all stations to invert this extended horizontal displacement data set for a precursory source. In addition to the routine exclusion of RGBY we also exclude the stations QRRY, POLL and DUMM from our source estimations. Horizontal motion at QRRY differs significantly in magnitude from the nearby AC17. POLL shows a different direction in the horizontal, likely because it is on the far side of the Bruin Bay Fault to the SE of Redoubt. DUMM is likely affected by a loading signal due to lahar deposits. We found that inversions that include DUMM result in a significant increase in model misfit and a preference for an unrealistically long conduit from 2.25 km to 19 km depth with a very small volume increase of just $0.0063\,\text{km}^3$.

The best fitting source using the remaining stations is a single Mogi source located at 13.50 $^{10.17}_{17.33}$ km depth, 1.25 km to the S of the last dome with a volume change of ΔV= 0.0194 $^{0.0092}_{0.0340}\,\text{km}^3$ (Figure 3.9). The fit of this model to the data residuals is shown in Figure 3.8C. Figure 3.8D shows the fit of the sum of the models for explosive, effusive, and this corrected precursory model.

Physically this source represents an injection of material at the base of the prolate spheroid inferred from the explosive data. If we proceed in a similar manner to the effusive phase and reuse the explosive source geometry varying the volume change only, we get a best fit for ΔV=0.0278 $^{0.0214}_{0.0341}\,\text{km}^3$. The fit of this model to the data residuals is shown in Figure 3.8E. Figure 3.8F shows the fit of the sum of the models for explosive, effusive, and this corrected precursory model.

The fits of both models are rather similar (χ^2_{mogi} = 14.75, χ^2_{ps} = 18.54) and not as good as for the other periods. An F-Test is not as conclusive as for the effusive phase to decide whether the slight improvement in fit of the Mogi model justifies the addition of three parameters (F(3,14,0.05) = 3.3439 > 1.1958). We therefore provide both models as possibilities – precursory inflation could have involved either the same source as the other phases, or only inflation at its lower depth limit.

3.4.6   Post Eruption (06/2009–onward)

The time series with linear and seasonal trends removed (Figure 3.2) clearly shows an absence of consistent volcanic deformation after June 2009. A small vertical offset at RBED is noted at the beginning of June 2009, likely unrelated to volcanic activity due to its rapid

nature. DUMM does not show anything similar and RVBM was not operational at this time, so the origin of this signal remains unexplained.

3.5 Short Term Displacements: Picking up Plumes

We estimate kinematic trajectories to investigate subdaily motion for the stations RVBM, DUMM, and RBED with respect to AC17. The sampling interval for most receivers during the 2009 Redoubt eruption was 30 s (AC17, RGBY sample at 15 s), which we use as the time resolution in the processing without any data decimation. Figures 3.10–3.12 show the subdaily position time series from March 22 to April 05, 2009, for these three stations. Since the presented time series spans 15 days, they clearly resolve the long-term trend due to removal of material at depth, which we investigated above (see Section 3.4.3). Here, we did not attempt to remove multipath effects (e.g., Larson et al., 2007) as we do not interpret any small amplitude features and the long time span allows us to discern whether the signals we interpret repeat approximately daily. A good example of multipath is the repeating signal in the vertical time series for RBED in Figure 3.12.

Stations RVBM and DUMM experience significant spikes or outliers that correlate very well with the timing of explosions (shown in light gray in Figures 3.10, 3.11). Of the 28 explosive events determined through seismicity (Bull and Buurman, 2012, Table 1), 17 plumes reach higher than 12 km asl. 12 of these induce position spikes at RVBM where we see no false-positives during the explosive phase. 3 plumes induce position spikes at DUMM; 1 of these is not seen at RVBM (March 28, 23:29 UTC, Event 17). At DUMM we see one false-positive indicated by arrow A in Figure 3.11 and discussed below. The remaining 11 plumes reached altitudes below 8.5 km or the plume heights could not be determined.

As shown by Houlié et al. (2005a) for Miyakejima and Houlié et al. (2005b) for Mt. St. Helens, these changes in position may be due to path delay effects induced by ash plumes injected into the atmosphere during explosions. The presence of ash increases the travel time of signals from the satellite to the station. This inhomogeneous path delay is not modeled when tropospheric path delay effects are estimated during the GPS solution and it affects satellite-station-pairs that cross the vent or ash rich plume (Houlié et al., 2005a). In cases where base station and rover are on opposite sites of the vent, an apparent baseline lengthening occurs. The RVBM time series (Figure 3.10) shows this very well as RVBM

is consistently offset to the SW and up during these events. In addition to these spikes in position at RVBM, the associated RMS values (Figure 3.10, lowest panel) reported by `track` show a spike, indicating a poor fit to the data at these times. As `track` does not report postfit phase residuals individually for each satellite, we refer to the values reported by GIPSY from kinematic network solutions that we have run in parallel (we do not show time series from these as artificial position offsets at day boundaries occur in the GIPSY solutions when using the JPL orbit and clock products).

Figures 3.13 and 3.14 show phase RMS plotted along the satellite sky tracks for March 26 and April 04, 2009, respectively. These skyplots cover the times during which event 08 and 19 occurred (see Table 1 in Bull and Buurman, 2012, this volume). In the following we first explain signals related to these events and in Figure 3.16–3.17 we cover a few anomalies where we do not see a plume related signal or see a very large non-plume induced effect. Details on how to read these figures are given in the caption of Figure 3.13.

At almost 19 km asl, the plume of event 08 on March 26, 2009 (17:24 UTC), is one of the largest of the entire eruption (Bull and Buurman, 2012; Schneider and Hoblitt, 2012, this volume). Schaefer (2012) show tephra iso–mass contours for this event extending to the S and SSE of the vent. The contours cross Cook Inlet and highest ash-fall was sampled up to the shore. Figure 3.13 shows the phase residuals for satellites visible from 17:00 to 18:30 UTC. Both AC17 and RBED show small residuals at the time of event 08. They share a similar spike for PRN 21. RVBM on the other hand shows residuals distinctly different from those at AC17 at the time of the explosion (marked in red in Figure 3.13). PRN 26 and 15 to the ENE, PRN 21 to the E and PRN 18 to the SE show large spikes coinciding with the explosion. At DUMM a residual for PRN 16 in the southern sky seems more pronounced than at the other stations. These observations are consistent with a plume indicated by the tephra dispersion map of Schaefer (2012) and remote sensing observations of the plume (Webley et al., 2012). Given the narrow footprint of this plume and its direction combined with the satellite distribution only the clear lack of signal of PRN 22 at RBED seems surprising. We believe this can be explained by its low elevation above the horizon (30°) – the satellite may have been below the thick part of the plume.

On April 04, 2009, the plume went to the SE, and left a very narrow footprint (Schaefer, 2012). Figure 3.14 shows that AC17 and RBED see about the same level in noise for all

satellites with slightly higher amplitudes in phase RMS at RBED for PRN 3, 6, and 16 in the WNW sky. The general noise characteristic for these satellites can be explained by a ridge to the WNW above RBED, which makes this station more sensitive to low angle signals. At the time of Event 19, from 13:58 to about 15:00 UTC (see Table 1 in Bull and Buurman, 2012, this volume), most of the satellites are in the southerly sky or rather low to the WNW (PRN 16) and ENE (PRN 10). Both AC17 and RBED seem to have an undisturbed atmosphere between them and the satellites (compare to station positions in Figure 3.1). RVBM and DUMM, which are to the W and ENE of the vent, however, show distinct phase residuals. At about 14:30 UTC PRN 10 shows a big spike in phase RMS at RVBM while the residual for this satellite at DUMM is similar to AC17 and RBED. Smaller spikes at about the same time are visible to the WNW (PRN 16), SSE (PRN 30), and ESE (PRN 24, 29) at RVBM. The case is rather different for DUMM which shows the largest spikes for PRN 31, 21, and 30 from the SW to the SSE. While the residuals at DUMM seem consistent with disturbance by the plume, the directionality of the large spike at RVBM seems to correspond to the location of pyroclastic density current deposits (compare Figure 4 in Bull and Buurman, 2012, this volume). If we remove the satellites from the processing when they experience plume-related path delays, we can reduce the number of outliers and reported RMS significantly (Figure 3.15) which underlines the impact of the unmodeled disturbances of the atmosphere that increase the phase delay (Houlié et al., 2005a,b).

Although we seem to pick up many plumes in the phase residuals at RVBM, a few, some of which reached significant altitudes, are 'missed.' In Figure 3.16 we show the skyplots of DUMM and RVBM for March 29, 2009, from 3:00 to 5:00 UTC spanning event 18, which erupted at 3:23 UTC with a plume reaching up to 14.6 km elevation (Schneider and Hoblitt, 2012; Bull and Buurman, 2012, this volume). Comparing the skyplots with the tephra dispersion given by Schaefer (2012), it appears that we face a very unfortunate satellite constellation with no signals traveling through the dense plume. The later, more evolved and dispersed plume seems not to affect the signal significantly.

The last skyplot in Figure 3.17 covers the time of the large outlier at station DUMM on March 23, 2009, which shows up right at the beginning of the time series in Figure 3.11 and coincides with event 01 at about 06:38 UTC (marked by arrow 'A'). RVBM and RBED are running at this time but lack this feature (compare to Figures 3.10 and 3.12). Neither

the phase residuals for individual satellites nor the RMS value in Figure 3.11 indicates anything unusual for this epoch. Here, we assume an incorrectly resolved phase ambiguity or other problems with the solution caused this spike.

The DUMM time series in Figure 3.11 contains one last distinctive feature that begins in the evening of April 3 and stops early on April 4 and remains unexplained (marked by arrow 'B'). No other station shows any similar deformation. Although an earthquake swarm occurred during this time (Buurman et al., 2012, this volume), it seems rather unlikely for this to cause such a deformation pattern. The phase residuals appear normal during this time and the pattern is inconsistent with subsurface migration of material, which we would expect to induce uplift first. Also such deformation would be seen at RVBM and RBED as well. From the amplitudes of the other days we can infer that this signal is too large to be multipath. One possible explanation is loading deformation due to a pulse of water/mud flowing down Drift River Valley.

3.6 Discussion

As explained in Section 3.2 and depicted in Figure 3.1 (right), the data situation for the 2009 Redoubt eruption is not optimal and the measured volcanic deformation signals are not particularly large. This limits our ability to discriminate between volcanic and non-volcanic signals (see, for example, Section 3.4.2), which is complicated by the lack of detailed data for processes dominating changes in hydrosphere and cryosphere in this remote region.

Splitting the signal into temporal phases affects the signal statistics (e.g., uncertainties increase), but the sum of displacements of the individual eruption phases is within the uncertainty of the displacements observed for the entire period. This argues that splitting the signal introduces only small errors in our source inversions. The difference seems to be driven mainly by the small signal to noise ratio for the precursory and effusive periods. However, we demonstrated in Section 3.4.5 that constraining the precursory source to a geometry that fits the data reasonably would have been impossible without investigating the phases separately and removing deflationary signals from the campaign data set.

While the F-Test provides a slight preference toward inflation of the prolate spheroid inferred from explosive deflation, we find the inflation of a Mogi source at the base of this

spheroid to be an equally possible scenario driving precursory deformation. The horizontal offset between the precursory Mogi source and the prolate spheroid is negligible given the small signals and superimposed, unmodeled processes as well as the small offset over depth ratio. The sum of displacements of final source models for the individual eruption phases (Table 3.3, bold) with either precursory source produces a good fit when compared to the large data set that includes displacements for the whole network spanning the time from summer 2008 to summer 2009 (Figure 3.8D,F). Consequently, we provide both models as possible explanations for deformation during the precursory phase.

The source depths for both sources have large uncertainties associated with them, but locate in the general vicinity of each other (Table 3.3). The precursory Mogi source locates somewhat below the prolate spheroid making a case for magma influx at the spheroid's base. The prolate spheroid reaches up to shallower levels. It remains speculation whether this structure actually connects to a second small reservoir at 2-4.5 km bsl as suggested by, e.g., Coombs et al. (2012, this volume) and Werner et al. (2012, this volume). If a reservoir at these depths exists, the material removed must have been smaller than the network detection limit, e.g., about 0.002 km^3 for a Mogi source (Figure 3.3), which is an underestimate as we are not taking magma compressibility into account. Immediate replacement of material evacuated from such a source would be another possible explanation for the lack of measured deformation associated with a shallow reservoir.

The lack of measured deformation from 2001 to 2008 (Figure 3.4) and apparent lack of deformation from 1991 to 2001, combined with only a small precursory inflation (Table 3.3) indicates that much of the material that erupted in 2009 had been in place prior to 2001 and probably prior to 1991. No new magma influx occurred until the onset of the precursory inflation beginning in May 2008. Although it is likely that the magma was leftover from the 1989–90 event, a more successful analysis of the 1991 GPS campaign data would be necessary to confirm this hypothesis.

Bull and Buurman (2012, this volume) derive a total volume of erupted material between 0.08 and 0.12 km^3 which is about 1.5 times more than our best fit estimate for the explosive and effusive phases (0.0667 km^3). We have to keep in mind that the uncertainty intervals for the erupted volumes are large. Using the upper limits of erupted materials we can explain up to about 0.12 km^3 of erupted material; the upper limits of magma

volume correspond to deeper limits of source depth. This indicates a very good agreement between geodetically derived volume estimates and the actual erupted volume, as our volume estimates assume incompressible magma. For Mount St. Helens, Mastin et al. (2008) report 3-4 times as much erupted volume as inferred intruded material while Voight et al. (2010) similarly suggest a ratio of 6 for incoming magma over geodetically measured reservoir wall volume change at Soufriére Hills Volcano. Bull and Buurman (2012, this volume), however, found very low vesicularity (<10 %) for the material erupted during the eruption. This reduces magma compressibility, which is mainly controlled by the presence of bubbles due to exsolved gases in the magma. These gases may have escaped in the time since emplacement in 1989–90 or even before then.

The discrepancy in volume of the final dome as derived by Bull and Buurman (2012, this volume) and Diefenbach et al. (2012, this volume) ($0.054\,\text{km}^3$) and our estimate of $0.0167\,\text{km}^3$ for the effusive phase may support the hypothesis of erupted material being drawn from a shallow 2-4.5 km reservoir (Coombs et al., 2012; Werner et al., 2012, this volume) and instantly replaced with fresh magma from depth. Decompression due to rise of the magma may account for the 3.2 times more voluminous erupted material (dense rock equivalent) at the surface, compared to the geodetically derived effusive volume.

3.7 Conclusions

This paper summarizes the geodetic observations during the 2009 Redoubt eruption and provides interpretations of these data. We investigate changes in long term time series of daily GPS positioning solutions to infer characteristics of the magmatic source feeding this event. Furthermore, we find a combination of kinematic position trajectories and satellite phase residuals plotted along satellite sky tracks as seen by individual GPS stations a helpful tool for eruption plume detection.

3.7.1 Magmatic Process

We conclude that displacements due to a source in the mid-crustal region (7 to 13 km below sea level) beneath the final dome of the 2009 eruption are seen during all stages of the eruption. No deformation was observed during 2001-2008, until the start of the precursory phase. Detected pre-eruptive intrusion of new material at depth began as early

as May 2008 at a steady rate (compare to deep long period earthquakes below 20 km beginning in December 2008 discussed by Power et al. (2012, this volume)). This culminated in a reversal of displacements during the explosive activity from March 23-April 4, 2009. Thus, the geodetic precursors to the eruption preceded any seismic precursors although they were not identified until later. Note that we do not see any deformation associated with evacuation of material before March 23, 2009, although a first explosion was reported for March 15, 2009 (Table 1 in Bull and Buurman, 2012, this volume). During the explosive phase and the effusive phase (April 5-June 1, 2009) we see a net loss of material from the storage region. This suggests that some of the erupted material was already in place or emplaced without being detected. One or all of the following processes could be responsible for this: (a) compensation of displacements due to smaller intrusions by ductile processes within the edifice, (b) intrusions of material prior to 2001, or (c) evacuation of left over material from the previous eruption in 1989–90.

Coombs et al. (2012, this volume) suggest that unerupted hot, gas-rich magma heated and mobilized magmas residing in a shallow reservoir at 2-4.5 km bsl. We see possible deformation due to removal at these depths considering the uncertainty in location of the upper end of our suggested prolate spheroid. One hypothesis (Figure 3.18) that ties deep seismicity (Power et al., 2012, this volume), petrology (Coombs et al., 2012, this volume), and our observations together is a two reservoir system in the mid- to shallow crust. Material from a diffuse magma source at 25–38 km (Power et al., 2012) flowed in at about 13 km depth beginning as early as May 2008. This reheated and remobilized residing material in the prolate spheroid from 7 to 11.5 km resulting in migration to shallower depth (2-4.5 km; Coombs et al. (2012)). By end of January beginning of February 2009 shallow seismic tremor set on (Buurman et al., 2012) suggesting reheating and remobilization of material residing in the shallower reservoir; allowing gases to pass. As this material, leftover from the 1989–90 event or earlier, extruded beginning on 23 March 2009, the mix of fresh and reheated material from the deeper stages of the system replaced it and made the shallow removal undetectable by geodesy. In this case, the resulting pressure / volume change reflects only the deeper source, which experienced net evacuation.

3.7.2 Ash Plume Detection in Subdaily Positioning Solutions

We have related systematic spikes in subdaily positioning solutions to phase delays for station–satellite–pairs that cross dense parts of volcanic plumes. While the technique of detecting ash plumes with GPS has been described before by Houlié et al. (2005a,b), this possibility seems not generally included in monitoring or data analysis efforts and is, in fact, not well explored. We show that plotting the phase residuals along the sky tracks of satellites provides easy access to plume azimuths. A high number of satellite–station pairs crossing a vent should be desired when geodetic networks for volcano deformation monitoring are designed. Kinematic solutions in near real-time could be used for plume sensing and verification and hence assist remote sensing efforts to fill some of the gaps created by slow satellite repeat times or cloud cover. From our results it is obvious that standard sampling rates of 15-30 s are sufficient to resolve the plume signal.

While intriguing, this certainly will not detect all plumes. We show that gaps in vent crossing station-satellite pairs may prohibit detection of plumes or ash concentrations may not be large enough to affect the signal significantly. Therefore, this technique should be seen as complementary to seismic and remote sensing monitoring.

Future work is necessary to determine ash concentrations and plume heights that affect the GPS signal quality significantly and hence determine detection limits. Results from such studies might in turn allow to estimate plume parameters such as density from GPS noise characteristics. Furthermore, reprocessing of any existing data set that indicates the existence of a plume with Ultra–rapid orbits or real time orbit products should clarify whether real time detection is feasible.

Bibliography

Anderson, E. M., 1936. The Dynamics of the Formation of Cone-sheets, Ring-dykes, and Caldron-subsidences. Proceedings of the Royal Society of Edinburgh 56, 128–157.

Battaglia, M., Cervelli, P. F., Murra-Muraleda, J. R., 2012. Modeling Crustal Deformation: a catalog of deformation models and modeling approaches. US Geological Survey Prof. Pap., in press.

Bleick, H. A., Coombs, M. L., Bull, K., Wessels, R., 2012. this issue. Volcano-ice interactions during the precursory phase of unrest preceding the 2009 eruption of Redoubt Volcano, Alaska. Journal of Volcanology and Geothermal Research, Special Issue on the 2009 Redoubt Eruption, in press.

Boehm, J., Heinkelmann, R., Schuh, H., 2007. Short Note: A global model of pressure and temperature for geodetic applications. J. Geod. 81, 679–683.

Boehm, J., Niell, A., Tregoning, P., Schuh, H., 2006. Global Mapping Function (GMF): A new empirical mapping function based on numerical weather model data. Geophys. Res. Lett. 33, L07304.

Bonaccorso, A., Davis, P. M., 1999. Models of ground deformation from vertical volcanic conduits with application to eruptions of Mount St. Helens and Mount Etna. J. Geophys. Res. 104 (B5), 10531–10542.

Bull, K. F., Buurman, H., 2012. An Overview of the 2009 Eruption of Redoubt Volcano, Alaska. Journal of Volcanology and Geothermal Research, Special Issue on the 2009 Redoubt Eruption, in press.

Buurman, H., West, M. E., Thompson, G., 2012. Seismicity of the 2009 Redoubt Eruption. Journal of Volcanology and Geothermal Research, Special Issue on the 2009 Redoubt Eruption, in press.

Coombs, M., Sisson, T., Bleick, H., Henton, S., Nye, C., Payne, A., Cameron, C., Larsen, J., Wallace, K., Bull, K. F., 2012. Andesites of the 2009 eruption of Redoubt Volcano, Alaska. Journal of Volcanology and Geothermal Research, Special Issue on the 2009 Redoubt Eruption, in press.

Diefenbach, A., Bull, K. F., Wessels, R., McGimsey, R., 2012. Photogrammetric monitoring of lava dome growth during the 2009 eruption of Redoubt Volcano. Journal of Volcanology and Geothermal Research, Special Issue on the 2009 Redoubt Eruption, in press.

Dow, J. M., Neilan, R. E., Rizos, C., 2009. The International GNSS Service in a changing landscape of Global Navigation Satellite Systems. J. Geod. 83, 191–198.

Dzurisin, D., 2003. A Comprehensive Approach to Monitoring Volcano Deformation as a Window on the Eruption Cycle. Reviews of Geophysics, 1–29.

Estey, L. H., Meertens, C. M., 1999. TEQC: The Multi-Purpose Toolkit for GPS / GLONASS Data. GPS Solutions 3 (1), 42–49.

Freymueller, J. T., Kaufman, A. M., 2010. Changes in the magma system during the 2008 eruption of Okmok volcano, Alaska, based on GPS measurements. Journal of Geophysical Research 115, B12415.

Freymueller, J. T., Woodard, H., Cohen, S. C., Cross, R., Elliott, J., Larsen, C. F., Hreinsdóttir, S., Zweck, C., 2008. Active Deformation Processes in Alaska, Based on 15 Years of GPS Measurements. In: Freymueller, J. T., Haeussler, P. J., Wesson, R. L., Ekström, G. (Eds.), Active Tectonics and Seismic Potential of Alaska. Geophysical Monograph. AGU, pp. 1–42.

Fu, Y., Freymueller, J. T., Dam, T. V., 2012. The effect of using inconsistent ocean tidal loading models on GPS coordinate solutions. J. Geod. 86 (6), 409–421.

Grapenthin, R., Ofeigsson, B. G., Sigmundsson, F., Sturkell, E., 2010. Pressure sources versus surface loads : Analyzing volcano deformation signal composition with an application to Hekla volcano , Iceland. Geophys. Res. Lett. 37, L20310.

Grapenthin, R., Sigmundsson, F., Geirsson, H., Árnadóttir, T., Pinel, V., 2006. Icelandic rhythmics: Annual modulation of land elevation and plate spreading by snow load. Geophys. Res. Lett. 33, L24305.

Gregorius, T., 1996. GIPSY OASIS II: How it works. self, University of Newcastle upon Tyne.

Herring, T., King, R., McClusky, S., 2010. GAMIT/GLOBK Reference Manuals, Release 10.4.

Hilla, S., 2004. Plotting Pseudorange Multipath with Respect to Satellite Azimuth and Elevation. GPS Solutions 8 (1), 44–48.

Houlié, N., Briole, P., Nercessian, A., Murakami, M., 2005a. Sounding the plume of the 18 August 2000 eruption of Miyakejima volcano (Japan) using GPS. Geophys. Res. Lett. 32, L05302.

Houlié, N., Briole, P., Nercessian, A., Murakami, M., 2005b. Volcanic Plume Above Mount St. Helens Detected with GPS. Eos Trans. AGU 86 (30), 277–281.

Kouba, J., 2009. Testing of global pressure / temperature (GPT) model and global mapping function (GMF) in GPS analyses. J. Geod. 83, 199–208.

Larson, K. M., Bilich, A., Axelrad, P., 2007. Improving the precision of high-rate GPS. J. Geophys. Res. 112, B05422.

Masterlark, T., 2007. Magma intrusion and deformation predictions: Sensitivities to the Mogi assumptions. J. Geophys. Res. 112, B06419.

Mastin, B. L. G., Roeloffs, E., Beeler, N. M., Quick, J. E., 2008. Constraints on the Size, Overpressure, and Volatile Content of the Mount St. Helens Magma System from Geodetic and Dome-Growth Measurements During the 2004- 2006 Eruption. U.S. Geological Survey Professional Paper 1750, pp. 461–488.

Miller, T. P., Chouet, B. A. (Eds.), 1994. The 1989-1990 Eruptions of Redoubt Volcano, Alaska. Journal of Volcanology and Geothermal Research, Special Issue.

Mogi, K., 1958. Relations between eruptions of various volcanoes and the deformations of the ground surface around them. Bull. Earthquake Res. Inst. Univ. Tokyo 36, 99–134.

Newman, A. V., Dixon, T. H., Gourmelen, N., 2006. A four-dimensional viscoelastic deformation model for Long Valley Caldera , California , between 1995 and 2000. Journal of Volcanology and Geothermal Research 150, 244 – 269.

Paul, F., 2010. GLIMS Glacier Database. Boulder, CO: National Snow and Ice Data Center/World Data Center for Glaciology. Digital Media.

Pinel, V., Sigmundsson, F., Sturkell, E., Geirsson, H., Einarsson, P., Gudmundsson, M. T., Högnadóttir, T., 2007. Discriminating volcano deformation due to magma movements and variable surface loads: Application to Katla subglacial volcano, Iceland. Geophys. J. Int. 169, 325–338.

Power, J., Stihler, S., Haney, M., 2012. Seismic observations of Redoubt Volcano, Alaska – 1989-2010 and forecasting of the 2009 eruption. Journal of Volcanology and Geothermal Research, Special Issue on the 2009 Redoubt Eruption, in press.

Press, W. H., Teukolsy, S. A., Vetterling, W. T., Flannery, B. P., 2007. Numerical Recipes: The Art of Scientific Computing, 3rd Edition. Cambridge University Press.

Reed, B. L., Lanphere, M. A., Miller, T. P., 1992. Double Glacier Volcano, a 'new' Quaternary volcano in the eastern Aleutian volcanic arc. Bull. Volc. 54, 631–637.

Schaefer, J. (Ed.), 2012. The 2009 Eruption of Redoubt Volcano, Alaska. Alaska Division of Geological & Geophysical Surveys Report of Investigation 2011-5, Fairbanks.

Schneider, D., Hoblitt, R., 2012. Doppler weather observations of the 2009 eruption of Redoubt Volcano, Alaska. Journal of Volcanology and Geothermal Research in review.

Segall, P., 2010. Earthquake and Volcano Deformation. Princeton University Press, Princeton.

Sigmundsson, F., 2006. Iceland Geodynamics, Crustal Deformation and Divergent Plate Tectonics. Springer-Praxis, Chichester, UK.

Suito, H., Freymueller, J. T., 2009. A viscoelastic and afterslip postseismic deformation model for the 1964 Alaska earthquake. Journal of Geophysical Research 114, B11404.

Turcotte, D. L., Schubert, G., 2002. Geodynamics. Cambridge University Press.

Voight, B., Widiwijayanti, C., Mattioli, G., Elsworth, D., Hidayat, D., Strutt, M., 2010. Magma-sponge hypothesis and stratovolcanoes: Case for a compressible reservoir and

quasi-steady deep influx at Soufrière Hills Volcano, Montserrat. Geophys. Res. Lett. 37, L00E05.

Waythomas, C., Pierson, T., Major, J., 2012. Lahar and flowage hazards in the Drift River valley associated with the 2009 eruption of Redoubt Volcano, Alaska. Journal of Volcanology and Geothermal Research, Special Issue on the 2009 Redoubt Eruption, in press.

Webley, P. W., Lopez, T. M., Dean, K. G., Rinkleff, P., Dehn, J., Cahill, C. F., Wessels, R. L., Schneider, D. J., Ekstrand, A., Bailey, J. E., Izbekov, P., Worden, A., 2012. Remote observations of eruptive clouds and surface thermal activity during the 2009 eruption of Redoubt volcano. Journal of Volcanology and Geothermal Research, Special Issue on the 2009 Redoubt Eruption, in press.

Werner, C., Kelly, P. J., Doukas, M., Lopez, T., Pfeffer, M., Mcgimsey, R. G., Neal, C. A., 2012. Degassing associated with the 2009 Eruption of Redoubt Volcano, Alaska. Journal of Volcanology and Geothermal Research, Special Issue on the 2009 Redoubt Eruption, in press.

Wessel, P., Smith, W. H. F., 1995. New version of the Generic Mapping Tools released. Eos Trans. AGU 76 (33), 329.

Yamakawa, N., 1955. On the Strain Produced in a Semi-infinite Elastic Solid by an Interior Source of Stress. Zisin (J. Seis. Soc. Japan), 84–98.

Yang, X. M., Davis, P. M., Dieterich, J. H., 1988. Deformation from Inflation of a Dipping Finite Prolate Spheriod in an Elastic Half-Space as a Model for Volcanic Stressing. Journal of Geophysical Research 93, 4257–4549.

Zumberge, J. F., Heflin, M. B., Jefferson, D. C., Watkins, M. M., Webb, F. H., 1997. Precise point positioning for the efficient and robust analysis of GPS data from large networks. J. Geophys. Res. 102 (B3), 5005–5017.

51
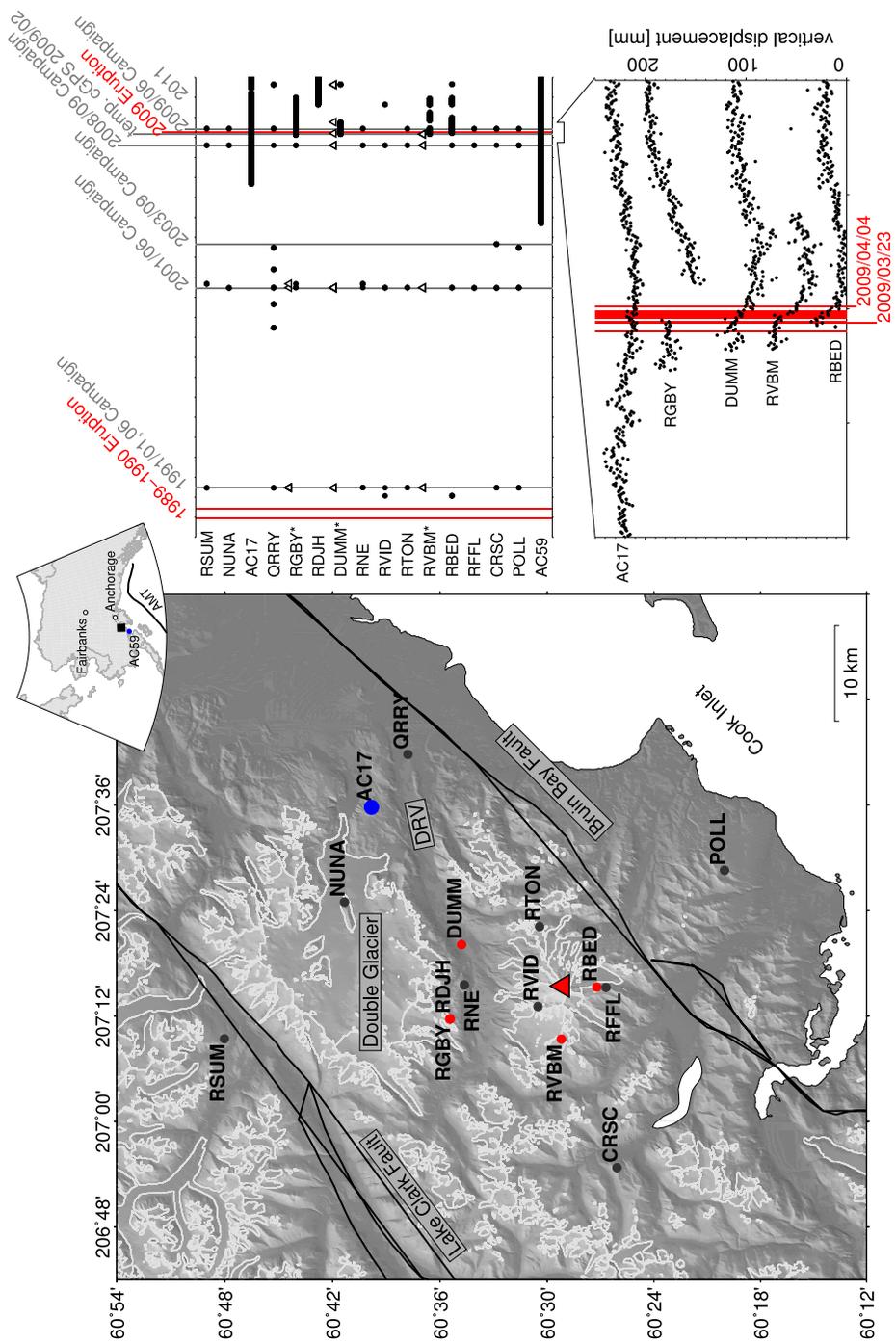
Figure 3.1: Regional setting and available GPS data for Redoubt Volcano. **Left:** Map of Redoubt area with GPS stations. The red triangle marks Mt. Redoubt. Red circles indicate temporary continuous GPS stations, black circles mark campaign GPS stations, the blue circle indicates the continuous PBO site AC17. White outlines mark glaciers in the region (Paul, 2010). The Double Glacier Ice cap to the north of Redoubt is outlined in gray and labeled; it seems to influence the time series at RGBY located on a cliff above one of its southern outlet glaciers. NUNA is located on a large nunatak that sticks out of the ice. The black lines from SW to NE indicate major faults in the region: Bruin Bay Fault to the south, and Lake Clark Fault north of Redoubt Volcano. DRV labels the mouth of the Drift River Valley. The black square in the inset indicates the location of this detail map. It also shows the location of the PBO site AC59 and the Aleutian Megathrust (AMT). **Right:** Overview of site occupations. Asterisks mark sites with composites of two tied markers. Each dot marks an existing daily positioning solution. Triangles mark occupations of DUMB, RGRB, and RVBR which are tied to DUMM, RGBY and RVBM, respectively. Times of individual campaigns are given on the top and marked by gray lines. Red lines mark the 1989-1990 eruption and the recent event of 2009. The timescale is linear. The lower right figure is a blow up of the (temporary) continuous stations from the decimal year 2008.75 to 2009.75 and shows vertical displacements for this time period. Vertical red lines indicate individual explosions (Table 1 in Bull and Buurman, 2012, this volume). Times are given for the first deformation inducing eruption on March 23, 2009, and the largest and last explosion on April 4th, 2009.

(A) original data in ITRF2008

(B) models removed
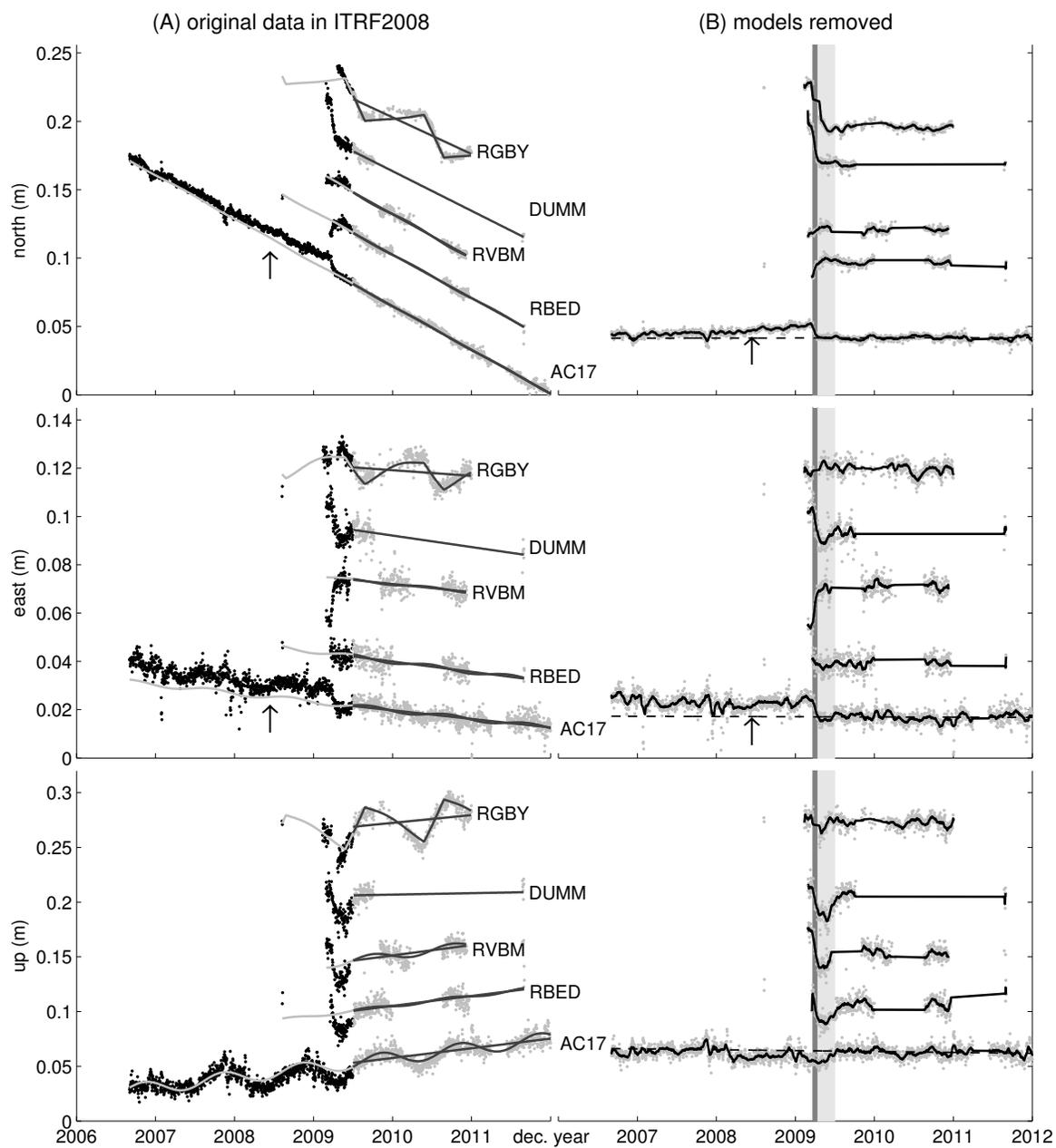
Figure 3.2: Original time series of positions in the ITRF 2008 (A) and detrended data (B) from 2006-2012. The rows show north, east and vertical displacements in meters (top to bottom). (**A**) Original GPS data for continuous GPS stations RGBY, DUMM, RVBM, RBED, and AC17 with outliers $> 3\sigma$ removed. Data from 2009.4 (May 26th, 2009) onwards (shown as gray dots) was used to estimate background linear trend and seasonal variations (shown in black for this period). These models were extrapolated into the past (shown in gray) to remove linear and seasonal trends while preserving the volcanic signal. DUMM has no seasonal model removed due to its short time series. Arrows in east and north panel indicate estimated onset of precursory deformation at AC17. (**B**) Detrended data, stations are ordered in the same way as in the left panel. Black line shows smoothed time series created using a moving average with window size of 20 data points. Smoothing starts when stations are continuous. The dark gray box in the background marks the explosive period from March 22 – April 05, 2009. The lighter gray box marks the effusive period from April 05–July 01, 2009 (Bull and Buurman, 2012, this volume). Dashed line for AC17 shows the post eruption average and illuminates pre-eruptive inflation and that the co-eruptive offset is overall larger than the pre-eruptive average in the horizontal field. Arrows in east and north panel indicate estimated onset of precursory deformation at AC17.
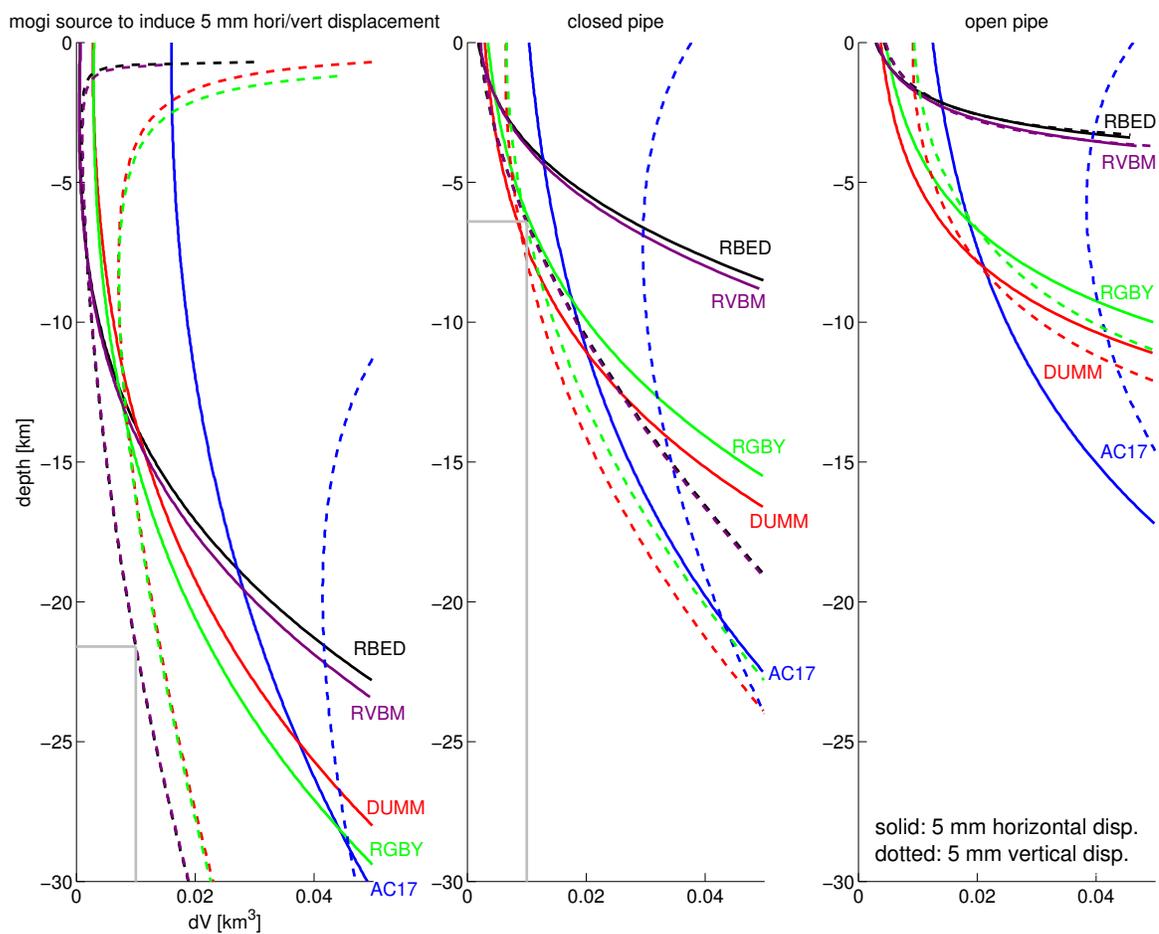
Figure 3.3: Network sensitivity for Redoubt GPS stations testing Mogi source, closed pipe, and open pipe with a source assumed centered underneath Redoubt's last dome from 2009 (Diefenbach et al., 2012). Colors refer to different stations; station names label respective lines. Solid and dotted lines represent horizontal and vertical 5 mm iso-displacement lines, respectively. A source that plots to the right of the line for a given station would produce > 5 mm displacement at that station. Gray boxes indicate how to find maximum depth for a given volume change (and vice versa) and which stations will show deformation.
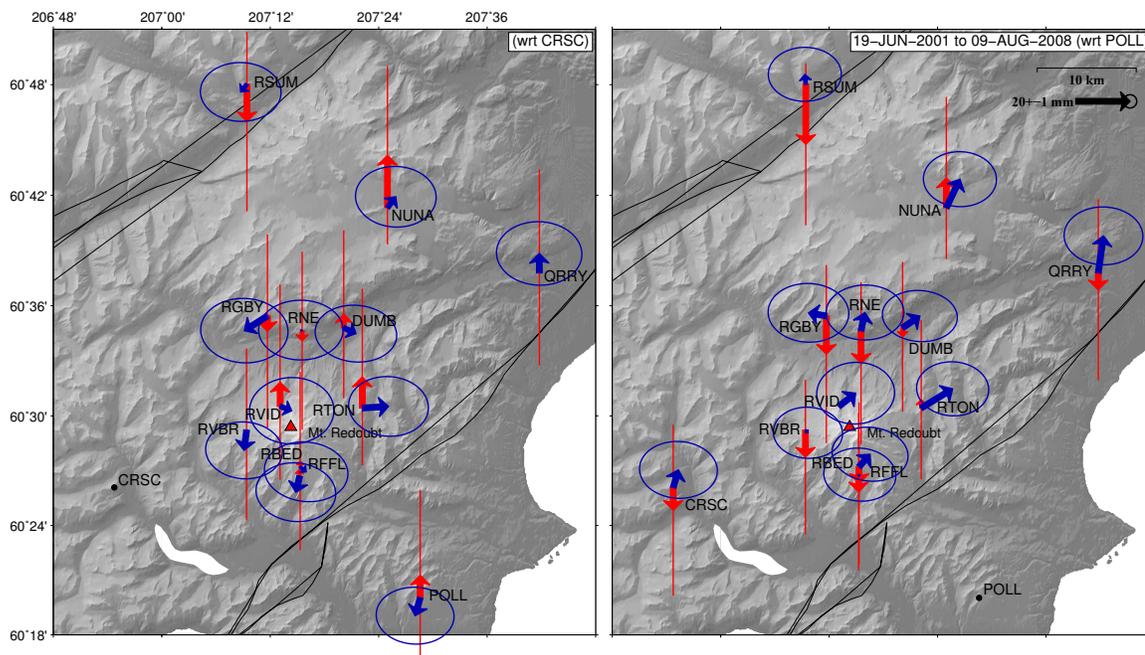
Figure 3.4: Displacements from 2001 to 2008 (inter-eruptive period) with respect to CRSC (left) and POLL (right). Blue vectors are horizontal displacements, red vectors are vertical displacements. Arrows are tipped with 95% confidence ellipses/lines. Numerical values for displacements (wrt POLL) are given in Table 3.2. Neither referencing the displacements to CRSC (left) nor to POLL (right) reveals a pattern consistent with deformation at Redoubt.
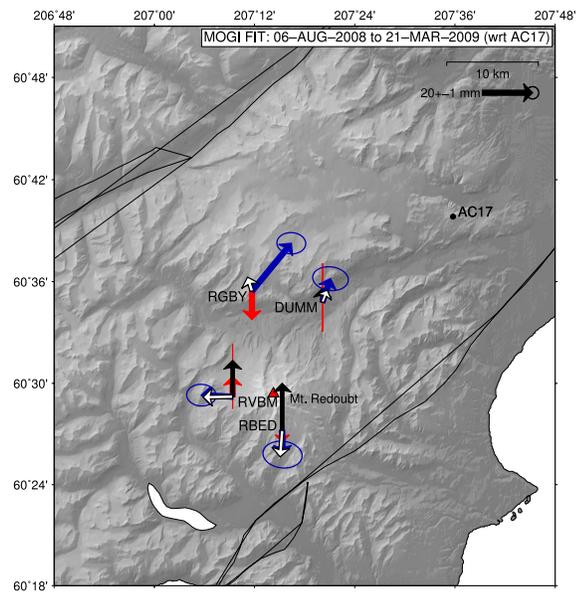
Figure 3.5: Displacements during pre-eruptive period from August 2008 to March 2009 with respect to AC17 (blue: horizontal, red: vertical) and displacements induced by a preliminary model (white: horizontal, black: vertical) inferred from horizontal displacements only. Data arrows are tipped with 95% confidence ellipses/lines. Preliminary model predictions assume a Mogi source at depth d = 21.75 km with volume change dV = 0.1018 km^3 (see column "preliminary precursory" in Table 3.3). The red triangle marks Mt. Redoubt.
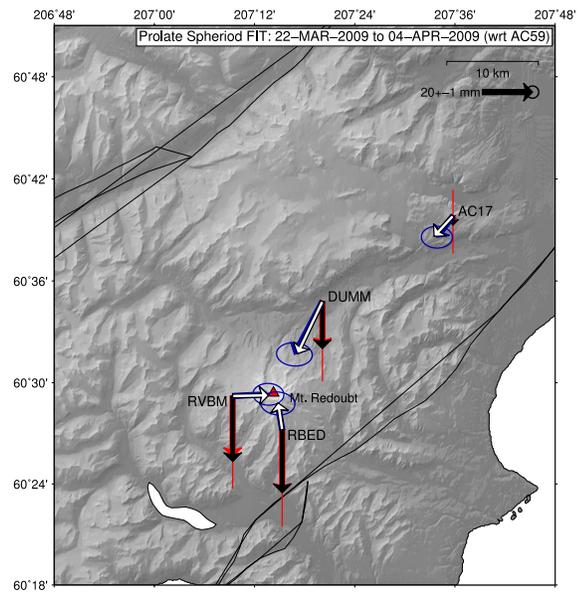
Figure 3.6: Displacements and model fit during explosive period from 22 March to 04 April with respect to AC59. Same symbols as in Figure 3.5. Both, vertical and horizontal data are fit well by the model. Vectors from all stations point straight at position of last dome (red triangle).
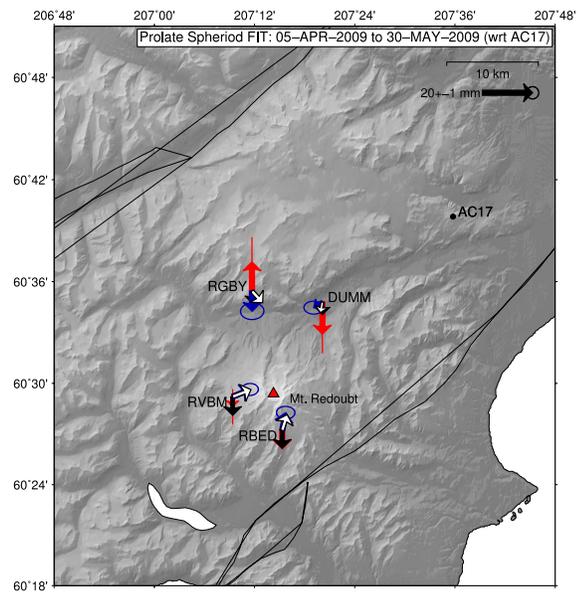
Figure 3.7: Displacements (blue: horizontal, red: vertical) and model fit (white: horizontal, black: vertical) for effusive period from 05 April to 30 May with respect to AC17. The model fit assumes the same prolate spheroid geometry as the explosive phase with volume change $dV = -0.0167\,km^3$ (see column "effusive" in Table 3.3) and is based on the fit to displacements at RBED and RVBM only. Data arrows are tipped with 95% confidence ellipses/lines. The red triangle marks Mt. Redoubt.

Mogi Source Fit

Prolate Spheroid Fit
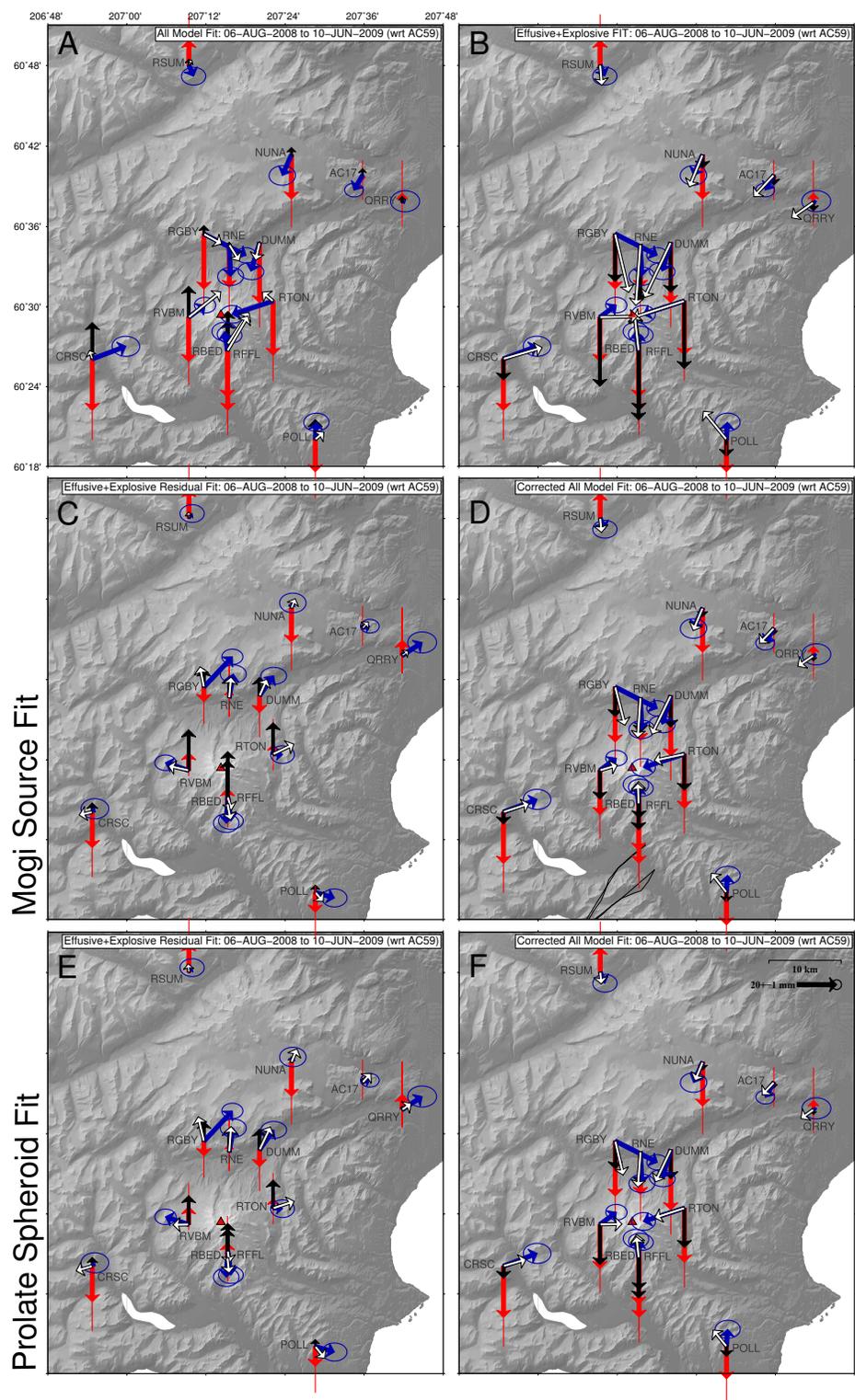
Figure 3.8: Displacements relative to AC59 from August 2008 to June 2009 spanning the full eruption. Clearly, we see a net deflation, i.e., net loss of material. Each panel shows different forward models (black and white vectors). **(A)** Sum of displacements for the best fitting sources from preliminary precursory, explosive and effusive period provides poor fit to the data. **(B)** Sum of displacements due to explosive and effusive source only (prolate spheroid). The residuals, inferred to represent the precursory deformation are plotted as colored vectors in **(C)** and **(E)**. **(C)** Fit of best Mogi model (black and white vectors, see Table 3.3) to residuals (colored vectors). **(D)** Sum of displacements for all source models using the source model derived from **(C)** as precursory source model. **(E)** Best fitting volume change of explosive source model (black and white vectors, see Table 3.3) to residuals (colored vectors). **(F)** Sum of displacements for all source models using the source model derived from **(E)** as precursory source model.
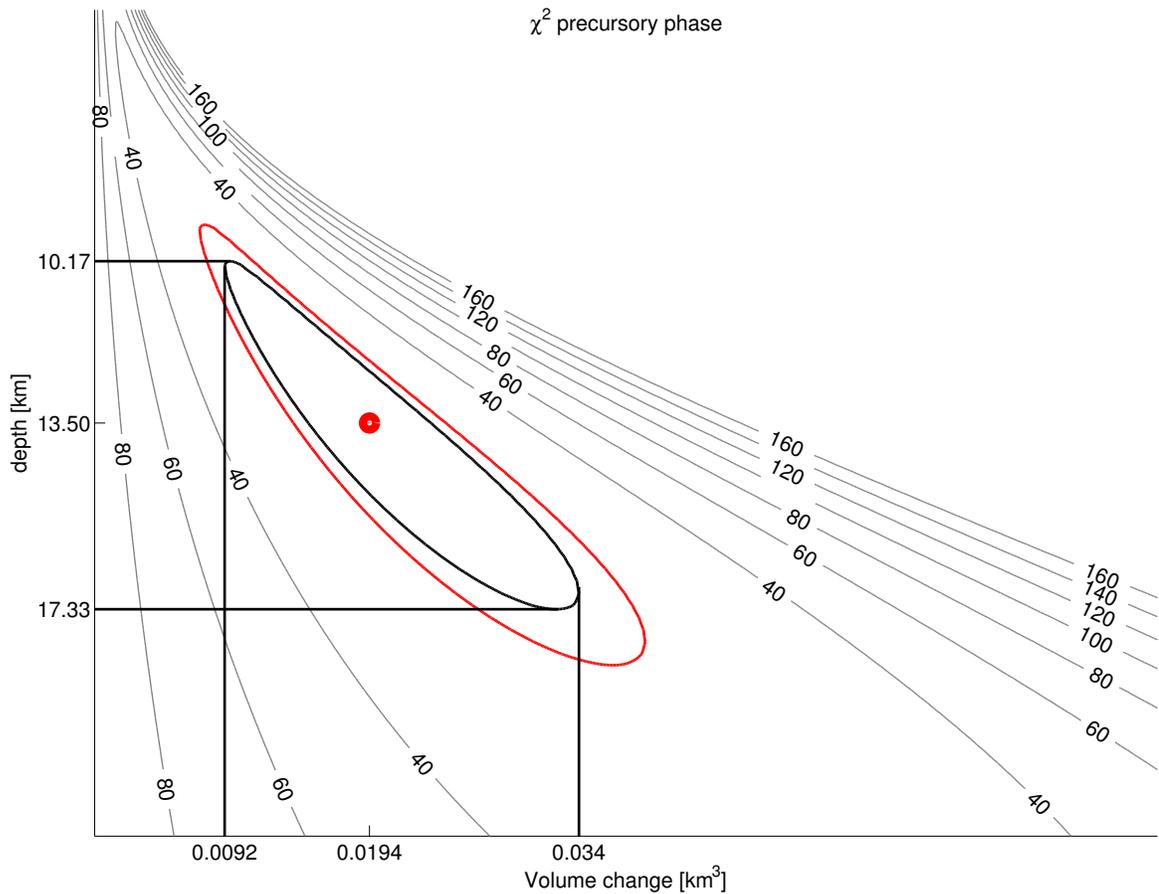
Figure 3.9: χ^2 contour plot showing change of misfit depending on variation of the two parameters depth and volume change for the precursory phase derived from displacements for the full event. Red dot is best fitting model from the inversion. Ellipses show confidence intervals at 95% level derived from $\Delta\chi^2$; red ellipse for two free parameters; black ellipse assumes one free parameter at the 95% confidence level and is used to project confidence intervals on the axes (black lines; see Press et al. (2007)).
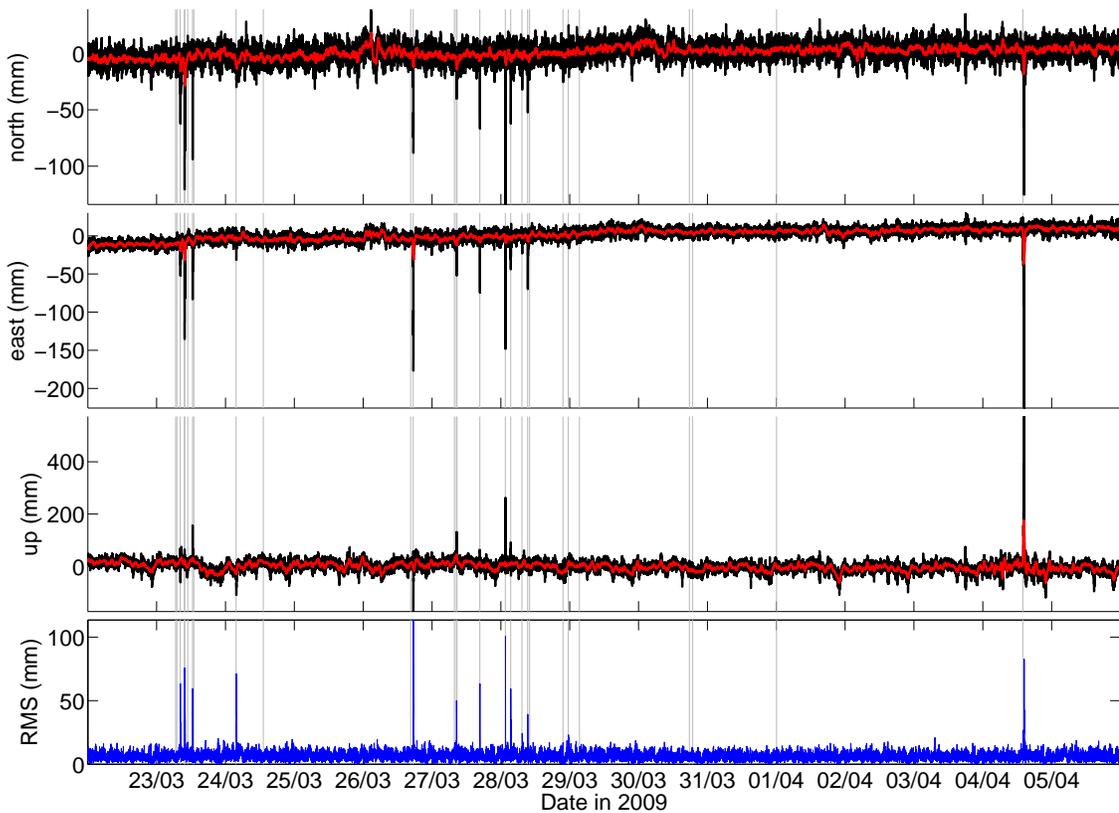
Figure 3.10: RVBM kinematic position time series with respect to AC17 from March 20 to April 5, 2009 (north, east, up, and RMS). Black lines are 30 s solutions, red lines are half-hour sliding window averages. Vertical gray lines indicate individual explosions (Table 1 in Bull and Buurman, 2012, this volume). Large plumes result in phase delay and hence position changes of RVBM (Houlié et al., 2005a,b) due to phase delays for satellite-station combinations that cross the plume.
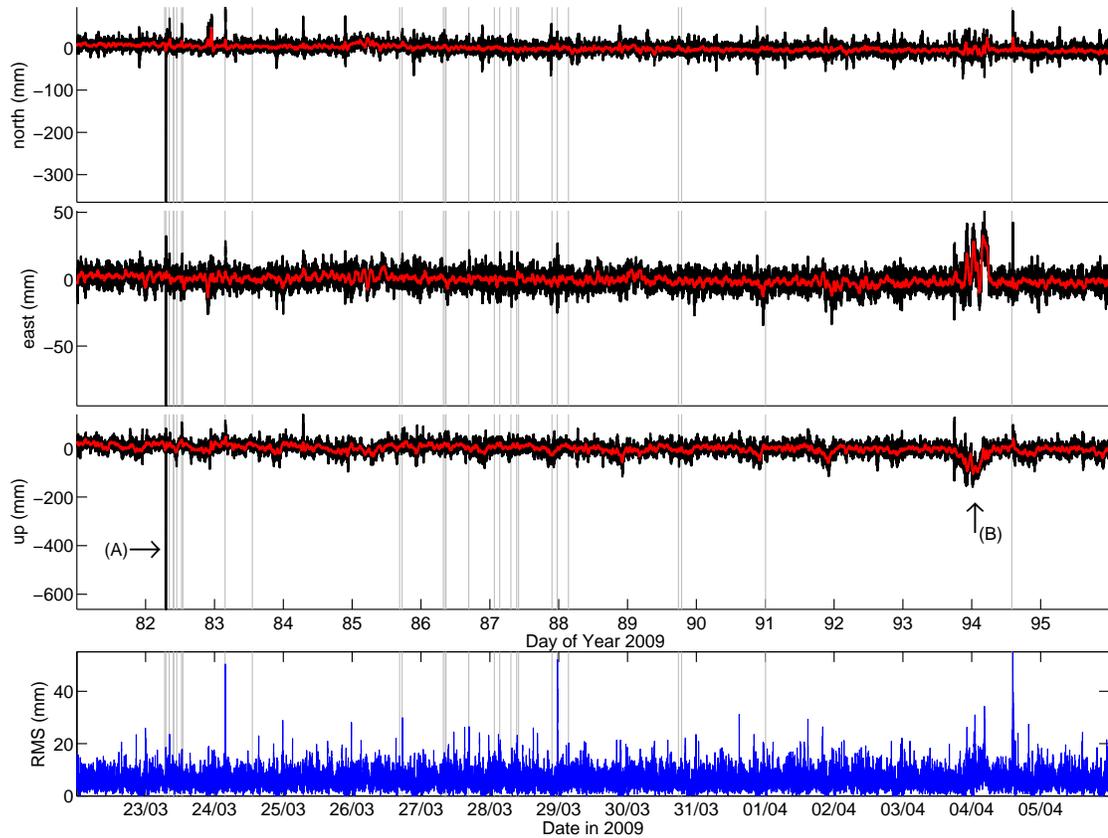
Figure 3.11: Same as Figure 3.10 but for station DUMM. Arrow (A) marks non-plume related spike on March 23, 2009. Arrow (B) marks unexplained deformation at the end of April 03 to April 04, 2009.
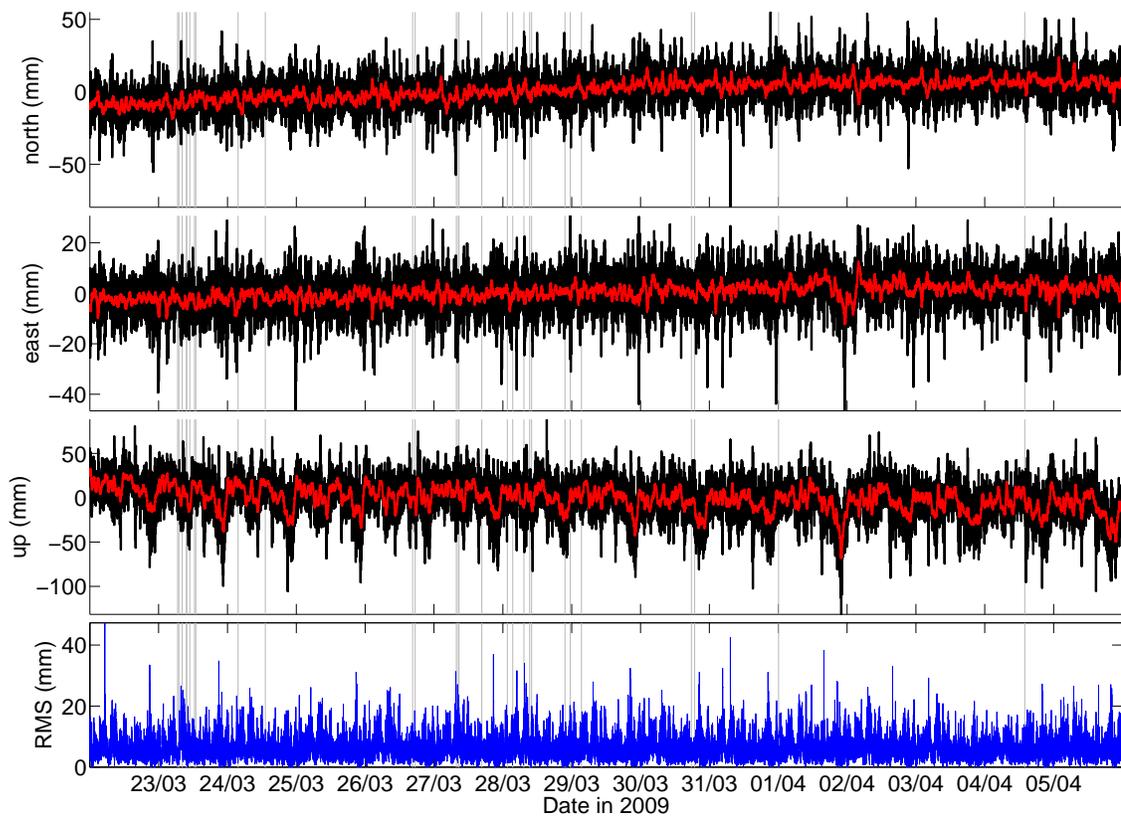
Figure 3.12: Same as Figure 3.10 but for station RBED.
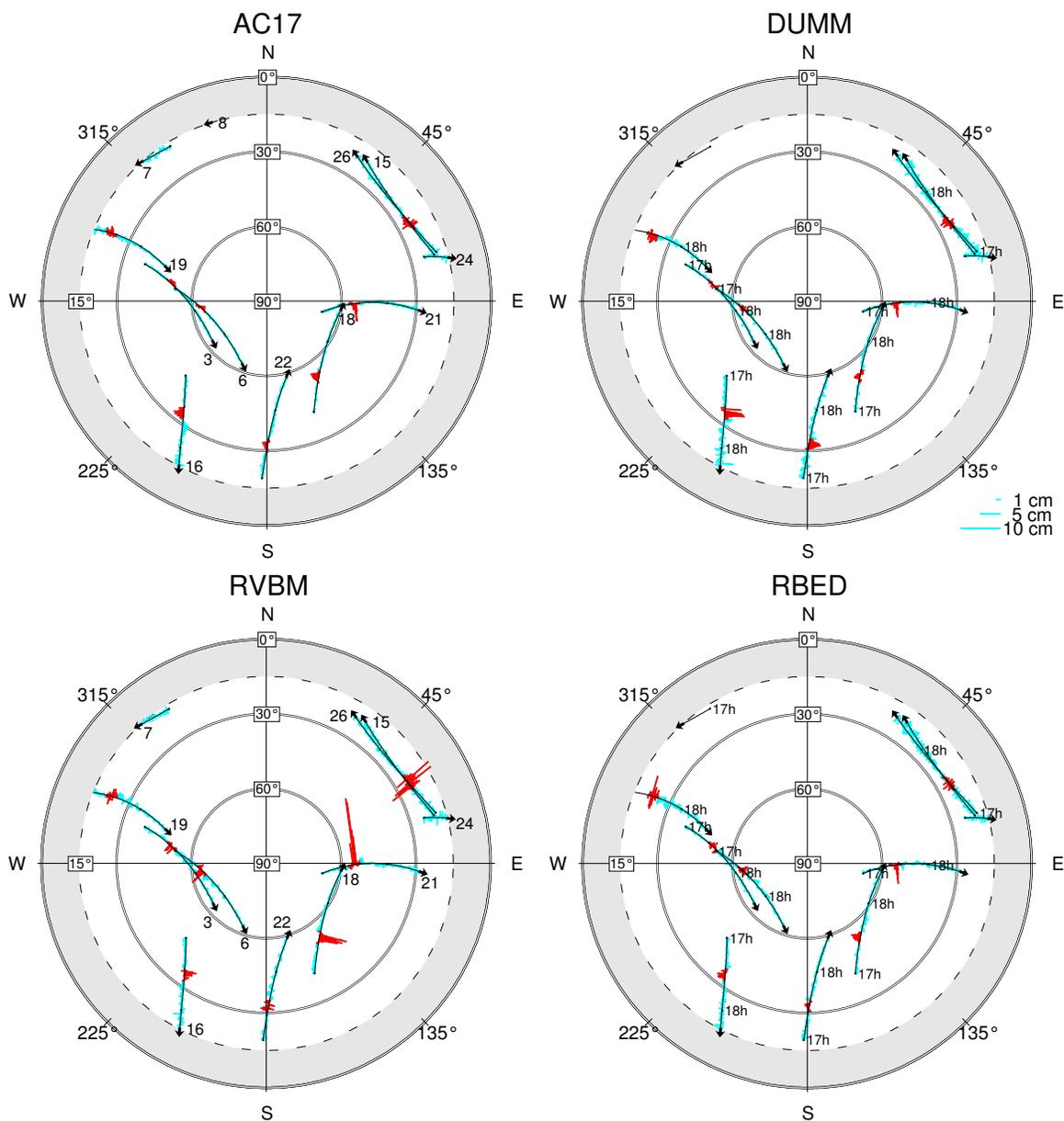
Figure 3.13: Skyplot of phase residuals per satellite for AC17, DUMM, RVBM, RBED for March 26, 2009 from 17:00 to 18:30 UTC covering the time Event 18 occurred (17:24 UTC, Bull and Buurman (2012, this volume)). The setup is similar for each of the subplots: the outer circle marks azimuths for the satellites and also indicates $0°$ degrees of elevation above the horizon as seen from the station. The two inner circles mark $30°$, $60°$ of elevation. $90°$ of elevation is directly above the station. Thin black lines indicate the tracks of the GPS satellites. The turquoise lines are the time series of phase residuals for this satellite. The red sections indicate the eruption time from 17:24–17:35 UTC. See text for detailed description on observations. Satellites are identified in the left column by PRN numbers at the end of the sky tracks next to a black arrow that points in the direction of motion of the satellite. The numbers next to black dots in the right column along those lines mark full UTC hours of the observation interval.

64
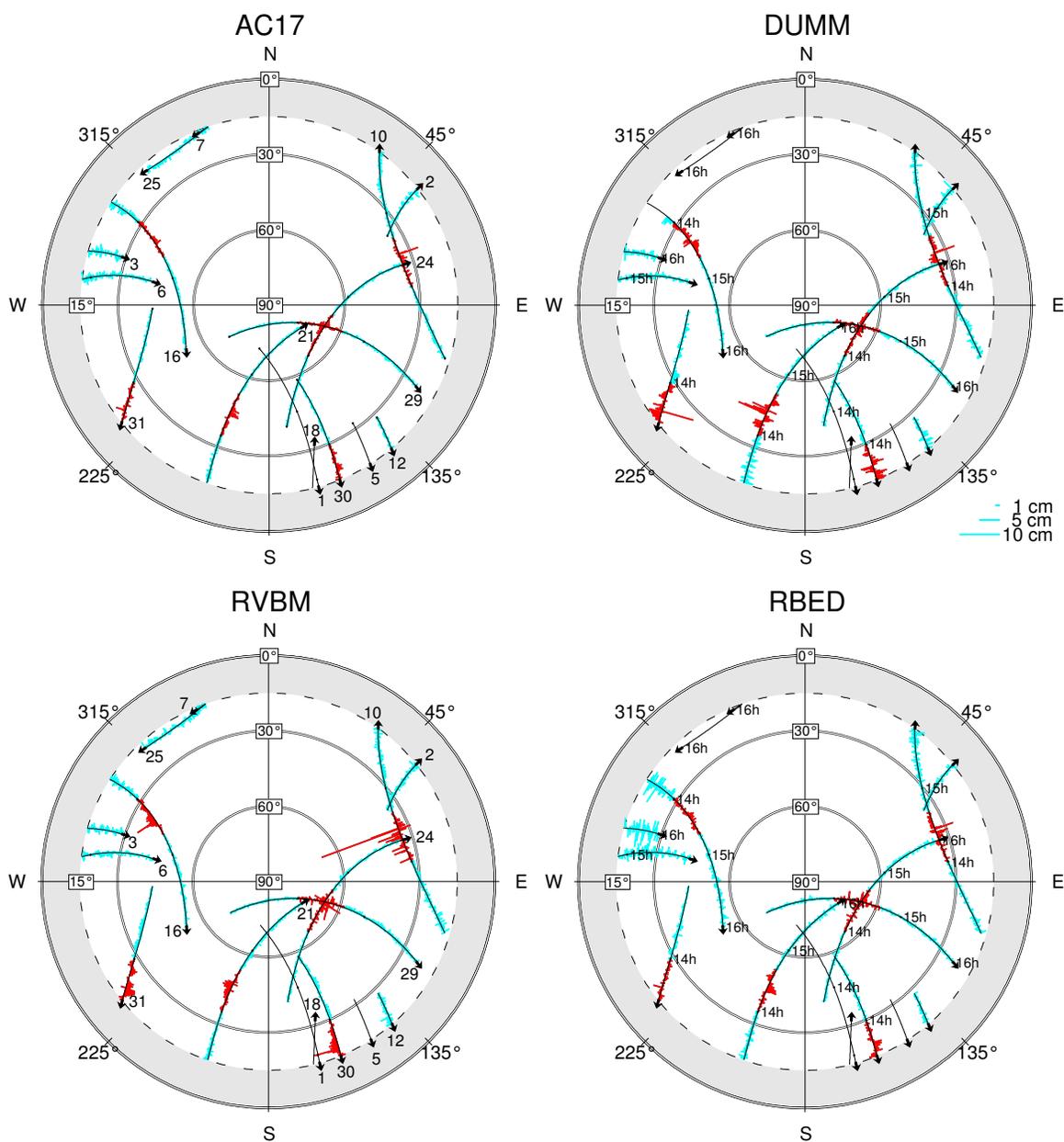
Figure 3.14: Skyplot of phase residuals per satellite for AC17, DUMM, RVBM, RBED for April 04, 2009. Red sections indicate time of eruption from about 14:00–14:40 UTC. Figure 3.13 describes the setup of this figure.
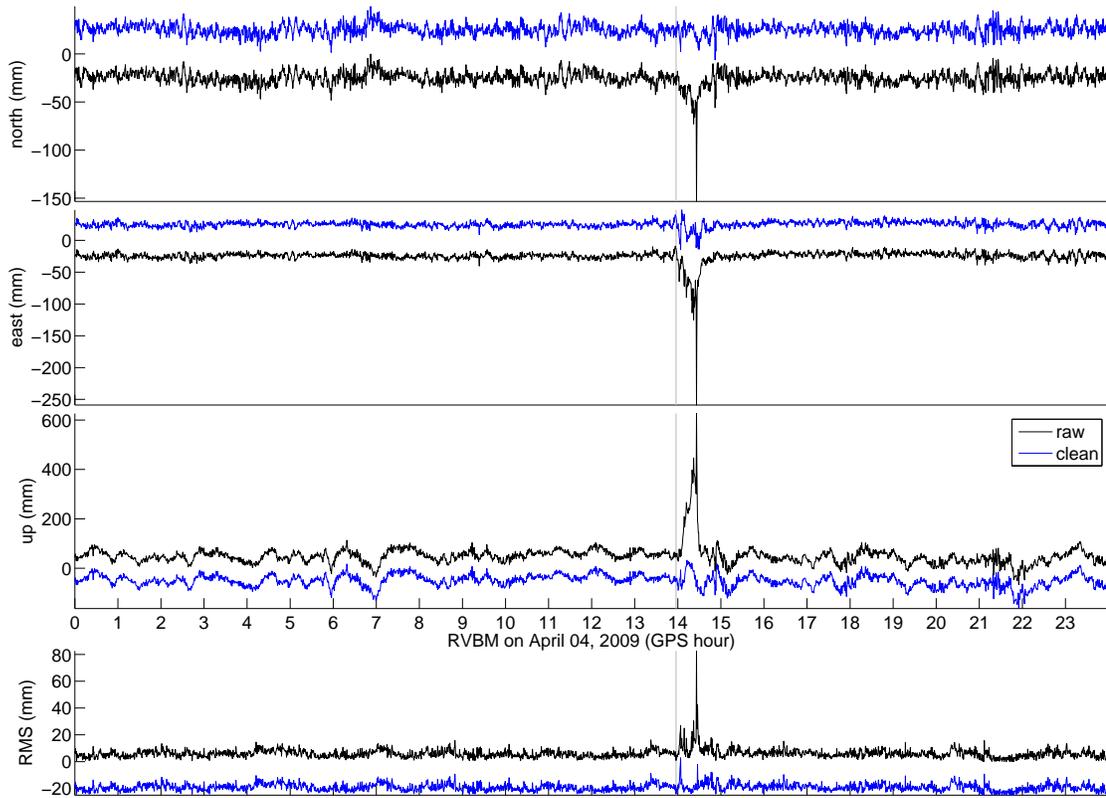
Figure 3.15: Kinematic solution for RVBM on April 04, 2009 with AC17 as a base station. Black line is original solution, blue line shows position time series with satellite PRN 10 deleted from 14:00-14:45 GPS time (shifted for clarity). Clearly the spike in the position time series is reduced, as is the associated RMS value. Some scatter in the position remains which may be due to the other satellites being affected by ash or actual ground motion associated with the eruption.
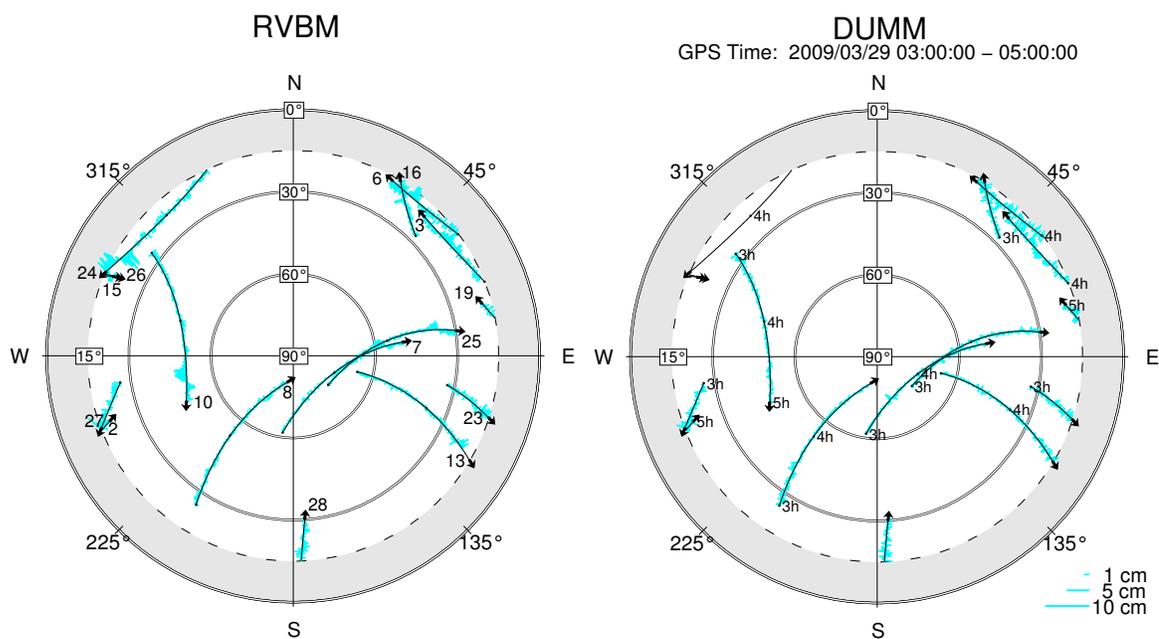
Figure 3.16: Skyplot of phase residuals per satellite for DUMM and RVBM for March 29, 2009, Figure 3.13 describes the setup of this figure. Event 18 (Bull and Buurman, 2012, this volume) occurs at 3:23 UTC with a plume extending to the NE
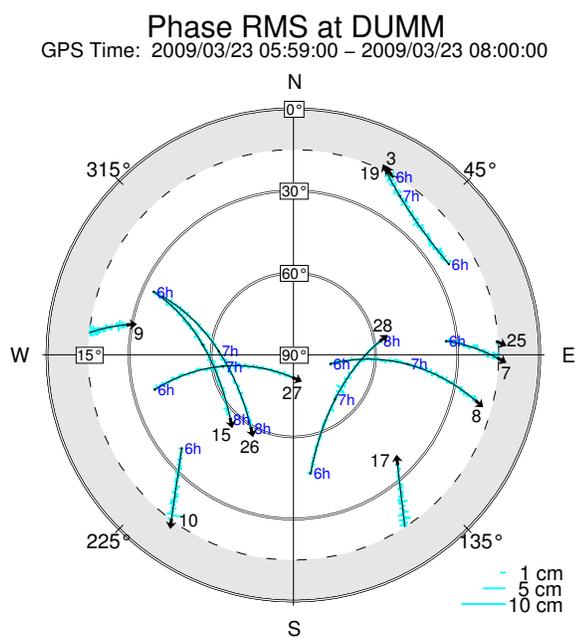
Figure 3.17: Skyplot of phase residuals per satellite for DUMM for March 23, 2009, Figure 3.13 describes the setup of this figure. The big spike in Figure 3.11 coincides with event 01 at about 06:38 UTC, but is not associated with any unusual residuals.
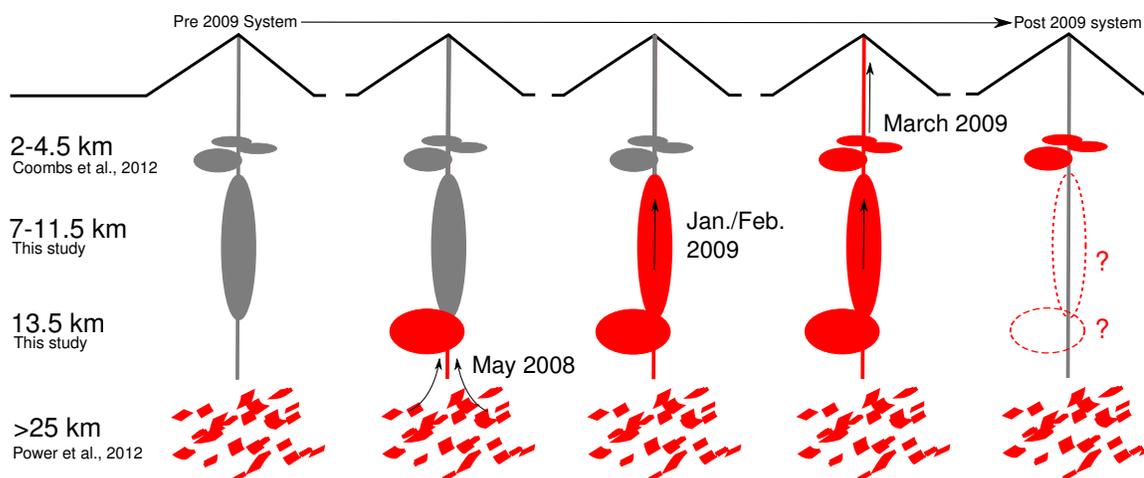
Figure 3.18: Cartoon illustrating the suggested evolution of the Mt. Redoubt plumbing system as suggested by geodetic, seismic, and petrologic data. Here we tie deep seismicity (Power et al., 2012, this volume), petrology (Coombs et al., 2012, this volume), and our observations together by proposing a two reservoir system in the mid- to shallow crust. Material from 25–38 km migrated to about 13 km depth beginning as early as May 2008; reheating and remobilizing residing material in the prolate spheroid from 7-11.5 km. This resulted in migration to 2-4.5 km depth (Coombs et al., 2012); supported by shallow seismic tremor beginning in January / February 2009 (Buurman et al., 2012). This material extruded form 23 March 2009 on. The mix of fresh and reheated material from the deeper stages of the system replaced extruded material and made the shallow removal undetectable by geodesy.

Table 3.1: Redoubt Volcano GPS benchmark coordinates. Installation dates (YYYY-MM-DD) represent the earliest available data.

4 Char ID	Lat (deg.)	Lon (deg.)	Height (m)	Installation Date	Dist to Redoubt (km)
RSUM	60.800404	-152.843023	908.4798	1991-06-20	35
NUNA	60.688944	-152.583804	954.2120	1991-06-20	24
QRRY	60.629873	-152.303741	56.1551	1991-06-20	30
RGBY	60.590781	-152.805216	1421.4969	2001-06-25	12
RDJH	60.590764	-152.805241	1422.4000	2010-08-20	12
DUMB	60.579978	-152.664516	230.6017	1991-06-20	11.5
DUMM	60.579923	-152.664469	231.1957	2009-02-27	11.5
RNE_	60.577380	-152.741092	994.2093	1991-06-25	10
RVID	60.508641	-152.781835	1886.6534	1991-01-25	2.4
RTON	60.507123	-152.630164	1358.8424	1991-06-23	7.5
RVBM	60.486809	-152.843623	1646.2630	2009-02-28	4.5
RVBR	60.486866	-152.843663	1646.2310	1991-06-23	4.5
RBED	60.453568	-152.744912	1557.8103	1991-01-25	4.0
RFFL	60.444978	-152.745881	1445.8446	1991-06-23	5.0
CRSC	60.434693	-153.087553	1073.3678	1991-06-22	19
POLL	60.333857	-152.523572	849.9948	1991-06-21	22
		West of Cook Inlet			
AC17	60.663902	-152.403846	882.6025	2006-08-31	28
AC59	59.567197	-153.585201	308.5802	2004-09-01	112

Table 3.2: Overview of displacements for the eruptive phases: Shows displacement values and uncertainties for each station in ENU direction for each of the periods described in the text.

phase:	inter-eruptive			pre-eruptive			explosive		
time:	06/2001–08/2008 (wrt POLL)			08/2008–03/2009 (wrt AC17)			03/2009–04/2009 (wrt AC59)		
# solutions:	17			46			14		
site	E	N	U (cm)	E	N	U	E	N	U
AC17	–	–	–	0.00 ± 0.0	0.00 ± 0.0	0.00 ± 0.0	-0.64 ± 0.3	-0.85 ± 0.2	-0.23 ± 0.5
CRSC	0.19 ± 0.6	0.65 ± 0.4	-0.84 ± 1.3	–	–	–	–	–	–
DUMM	–	–	–	0.32 ± 0.3	0.94 ± 0.2	0.18 ± 0.6	-1.12 ± 0.3	-2.12 ± 0.2	-1.83 ± 0.6
NUNA	0.50 ± 0.6	1.05 ± 0.4	1.09 ± 1.2	–	–	–	–	–	–
POLL	0.00 ± 0.0	0.00 ± 0.0	0.00 ± 0.0	–	–	–	–	–	–
QRRY	0.19 ± 0.6	1.37 ± 0.4	-0.63 ± 1.4	–	–	–	–	–	–
RBED	0.41 ± 0.6	0.46 ± 0.4	-0.61 ± 1.2	0.02 ± 0.3	-0.97 ± 0.2	-0.46 ± 0.6	-0.18 ± 0.3	1.05 ± 0.2	-2.51 ± 0.5
RFFL	0.04 ± 0.5	0.06 ± 0.4	-0.58 ± 1.2	–	–	–	–	–	–
RGBY	-0.66 ± 0.6	0.11 ± 0.4	-1.41 ± 1.3	1.57 ± 0.2	1.91 ± 0.2	-1.14 ± 0.5	–	–	–
RNE	0.14 ± 0.6	0.67 ± 0.4	-1.20 ± 1.2	–	–	–	–	–	–
RTON	1.16 ± 0.5	0.71 ± 0.4	0.31 ± 1.2	–	–	–	–	–	–
RSUM	-0.04 ± 0.6	0.36 ± 0.4	-2.22 ± 1.2	–	–	–	–	–	–
RVBM	–	–	–	-1.25 ± 0.2	0.06 ± 0.2	0.81 ± 0.5	1.43 ± 0.3	0.07 ± 0.2	-2.43 ± 0.5
RVID	0.61 ± 0.6	0.49 ± 0.5	0.05 ± 1.4	–	–	–	–	–	–

Table 3.2: continued.

phase:	effusive			full eruption			post eruptive		
time:	04/2009–06/2009 (wrt AC59)			08/2008–06/2009 (wrt AC59)			06/2009–09/2011 (wrt AC17)		
# solutions:	56			10			851		
AC17	-0.30 ± 0.1	-0.04 ± 0.1	-0.04 ± 0.3	-0.43 ± 0.2	-0.75 ± 0.1	-0.24 ± 0.4	0.00 ± 0.0	0.00 ± 0.0	0.00 ± 0.0
CRSC	–	–	–	1.70 ± 0.3	0.64 ± 0.2	-2.60 ± 0.6	–	–	–
DUMM	-0.66 ± 0.2	-0.30 ± 0.1	-1.31 ± 0.3	-0.43 ± 0.3	-1.44 ± 0.2	-3.04 ± 0.5	-0.16 ± 0.2	0.64 ± 0.1	-0.49 ± 0.4
NUNA	–	–	–	-0.46 ± 0.3	-1.03 ± 0.2	-2.23 ± 0.6	–	–	–
POLL	–	–	–	0.06 ± 0.3	0.87 ± 0.2	-1.64 ± 0.6	–	–	–
QRRY	–	–	–	0.15 ± 0.3	0.07 ± 0.2	0.46 ± 0.7	0.27 ± 0.4	-0.26 ± 0.3	-2.10 ± 0.9
RBED	-0.18 ± 0.2	0.65 ± 0.1	-0.80 ± 0.3	0.09 ± 0.3	0.47 ± 0.2	-3.35 ± 0.5	0.05 ± 0.1	-0.28 ± 0.1	1.08 ± 0.2
RFFL	–	–	–	-0.14 ± 0.3	0.97 ± 0.2	-2.35 ± 0.6	–	–	–
RGBY	-0.26 ± 0.2	-0.82 ± 0.1	1.14 ± 0.4	2.14 ± 0.2	-1.08 ± 0.2	-2.78 ± 0.5	0.24 ± 0.1	0.91 ± 0.1	0.10 ± 0.2
RNE	–	–	–	0.07 ± 0.3	-1.60 ± 0.2	-2.16 ± 0.5	–	–	–
RTON	–	–	–	-2.07 ± 0.2	-0.67 ± 0.2	-2.74 ± 0.5	–	–	–
RSUM	–	–	–	0.24 ± 0.3	-0.56 ± 0.2	1.26 ± 0.5	–	–	–
RVBM	0.38 ± 0.1	0.25 ± 0.1	-0.46 ± 0.3	0.83 ± 0.2	0.62 ± 0.2	-2.24 ± 0.5	0.11 ± 0.1	-0.07 ± 0.1	0.49 ± 0.3
RVID	–	–	–	–	–	–	–	–	–

Table 3.3: Best fitting models. Depth values in parenthesis are actual model results not topography corrected as for the spheroids the average elevation had to be removed to move the reference surface to sea level and give depths below sea level. Confidence intervals (superscripts and subscripts) are given at the 95% level.

	preliminary precursory		final precursory		explosive		effusive	
stations	DUMM, RBED, RVBM		AC17, CRSC, NUNA, RBED, RFFL RNE, RSUM, RTON, RVBM		AC17, DUMM, RBED, RVBM		RBED, RVBM	
# observables	6 (horizontal only)		18 (horizontal only)		12 (horizontal + vertical)		6 (horizontal + vertical)	
average elevation (m)	1145.01		1202.67		1079.40		1601.70	
source geometry	closed conduit	Mogi	**Mogi**	**Prolate Spheroid**	**Prolate Spheroid**	Mogi	**Prolate Spheroid**	Mogi
centroid depth (km)	10.61 (11.75)	21.75	**13.50** $^{10.17}_{17.33}$	see explosive	**9.17** $^{6.92}_{15.17}$ (10.25)	15.25	see explosive	8.75
semimajor (km)	12.00	–	–	see explosive	**4.50** $^{1.25}_{>10.00}$	–	see explosive	–
semiminor (km)	0.025	–	–	see explosive	**0.475** $^{0.3}_{>4.00}$	–	see explosive	–
ΔV (km^3)	0.0309	0.1018	**0.0194** $^{0.0092}_{0.0340}$	**0.0278** $^{0.0214}_{0.0341}$	$-($**0.05** $^{0.028}_{>0.1})$	-0.0303	$-($**0.0167** $^{0.0106}_{0.0228})$	-0.0034
dx (km)	-1.75	-3.25	**0.00**	see explosive	**0.50**	1.00	see explosive	1.75
dy (km)	-2.75	-4.00	**-1.25**	see explosive	**0.00**	0.25	see explosive	1.75
χ^2	0.1005	1.1426	14.2667	18.54055	0.2450	11.0137	0.7468	0.1470

Chapter 4

Surface Deformation of Bezymianny Volcano, Kamchatka, Recorded by GPS: The Eruptions from 2005-2010 and Long-term, Long-wavelength Subsidence[1]

Abstract

Since Bezymianny Volcano resumed its activity in 1956, after $\sim$1000 years of dormancy, eruptions have been frequent with up to 1-2 explosive events per year in recent years. We installed a GPS network of 8 continuous and 6 campaign stations around Bezymianny in 2005 and 2006 to investigate deformation related to this activity. The two striking observations for 2005-2010 are (1) rapid and continuous network-wide subsidence at rates between 8 and 12 mm/yr, which appears to affect KAMNET stations more than 40 km away where we observe 4-5 mm/yr of subsidence, and (2) only the summit station BZ09 shows slight deviations from the average motion in the north component at times of eruptions.

We test various hypotheses to explain the network-wide subsidence. Tectonic deformation related to the build-up of interseismic strain from subduction of the Pacific plate induces negligible vertical motions. A first order model of surface loading by eruptive products of the Kluchevskoy Group of Volcanoes (KGV) explains a fraction of the signal. A deep sill at about 30 km which constantly discharges material that may be fed into shallower reservoirs under Bezymianny and Kluchevskoy fits our observations well. The very localized sampling of GPS velocities supports a wide range of geometries for this model. Deep seismicity underneath Kluchevskoy poses additional constraints on location and geometry and suggests a sill of 9.5 km width, 12.7 km length, and a 13° dip-angle to the south-east. We infer a closing rate of 0.22 m/yr, which results in a volume loss of 0.027 km^3/yr (0.16 m/yr and 0.019 km^3/yr respectively, considering surface loading). Additional stations in the near and far field are required to uniquely resolve the spatial extent and likely partitioning of this source.

The explosion related deformation at BZ09 can be explained by a very shallow reservoir, likely within Bezymianny's edifice, suggested by Thelen et al. (2010). This reservoir could be at about 0.25–1.5 km depth with a volume change of 1-4$\times$10^{-4} km^3. Much of the

---

material erupted at Bezymianny may be sourced from deeper mid-crustal reservoirs with co-eruptive volume changes at or below the detection limit of the GPS network. Installation of more sensitive instruments such as tiltmeters would lower the detection limit of the network and hence allow resolving more subtle co-eruptive motion.

4.1 Introduction

Bezymianny Volcano is part of the KGV at the northern end of the Central Kamchatka Depression in Kamchatka, Russia (Figure 4.1). The group is named after Kluchevskoy Volcano, the tallest (4835 m) and most productive volcano in Eurasia (60 Gt/yr, which translates to about 0.023 km^3/yr of basalt, Fedotov et al., 2010) about 10 km to the north-northeast of Bezymianny volcano. Tolbachik (Figure 4.1), about 20 km to the south-west of Bezymianny, is another notable volcano of this group, because in 1975-76 it produced the largest basaltic eruption in Kamchatka in historical time (Fedotov and Markhinin, 1983; Fedotov et al., 2010).

Bezymianny itself is equally notable; after about 1000 years of dormancy this 11,000 year old volcano (Belousov et al., 2007) entered a new period of activity that started with a catastrophic flank collapse and lateral blast eruption in 1956 (Gorshkov, 1959; Belousov et al., 2007). The resulting horseshoe shaped crater opens to the south-east (Figure 4.1) and was quickly filled by a new dome (Malyshev, 2000). The dome now almost touches the crater walls which it already exceeds in elevation. Having changed its mode of growth from internal to external over the decades, the dome has formed a crater of its own (Carter et al., 2007) and lava flows run down its flanks.

Current activity of Bezymianny is characterized by roughly 1-2 explosive eruptions per year (e.g., Girina, 2012, this volume), which are accompanied by pyroclastic flows and small lava flows. Prior work on the system that feeds such activity, as well as the large production rates of the entire group, suggests a deep reservoir at about 30 km depth below Kluchevskoy volcano (Fedotov et al., 2010; Koulakov et al., 2011, 2012). From there magma is suggested to migrate into more shallow, mid-crustal reservoirs beneath Kluchevskoy (Fedotov et al., 2010) and Bezymianny (Fedotov et al., 2010; Thelen et al., 2010). An additional very shallow magma or volatile region within the edifice of Bezymianny was suggested by Thelen et al. (2010). However, their study was limited to only 3 months

of data in the latter half of 2007, so it remains unclear whether this is a transient or permanent feature. Studies of relatively insoluble/soluble gas species ratios observed in fumarole samples collected in 2007, 2009, and 2010 (Lopez et al., 2012, this volume) certainly strengthen the case of Thelen et al. (2010) for the existence of a very shallow reservoir. Lopez et al. (2012, this volume) find evidence for degassing of magma at shallow depths in August 2007 and July 2010; potentially within the edifice (pers. comm. with T. López, 2012). For July 2009 Lopez et al. (2012, this volume) find evidence for degassing of a deeper magma source, with the actual depth hard to constrain using current methods.

While long term seismicity from 1999-2010 draws a fairly clear picture supporting the subsurface structure described above (Thelen et al., 2010, their Figure 1), which is furthermore supported through petrologic studies (Turner et al., 2012, this volume), recent 4-D seismic tomography (Koulakov et al., 2012) suggests the mid-crustal to shallow structures are more transient in nature and only the deep reservoir under Kluchevskoy appears permanent. This may be similar to interpretations of deformation at Kluchevskoy from 1981-88 by Fedotov et al. (1992) who interpret their observations with a migrating pressure source.

Until now this complex region has not been a target of dense GPS deformation studies. The last published geodetic study by Fedotov et al. (1992) gives an overview of leveling and triangulation surveys that were conducted from 1978-1989. Along one leveling line that runs east-west at about 3-4 km south of Bezymianny Fedotov et al. (1992) report 45 mm of subsidence from 1978-1987 over a broad region (∼50-60 km). The source of this signal remains uninterpreted. Analysis of satellite data from 1992-2003 by Pritchard and Simons (2004b) reveals high rates of subsidence in the vicinity of the 1975-76 Tolbachik lava flows. No deformation due to any of the eruptions at the KGV volcanoes during that period could be resolved due to poor spatial and temporal coverage, which limits detection to larger signals in that region (Pritchard and Simons, 2004b).

Here, we present the first detailed geodetic study of Bezymianny Volcano based on continuous and campaign GPS measurements spanning the years 2005–2010. This work is part of the Partnerships in International Research and Education program (PIRE-Kamchatka), sponsored by the National Science Foundation and carried out in collaboration with the Institute of Volcanology and Seismology (IVS) and the Kamchatkan Branch of Geophysi-

cal Services (KBGS). This project targeted Bezymianny Volcano from a range of different perspectives (including Seismology, Petrology, Geodesy, Gas, Geology, Remote Sensing) to investigate the effect of sector collapse on the evolution of a volcanic system. Our main goals were (1) investigate GPS time series for deformation related to individual explosive events and infer constraints for the subsurface magmatic system, and (2) explain the constant, network-wide subsidence observed during the investigation period. To find answers to (2), we test various hypotheses including effects of subduction related strain accumulation, effects of surface load changes due to lava deposition and edifice growth, deflation of a deep magma reservoir replenishing the shallower reservoirs that drive the regular eruptions at Kluchevskoy and Bezymianny volcanoes, as well as combinations of those factors.

The rest of the paper is structured as follows; we first describe the GPS data in section 4.2, where the GPS network and the data processing, and some key observations from the resulting time series are detailed. Following this, we investigate long-term, long-wavelength subsidence and test our hypotheses for driving forces in section 4.3. In this section we introduce models we apply and remove from the velocity field and investigate results each of these operations yields. In section 4.4, we analyze short term displacements related to individual eruptions and put constraints on a location for a shallow magma storage area below, or even within Bezymianny's edifice. We discuss our results in section 4.5 and present our conclusions in section 4.6.

4.2 GPS Data

4.2.1 GPS Network

The geodetic network at Bezymianny consists of 8 continuous and 6 campaign sites (Figure 4.1, Table 4.1); all newly installed during the PIRE-Kamchatka project beginning in 2005. The network is intended for volcano deformation studies and thus provides good station coverage in both near and far field of Bezymianny Volcano. Additional stations were planned to the north of Bezymianny to discriminate local deformation from activity at Kluchevskoy Volcano. However, logistical constraints made it impossible to implement this part of the network.

The continuous sites are equipped with concrete pylons topped with SCIGN antenna

mounts (Figure 4.2A,C). The pylons were anchored in rock where available, but in most cases were anchored in soil more than 1 meter below the surface. The exception was BZ09, which featured a smaller mount directly into rock. Steel enclosures or other shelters at the sites housed the receiver and batteries. Data were downloaded during annual service visits, during which we also changed batteries at the sites. Most of the campaign benchmarks are steel pins cemented in stable rock (Figure 4.2B) and were first measured in 2005. Originally, the campaign sites BZ00 and BZ05 were intended for continuous observations and were built in the same fashion as the continuous sites. Logistical problems and/or concern of vandalism, however, prevented the permanent installation of receivers at these sites and they were measured annually during field campaigns together with the other campaign sites.

The continuous sites, and BZ00 and BZ05, have their earliest measurements in summer 2006. Some stations suffer from significant data gaps (Figure 4.3) due to power failures and animal damage (bear attacks). Since 2009 several sites have been converted to solar powered operation. While the sites were intended to run only throughout the time of the project, solar power makes long-term operation of the sites feasible. At the moment, 4 sites (BZ01, BZ03, BZ04, BZ06) remain in operation through KBGS and IVS, powered entirely or mainly by solar power.

In addition to the data from the Bezymianny network, KBGS provided data from their regional KAMNET network (Figure 4.1, upper left inset). We use these data to get a sense for far field background velocities. ES1 is used as a reference station. Other stations do not qualify for such use as they are affected by inexplicable offsets (MIL1, likely an antenna change) or offsets due to earthquakes (TIG). The station KLU in the village of Kluchi was operated until 26 October 2008 when the benchmark was destroyed during construction. A new station (KLUC) was installed on 27 October 2008. KLUC shows similar long term trends as KLU (Figure 4.3). However, due to a lack of overlap of observations at KLU and KLUC we do not combine the data and for velocity estimates we refer to data from KLU only.

4.2.2 GPS Data Processing

We use the GIPSY/OASIS II software (Gregorius, 1996) developed at NASA's Jet Propulsion Laboratory (JPL) to compute Precise Point Positioning solutions (Zumberge et al., 1997) for the GPS data. We analyze the GPS data together with data from all available continuous and campaign GPS sites in north-west North America and north-east Asia to generate time series of daily positions (Figure 4.3). Details on parameter estimation are given in Freymueller et al. (2008) and Freymueller and Kaufman (2010). Our data analysis strategy is described in Fu and Freymueller (2012). To estimate station velocities and their uncertainties assuming a power-law noise model, we use the time series analysis software CATS (Williams, 2008) and give results relative to stable Eurasia as defined by Argus et al. (2010) (Table 4.2, Figure 4.4A).

We also estimated station positions for BZ09 kinematically at each epoch (30 s intervals) using BZ06 or BZ03 as base station and processed the data similar to Grapenthin et al. (2012). However, the resulting time series show no significant explosion related deformation above background noise so we will not report further details on this work.

4.2.3 Time Series Observations

The main and most perplexing observation from the time series is that a region greater than 50 km in radius, encompassing the entire KGV, is subsiding rapidly. Figure 4.3 illustrates this, showing vertical position time series for the continuous sites. All sites in the Bezymianny network subsided rapidly over the entire study period at relatively uniform rates between about 8 and 12 mm/yr (Table 4.2). The campaign sites BEZD and KAMD subside at less than 7 mm/yr and the continuous site BZ08, built on a mound of softer soil, subsides by 15 mm/yr. Note that we ignore BEZH due to inconsistent measurements in the vertical component for 2005 and 2006 compared to the rest of the campaign results and its close proximity to BZ00, which shows position changes more consistent with the rest of the network.

The KAMNET sites in Kluchi (KLU/KLUC, about 42 km to the NNE) and Mayskoe (MAYS, about 45 km to the NW) show similar but slightly slower subsidence at respective rates of 4.3 and 5.3 mm/yr. Even the more distant KAMNET site in Esso (ES1, about 120 km

to the E) subsides at about 2.1 mm/yr. The spatial variations of these subsidence rates do not show an obvious relationship in the position of the sites relative to Bezymianny Volcano but indicate that the main signal source is limited to the KGV. Pinpointing this down to a simple, small scale signal source is difficult as the rate of relative horizontal motion is small (Table 4.2).

The second – equally perplexing – observation from the time series is that most of the GPS sites do not show variations in their horizontal or vertical motions that correlate with the times of the eruptions (Figure 4.3, eruptions are marked by vertical gray lines). An exception is the late 2006 eruption, which induced a small signal at several sites (Figure 4.3). The time series prior to the event, however, are too short to make a definitive statement given the small signal amplitude.

The site BZ09, located only 1.5 km from the Bezymianny dome, does show small variations in motion that correlate with the eruptions at 2007.36, 2008.64, and 2010.42 (times are given in decimal years). In the months before an eruption, the site shows a tendency to move northward at a rate faster than average, and then move southward again at the time of the eruption. This pattern would be expected from the pressurization and depressurization of a magma source located near the summit of the Bezymianny dome. However, the variations (∼1 cm) are close to the level of noise.

Two additional stations show motion that deviates from average trends at times of eruptions. BZ07 moves rapidly south during and after the eruption in 2008.64 and then continues to follow the pre-eruptive trend. Since BZ08, the nearest site to BZ07, is not operational during this time and no other station of the network shows similar motion, we assume this motion was very local and coincided with the eruption rather than being triggered by the event. MAYS shows a very interesting pattern of slight eastward motion prior to the 2009.96 eruption. During and after the event the site moves first west, then back east, and finally re-assumes the prior long-term trend with no visible static offset. If this signal was volcanic in origin, it would indicate deep deflation prior to the 2009.96 event and then immediate recharge of this deep pressure source. This interpretation remains speculative since station KLUC at a similar distance to the KGV does not show significant deformation during this time period (displacement at KLUC would be expected in the north component for most volcanic sources, Figure 4.3).

In the following two sections we analyze and interpret these main observations. First, we will work through tectonic, surface load and volcanic source processes that could explain the long-term, long-wavelength subsidence. Following this, we limit the range of magma source parameters that could explain the observed motion at BZ09 during the individual eruptions.

4.3 Long-Term, Long-Wavelength Subsidence

In this section we investigate the main sources that could induce regional subsidence on the scale we observe at Bezymianny: strain accumulation at a subduction zone, loading deformation due to deposition of volcanic products and deformation due to a volcanic source. None of these processes is particularly well understood in this region, subduction strain accumulation certainly being the best measured and modeled based on GPS data (Bürgmann et al., 2005). However, first order approximations based on conservative model parameter definitions will allow us to identify which of these processes dominates and gives the best explanation of the observations.

4.3.1 Tectonic Displacements

Tectonically, Kamchatka is part of the Okhotsk micro plate (Apel et al., 2006). While the exact motion of this plate is somewhat controversial and poorly constrained (e.g., Shestakov et al., 2011), Kamchatka clearly moves independently from the North American and Eurasian plates. In addition to the resulting rotational component, the Pacific plate subducts beneath Kamchatka at a rate of $\sim$80 mm/yr (e.g., Bürgmann et al., 2005) which induces active deformation south of the intersection with the Aleutian trench ($<$56° N). Vertical motions are expected from such strain accumulation at subduction zones (Savage, 1983). Inverting interseismic GPS data, Bürgmann et al. (2005) proposed models for the plate interface of the subduction zone and the related slip along these fault models. We apply these models and select one (model 5) to eliminate interseismic strain that accumulates over the time of our observations. Figure 4.4A shows in colored vectors the site velocities (blue: horizontal, red: vertical) inferred from time series spanning 2005 to 2010 (KLU: 2005-2008) with respect to stable Eurasia (Argus et al., 2010). The white and black vectors in the same figure show velocities of the overriding plate induced by the underthrusting

Pacific plate as proposed by Bürgmann et al. (2005, Table 2 model 5). This two-fault model is outlined in gray in Figure 4.4A. Although fully modeled, only a small part of the southern plate interface model is visible in the figure. We clearly see a reduction in predicted horizontal velocity with increasing distance from the trench (Figure 4.4A, white). The relative motion between the Bezymianny network and ES1 is about 2-3 mm/yr, which shows that without removing this model from the velocities a bias would be introduced in the horizontal velocities of the Bezymianny network when we use any of the more distant sites as a reference station. More importantly, however, the predicted vertical motion at the Bezymianny network is virtually zero and hence does not explain any of the subsidence we observe. Slight subduction related modeled uplift is plotted as black vectors in Figure 4.4A. Nevertheless we can use this model to correct for interseismic velocities.

Subtracting the predicted subduction zone velocities from the velocities with respect to stable Eurasia gives the white and black vectors in Figure 4.4B. This approximates the motion of the Okhotsk plate relative to stable Eurasia. To eliminate this component, we subtract the residual motion at ES1 (vectors in Figure 4.4B) from the Bezymianny network including stations MAYS and KLU. The result are the colored vectors in Figure 4.4B which we do not show for PETS as it is not relevant for our study. The plotted uncertainties are propagated from the original uncertainties shown in Figure 4.4A with the horizontal uncertainties for ES1 added in quadrature. Note that the vertical motion at ES1 is not removed in Figure 4.4B to visually stress, again, the extent of the subsidence that persists after tectonic correction (5-15 mm/yr, Table 4.2). The directionality of the residual horizontal velocities (up to 6 mm/yr, Table 4.2) does not suggest an obvious single signal source and may be a combination of rotational difference between ES1 and the Bezymianny network (likely small, and systematic across the network) and an unmodeled tectonic component.

4.3.2 Surface Load Models

To understand the cause of the rapid network wide subsidence observed for the Bezymianny network and to avoid biases in the estimation of a volcanic source (Grapenthin et al., 2010), we test whether destruction of the pre-1956 edifice, the rapid rebuilding of Bezymianny's dome, and the reoccurring pyroclastic flow deposits since then could induce displacement rates large enough to explain the observations. We include the impact of the

ongoing rapid build-up of Kluchevskoy Volcano and the 2.2 km^3 of material erupted during the 1975 Tolbachik fissure eruption (Fedotov and Markhinin, 1983; Fedotov et al., 2010).

To model the response of the crust to changes in surface load, we assume a half-space of Newtonian viscosity overlain by an elastic plate as Earth model. Recent displacement rates are estimated from the Green's function derived by Pinel et al. (2007, Equation A3), which are implemented in the framework CrusDe (Grapenthin, 2007) used for our simulations. For simplicity, we approximate all loads as (combinations of) disk loads (Figure 4.5). Individual disk heights are determined by volume redistribution based on the geometric shape of the feature, e.g., the Bezymianny dome is approximated by a half sphere, and Kluchevskoy Volcano by a cone (see Table 4.3 for all load values). The density of each load is assumed to be 2600 kg/m^3.

The growth rate for Kluchevskoy Volcano was inferred by calculating the volume for a cone starting at 1400 m asl with a base radius of 7 km and a height of 3400 m. When we divide the resulting total volume by the 7000 years of eruptive activity, we get a growth rate of 0.0245 km^3/yr. This is very similar to a rate of 0.0231 km^3/yr that can be inferred from the annual mass output of Kluchevskoy Volcano given by Fedotov et al. (2010, assuming a density of 2600 kg/m^3 for basalt).

We have to make several assumptions on crustal properties. We assume a 30 km effective elastic plate thickness (considering the assumption of a large magma body below that depth), an effective Young's modulus of $E = 80$ GPa, and a Poisson's ratio of 0.25. The mantle is assumed to have a density of $\rho_m = 3100$ kg m^{-3} and a viscosity of $\eta = 4 \times 10^{19}$ Pa s (Turcotte and Schubert, 2002). These parameter values result in a visco-elastic relaxation time $\tau_{ve} = 2\eta/E \sim 32$ yr (Turcotte and Schubert, 2002). Given the short wavelength of the loads (<30 km) compared to the assumed elastic thickness (30 km), we can neglect any viscous effects from deeper in the mantle. This effect must be taken into account if compensation of the load due to the build-up of the entire KGV was modeled. While this may contribute significant deformation, the long-term load history is too poorly constrained to create a realistic model.

Due to their greater distance from the GPS stations, we estimate current displacement rates induced by the 1975–76 Tolbachik products and activity at Kluchevskoy Volcano on a 1×1 km grid (Figure 4.5, map box limits model region). To reach a steady state velocity

for the ongoing build-up of Kluchevskoy Volcano, we run this simulation over the last 200 years. The Tolbachik loads are added at model time step 165 (real-time year 1975). The velocities at grid nodes closest to station coordinates at model time 200 are the estimated velocities for year 2010. The velocities induced by Bezymianny products are estimated separately on a 0.5×0.5 km grid (Figure 4.5, black box indicates model region) and, since the method of Green's functions requires linear behavior, added to the results for Tolbachik and Kluchevskoy (see electronic supplements 1,2).

The results of these simple experiments that assume a conservative Earth model indicate that loading cannot be neglected when we try to understand the displacement field at Bezymianny (Figure 4.6, Table 4.4). However, the maximum modeled load induced subsidence rate of 3.1 mm/yr at BZ09 is still small compared to the observed values. For the more distant sites KLU and MAYS the model still predicts 1.2 mm/yr of subsidence (ES1: 0.4 mm/yr); this is mainly due to Kluchevskoy's ongoing growth. With such small rates in the vertical field, displacement rates in the horizontal field are negligible (fractions of mm/yr, see Table 4.4) and the surface load modeling, while inducing a complex deformation pattern, does not clarify the observed complex horizontal velocities at Bezymianny.

4.3.3 Volcanic Sources

Having eliminated subduction and surface loading as main contributers to the observed subsidence rates at Bezymianny, we will now assess the likelihood of a volcanic source inducing such regional scale deformation as indicated by our observations. Deep volcanic inflation over similar-sized regions has been observed before in South America (Pritchard and Simons, 2004a; Fournier et al., 2010), which suggests that we may be observing a similar phenomenon.

Some tests with forward models using a deep pressure point source (Anderson, 1936; Yamakawa, 1955; Mogi, 1958) and an oblate spheroid (Yang et al., 1988; Battaglia et al., 2012) yield good fits to the vertical deformation field, but significantly overestimate displacements in the horizontal field. A simple source that generates large vertical and small horizontal displacements is a sill, which we model as a closing tensile fault (Okada, 1992).

Effectively, it is possible to fit the observed subsidence with any sill in the lower crust that changes in volume by about the amounts estimated for the annual volume output of

the KGV (0.023-0.057 km^3/yr, converted to volumes from mass estimates given by Fedotov et al. (2010) assuming density of basalt). We attempted various kinds of source estimations / data inversions including grid searches (similar to Grapenthin et al., 2012) and simulated annealing (e.g., Cervelli et al., 2001). In these procedures we evaluated model fits with respect to ES1 for a range of subsets of the data:

- load model removed / not removed

- only stations > 4 km away from Bezymianny

- including / excluding KLU, MAYS

- using only vertical or full 3D velocities

Except for a geometry preference toward a deep, large sill, rather than spherical sources, the results to these inversions remain inconclusive. In fact, Figure 4.7 presents histograms from these experiments that indicate the spread of best fitting parameter sets. We ran 5,000 experiments on each set of input data listed above (see caption of Figure 4.7). The parameters for the sill were limited to a 40×40 km area around Bezymianny Volcano, depths from 1-50 km, lengths and widths from 1-40 km, opening from -10-0 m, strike from -180-180°, and dip from 0-90°. Best fits to the data can be found for any of these subsets, the tendency appears for the sill to have its center of gravity roughly south and anywhere between east and west from Bezymianny at rather large depth. Misfits can be minimized either with a very small area sill (no impact on data) or a wide and long sill with small opening, striking roughly north-south and dipping at angles smaller than 20°.

This seems to contradict previous findings from seismology and seismic tomography. Fedotov et al. (2010, their Figure 19) propose a complex plumbing system underneath the entire KGV with a deep source at about 30 km beneath Kluchevskoy Volcano feeding into intermediate storage regions under Bezymianny and Kluchevskoy, respectively. Koulakov et al. (2011) and Koulakov et al. (2012, this volume) find a robust deep velocity anomaly under Kluchevskoy, which they interpret as a pool of magma. If the Fedotov et al. (2010) description of the plumbing system is accurate, our results imply that the pressures change very little with time in all of the shallow bodies, so that only the depressurization of the deep body induces significant deformation. As the KGV shows sustained high levels of

volcanic activity, continuous withdrawal from a deep, common magma storage region seems plausible. Therefore, we test the hypothesis of deflation of a deep sill located underneath Kluchevskoy and constrain this model in accord with long-term seismicity (e.g., Figure 4.8):

- EW extent: 9.46 km

- NS extent: 12.75 km

- depth of fault plane: 33.5 km

- dip: 13° E

- strike: 200° N

The remaining unconstrained parameter is the opening for which we perform a grid search from -1 to 0 m in 0.001 m intervals. We determine that -0.22 m/yr (-0.16 m/yr when fitting the load corrected data) of opening fits the vertical displacements best. This results in an annual volume change of $0.027\,km^3$ ($0.019\,km^3$/yr for load corrected opening), which is a reasonable value compared to the productivity of $0.023\,km^3$/yr of Kluchevskoy that can be derived from the mass output given by Fedotov et al. (2010). The productivity rate of the entire region is given as 150 Gt/yr (Fedotov et al., 2010), which converts to $0.057\,km^3$ assuming a density of $2600\,kg\,m^{-3}$ (basalt).

The predictions of this model (Figure 4.9), along with the velocity field relative to ES1, are shown in Figure 4.10A. The horizontal residuals in Figure 4.10B suggest some remaining, southward motion of the entire network. Only the campaign site BEZR, a station on a ridge in the pyroclastic flow path, and the continuous site BZ08, the continuous station with fewest data (Figure 4.3), do not conform with this overall trend. The coherence of the remaining horizontal residuals may indicate a small ($\sim 5 - 7$ mm/yr) residual motion of the Bezymianny network relative to ES1 on the opposite side of the Central Kamchatka Depression. This residual motion is roughly trench-parallel, so it is likely not related to any shortcoming in the subduction strain model. However, it could represent a small shear motion across the Central Kamchatka Depression.

This gain in consistency in the horizontal component supports the assumption of long term deformation at Bezymianny being driven by the deep sill-like source under Kluchevs-

koy. Our solution is non-unique, however, considering the uncertainties in the velocities, the long wavelength and small amplitudes of deformation, our model seems to provide a reasonable and conservative explanation for the observations. Data spanning the entire KGV would be required to constrain a unique best-fitting model.

4.4   Short-Term Displacements: Individual Eruptions

The daily positioning time series for continuous GPS stations around Bezymianny show no clear signal in either vertical or east component related to explosive events from 2005 to 2010 (Figure 4.3). In the north component only BZ09 shows slight variations indicating northward motion prior to eruptions at 2006.98, 2007.36, 2008.64, 2010.42 and southward motions following these events (if the antenna was not destroyed by ballistics as was the case during the 2010.42 event) and likely also at 2009.96. This means all events for which we have data at this site appear to induce subtle motion in the north component at this location. While this motion stands out above background it is too small to infer eruption related offsets that would enable source modeling. Even if we would do this and dealt with large uncertainties, the result would still only be a single observable which is not sufficient to derive a unique source. Instead, we follow Grapenthin et al. (2012) in their approach of analyzing the sensitivity of a GPS network to test likely source locations for their detectability and limit the seemingly infinite parameter space to a more informative range.

Several depths have been previously proposed for reservoirs located under Bezymianny (e.g., Fedotov et al., 2010; Thelen et al., 2010; Koulakov et al., 2011). Source geometries, however, have not been inferred so we assume the most simplistic model under Bezymianny's summit: a pressure point source, or Mogi source (Anderson, 1936; Yamakawa, 1955; Mogi, 1958). The simple analytical model requires only source depth, and source strength or volume change in addition to horizontal location, which we constrain.

At fixed horizontal locations – one directly under the summit, the other one in the blast zone about 2 km to the south-east of Bezymianny (West, 2012, this volume) – we vary the source depth and at each depth level we search for the minimum volume change required to induce ≥ 1 cm of horizontal or vertical displacement. Doing this for each station produces the colored contours in Figure 4.11. The blue-shaded region in Figure 4.11A,B in-

dicates depth-volume change combinations that induce at least 1 cm horizontal or vertical displacement at a minimum of one station, which we can reject based on the lack of deformation observed. White areas of the plot indicate depth–dV combinations that would produce deformation too small to observe, and we can neither confirm nor reject any such model. Previous work proposed sources at shallow levels (1 km, 7 km Thelen et al., 2010), mid-crustal levels (10 km, 18 km Fedotov et al., 2010), and at the base of the crust (25-30 km Fedotov et al., 2010; Koulakov et al., 2011), which we mark with the horizontal dashed gray lines in Figure 4.11.

In addition to these proposed source depths, we can plot ranges for estimated volume changes. The lava flows from 1984-2007 (Zharinov and Demyanchuk, 2011) are marked by the vertical dashed black lines indicating $2.5 - 8.0 \times 10^{-4}$ km^3 as minimum and maximum volume, respectively. Pyroclastic flow volumes from $0.2 - 2.0 \times 10^{-2}$ km^3 are given by Girina (2012, this volume) and marked by the vertical solid black lines. These volumes, however, are overestimates in terms of source volume change as they are not a dense rock equivalent and contain unspecified portions of non-juvenile material (i.e., dome material and other lithics).

Using the values for volumes and depths specified above, we would not record any deformation due to a deep spherical source for such small volume changes of Bezymianny eruptions. If any of the eruptions was fed straight from the basaltic layer at 18 km proposed by Fedotov et al. (2010), we would see this only in the vertical component for volume changes >0.01 km^3, and would expect to observe this at all stations across the network. As we do not see this, we rule out direct involvement of this source for larger events. A similar decision follows for sources suspected at 7 and 10 km as we do not observe consistent network wide deformation at times of explosions in both the vertical and horizontal field.

What we do observe is subtle deformation in the horizontal (north component) at BZ09 only. If we now combine the vertical and horizontal contours for the region highlighted in pink in Figure 4.11A,B, we get the plot in the inset in Figure 4.11A. The area highlighted in red shows the combinations of depth and volume change that would induce 1 cm or more motion in the horizontal at BZ09, but motion at or below the detection limit in the vertical at BZ09 and the horizontal at BZ03. We infer that a pressure point source at 0.25-1.5 km with a volume change of 1-4×10^{-4} km^3 may be involved in the eruptions. This

falls in the region of the shallow source within the edifice proposed by Thelen et al. (2010). The range of permissible volume changes lies around the lower limit of the 1984-2007 lava flow volumes (Zharinov and Demyanchuk, 2011). We emphasize again our assumption that this source is located straight underneath Bezymianny's dome summit at 55.9719°N, 160.5965°E.

A second plausible location for a shallow source is about 2 km to the south-east of the dome where particle motion plots of very long period seismic signals during eruptions on Dec. 16, 2009 (21:46:00 UTC) and May 31, 2010 (12:34:00 UTC) suggest a region involved in the explosive activity (West, 2012, this volume). If we repeat the exercise described above for this hypothetical horizontal source location, we get the sensitivity contours shown in Figure 4.12. While station BZ02 is most sensitive to this source and hence would be critical to confirm this source location, it was not operating during any of the events for which West (2012, this volume) hypothesizes this source location. Note that deformation at BZ09 induced by a point source at such a location would likely induce motion in both east and north component, rather than just the north component as we observed. More complex scenarios such as a dike could possibly limit the induced motion to the north component, though.

The inset in Figure 4.12A shows that a possible pressure point source could be located at 0.25-3.5 km depth changing in volume by about 0.6-1.5×10^{-3} km^3. These ranges are larger than before because of the increased distance between BZ09 and the source. Note that the depth range inferred for the summit source is included here and that shallower depths require smaller volume changes; i.e. there is a significant depth-volume change trade-off.

4.5 Discussion

The two striking observations from the GPS data for 2005-2010 are (1) rapid and continuous network wide subsidence, which diminishes in amplitude away from the KGV, but still appears to affect stations more than 40 km away (KLU, MAYS), and (2) the absence of a clear deformation pattern related to individual eruptions at stations other than BZ09 which, prior to and after explosions, shows slight deviations from the average motion in the north component. From our analysis above we infer that a deep sill at about 30 km

underneath Kluchevskoy constantly discharges material that may be fed into shallower reservoirs under Bezymianny and Kluchevskoy, respectively. A very shallow reservoir suggested by Thelen et al. (2010), likely within Bezymianny's edifice, appears to explain slight deformation during individual events which seem to be sourced from a mid-crustal reservoir with volume changes at or below the detection limit of our network. In the following we will discuss these findings individually.

4.5.1 Long-wavelength Subsidence: Deep Sill

The regional extent of the signal and therefore the dimensions of the volcanic source are certainly astonishing, yet similar observations have been made at other volcanoes, for example in South America (Pritchard and Simons, 2004a; Fournier et al., 2010). Those studies benefit from highly resolved spatial sampling InSAR techniques, which clearly show the extent of the deformation. For the KGV Pritchard and Simons (2004b) report deformation due to the 1975-76 Tolbachik lava flows from satellite data between 1992 and 2003, but cannot resolve deformation due to any of the eruptions at the KGV volcanoes during that period. Poor spatial and temporal coverage limits detection to larger signals in that region (Pritchard and Simons, 2004b). Within the PIRE-Kamchatka project several groups attempted InSAR analysis of more recent data for this region. The results remain similar to those of Pritchard and Simons (2004b). Lack of coherence due to snow cover for much of the year limits success and the small amplitude of the signal over such a large region poses another problem as atmospheric effects show similar behavior and hence make the signal hard to detect.

Various authors (e.g., Fedotov et al., 2010; Koulakov et al., 2011, 2012, and KBGS seismic catalog) have suggested a deep source under Kluchevskoy and, in fact, these findings largely constrain our source parameterization. Formal inversion procedures such as simulated annealing or simple grid searches fail due to the very regional nature of the signal, which our network samples very localized. In combination with a small signal amplitude, or rather, small change in signal amplitude across the network, these methods place the best fitting source at locations not in agreement with previous studies, observed surface activity, and seismic evidence. However, using the occurrence of seismicity and its spatial features as model constraints (Figure 4.8), we are able to limit the fundamental source ge-

ometry to a non-spherical source, and our inferred closing rate of the sill suggests a volume change of the source (0.019 - 0.027 km^3/yr) that agrees very well with long term production estimates for Kluchevskoy Volcano (0.023 km^3/yr) and is a factor of 2-3 smaller than the long term productivity of the entire group 0.057 km^3/yr (Fedotov et al., 2010). We should not put too much emphasis on the discrepancy with the productivity of the entire group as Fedotov et al. (2010) estimate this long term trend from all eruptions since 1930, which includes the 1956 Bezymianny eruption and the 1975-76 Great Tolbachik Fissure Eruption; events of a size we did not observe during our study.

A critical point about magma source location estimation is the depth–volume (here opening) trade-off for volcanic sources, meaning that a deep source with a large volume change induces displacements similar to a shallow source with less volume change. This is particularly important when we are not using the full 3-D displacement field. While we constrain the deep sill from seismic observations, Fedotov et al. (2010) also suggest a basaltic layer at about 18 km that may underlie parts of the KGV, which is supported by earthquakes during the 1975-76 Tolbachik eruption. In a test to see whether the source we put under Kluchevskoy would induce similar displacements at shallower depths, we vary depth and opening and calculate the χ^2 misfit between data and each of these sources. Figure 4.13 shows that the same source geometry at a depth of 18 km would result in a significant misfit. Shallower sources, of course, would result in an even larger misfit. Therefore, the constraints from seismicity and the inferred opening are robust.

Although we constrained our model based on information provided by other disciplines rather than inverting for the parameters giving the best model fit to the data, the resulting fit of model prediction to measurements is fairly good in both vertical and horizontal, i.e. the source generates small horizontal deformation. Subtracting the modeled velocities from the data results in residual horizontal velocities (Figure 4.10) that seem to gain coherence and may be explained either with a tectonic feature or maybe a shallower source at Kluchevskoy. An inversion for a point source did not yield any reasonable results. This may be revisited in the future when a better spatial distribution of data is available for this region and surface load effects as well as tectonics are better understood.

An important question that remains is where all the material goes that is continuously removed from such deep depths. As stated above, the removed volume of material agrees

well with the long term eruption rate of Kluchevskoy Volcano. But neither Kluchevskoy nor Bezymianny erupt continuously. This calls for an additional mid-crustal storage region underneath those two volcanoes, which is suggested by seismicity (Fedotov et al., 2010; Thelen et al., 2010; Koulakov et al., 2011). While we may actually record some long term mid-crustal inflation at Kluchevskoy (Figure 4.10), eruptions seem too frequent at Bezymianny to amount to enough detectable deformation (Figs. 4.11, 4.12). Additionally, compression and decompression of the magma at mid crustal depths may hide some of the mass transfer and result in less recordable deformation (Johnson et al., 2000; Rivalta and Segall, 2008).

To fully resolve the deep source under Kluchevskoy Volcano without relying on outside constraints, additional, regionally distributed continuous GPS stations will be necessary. Stations in between Bezymianny and Kluchevskoy, around Kluchevskoy, and in the far field (mainly east of Kluchevskoy and south of Bezymianny, at least 20 km from the volcanoes) are needed to better resolve the spatial limits of the deep source. GPS sites along the Central Kamchatka Depression, away from volcanic centers, would allow resolution of residual regional and local tectonics whose current contributions are not well quantified. Given the suggested complexity of the subsurface plumbing system of the KGV (Fedotov et al., 2010; Thelen et al., 2010; Koulakov et al., 2011, 2012), the quantity of data must provide spatial and temporal coverage large enough to allow to solve for more than one source (Turner et al., 2012, this volume) and migrating sources (Koulakov et al., 2012, this volume).

4.5.2 Co-eruptive Deformation: Shallow Reservoir

A very shallow storage region within Bezymianny's edifice was proposed by Thelen et al. (2010). They based this on a small aseismic area inferred from high-resolution earthquake locations and on fluid inclusions in plagioclase rims, which require magma storage at such shallow depths (Thelen et al., 2010, their pers. comm. with P. Izbekov). Since Thelen et al. (2010) only analyzed about 3 months of data from the 2007 eruptive sequence it is unclear whether this region is a transient or permanent feature. Lopez et al. (2012, this volume) find evidence for shallow degassing magma in 2007 and 2010. Since the gas samples were collected 1-3 months after the respective eruptions, the magma could have been a residual

in the conduit or associated with lava flow effusion (pers. comm. with T. López, 2012). On the other hand, this may suggest a more long-lived shallow reservoir, or at least an episodically active feature. Due to the repetitive nature of the slight eruption related deformation in the north component of BZ09 during our observation period of 5 years, we suggest this may be a more permanent feature. However, future improved observations with more sensitive instruments are necessary to answer this question with more certainty.

The volume changes of this storage region are near the detection limit of the network and are small compared to the volume of erupted products; comparable to or smaller than even the smallest 1984-2007 lava flows (Figure 4.11A,inset). This discrepancy between erupted material and apparent lack of volume change can be explained in several ways. Rivalta and Segall (2008) suggest that after removal of material from a pressurized, volatile rich magma, the lost volume is simply recovered through expansion of volatiles. This seems to work only in a closed system though as volatiles may simply escape during time of shallow storage when the system is open. As Bezymianny is an open system and constantly degassing, this pressure build-up might not occur.

Another possibility for volume-loss recovery is recharging of the shallow reservoir with material from depth (e.g, Grapenthin et al., 2012), or direct evacuation of material mostly from deeper regions, which seems supported by Turner et al. (2012, this volume) who model major and trace element as well as mineral data as a mixing of three different magmas. If the bulk of the material came from deeper (8-10 km) where Thelen et al. (2010), Fedotov et al. (2010), and Turner et al. (2012, this volume) suggest an intermediate storage region, the removal of magma at these depths could happen at network detection limits (Figure 4.11) and still agree with volumes of erupted material. This easily explains the lack of volume change in the shallow reservoir.

The fact that West (2012, this volume) recognizes small amplitude deformation in the seismic data located about 2 km to the south-east of Bezymianny's dome in the 1956 blast zone for eruptions in late 2009 and May 2010 deserves some attention. We do not think this is an actual shallow storage region as BZ09 shows deformation similar to prior events which is limited to the north component only. A very specific source geometry would be necessary to induce such deformation from this distance, which we consider unlikely. Deformation inferred from broadband seismometers suggests sub-mm displacements, which

we may not be able to detect at all. An explanation may be the transient pathways of fluid migration as opposed to well established conduit systems suggested by Koulakov et al. (2012). An improved record at BZ02 could help to clarify this (Figure 4.12).

4.6 Conclusions

Continuous and campaign GPS observations in a dense network of stations around Bezymianny Volcano, Kamchatka, show continuous subsidence at rapid rates between 8 and 12 mm/yr. This signal may range as far as about 40 km to the north (Kluchi) and to the east (Mayskoye) where we observe 4.3 and 5.3 mm/yr of subsidence, respectively. In time, this subsidence may be traced back to 1978-87 as an earlier study by Fedotov et al. (1992) suggests similar broad subsidence, although at smaller rates. Tectonic deformation related to build up of interseismic strain due to subduction of the Pacific plate to the east induces significant horizontal deformation in the network. According to the model of Bürgmann et al. (2005) vertical deformation due to subduction is negligible. A first order model of surface loading by eruptive products of the KGV explains a fraction of the subsidence signal and suggests that this signal source is non-negligible and future work should focus on deriving a better constrained Earth and load model for this region. The bulk of the vertical signal, however, is explained by a sill-like source under Kluchevskoy. This sill is at about 30 km depth, dips $13°$ to the south-east, and is about 9.5 km wide and 12.7 km long. We infer a closing rate of 0.22 m/yr, which results in a volume loss of $0.027\,\text{km}^3$ (0.16 m/yr and $0.019\,\text{km}^3$ respectively, considering surface loading). Additional stations in the near and far field are required to fully resolve the spatial extent and likely partitioning of this source.

From network sensitivity analysis, we limit the possible sources underneath the summit of Bezymianny that can induce slight deformation at BZ09 only to a shallow reservoir at about 0.25–1.5 km depth with a volume change of $1\text{-}4\times10^{-4}\,\text{km}^3$. Much of the material erupted at Bezymianny may be sourced from deeper mid-crustal reservoirs with co-eruptive volume changes at or below the detection limit of the GPS network. Installation of more sensitive instruments such as tiltmeters would lower the detection limit of the network and hence allow resolving more subtle co-eruptive motion.

Acknowledgements

Bibliography

Anderson, E. M., 1936. The Dynamics of the Formation of Cone-sheets, Ring-dykes, and Caldron-subsidences. Proceedings of the Royal Society of Edinburgh 56, 128–157.

Apel, E., Bürgmann, R., Steblov, G. M., Vasilenko, N., King, R., Prytkov, A., 2006. Independent active microplate tectonics of northeast Asia from GPS velocities and block modeling. Geophys. Res. Lett. 33, L11303.

Argus, D. F., Gordon, R. G., Heflin, M. B., Ma, C., Eanes, R. J., Willis, P., Peltier, W. R., Owen, S. E., 2010. The angular velocities of the plates and the velocity of Earth's centre from space geodesy. Geophysical Journal International 180, 913–960.

Battaglia, M., Cervelli, P. F., Murra-Muraleda, J. R., 2012. Modeling Crustal Deformation: a catalog of deformation models and modeling approaches. US Geological Survey Prof. Pap., in press.

Belousov, A., Voight, B., Belousova, M., 2007. Directed blasts and blast-generated pyroclastic density currents: a comparison of the Bezymianny 1956, Mount St Helens 1980, and Soufrière Hills, Montserrat 1997 eruptions and deposits. Bull. Volcanol. 69 (7), 701–740.

Bürgmann, R., Kogan, M. G., Steblov, G. M., Hilley, G., 2005. Interseismic coupling and asperity distribution along the Kamchatka subduction zone. J. Geophys. Res. 110, B07405.

Carter, A. J., Ramsey, M. S., Belousov, A. B., 2007. Detection of a new summit crater on Bezymianny Volcano lava dome: satellite and field-based thermal data. Bull. Volc. 69, 811–815.

Cervelli, P., Murray, M. H., Segall, P., Aoki, Y., Kato, T., 2001. Estimating source parameters from deformation data, with an application to the March 1997 earthquake swarm off the Izu Peninsula, Japan. Journal of Geophysical Research 106 (B6), 11,217–11,237.

Fedotov, S. A., Markhinin, Y. K. (Eds.), 1983. The Great Tolbachik Fissure Eruption. Cambridge University Press, Cambridge.

Fedotov, S. A., Zharinov, N. A., Gontovaya, L. I., 2010. The Magmatic System of the Klyuchevskaya Group of Volcanoes Inferred from Data on Its Eruptions, Earthquakes, Deformation, and Deep Structure. Journal of Volcanology and Seismology 4 (1), 3–35.

Fedotov, S. A., Zharinov, N. A., Sharoglazova, G. A., Demianchuk, Y. V., 1992. Deformations of the Earth's surface in the Klyuchi geodynamic polygon, Kamchatka, 1978-1987. Tectonophysics 202, 151–156.

Fournier, T. J., Pritchard, M. E., Riddick, S. N., 2010. Duration, magnitude, and frequency of subaerial volcano deformation events: New results from Latin America using InSAR and a global synthesis. Geochem. Geophys. Geosyst. 11 (1), Q01103.

Freymueller, J. T., Kaufman, A. M., 2010. Changes in the magma system during the 2008 eruption of Okmok volcano, Alaska, based on GPS measurements. Journal of Geophysical Research 115, B12415.

Freymueller, J. T., Woodard, H., Cohen, S. C., Cross, R., Elliott, J., Larsen, C. F., Hreinsdóttir, S., Zweck, C., 2008. Active Deformation Processes in Alaska, Based on 15 Years of GPS Measurements. In: Freymueller, J. T., Haeussler, P. J., Wesson, R. L., Ekström, G. (Eds.), Active Tectonics and Seismic Potential of Alaska. Geophysical Monograph. AGU, pp. 1–42.

Fu, Y., Freymueller, J. T., 2012. Seasonal and long-term vertical deformation in the Nepal Himalaya constrained by GPS and GRACE measurements. Journal of Geophysical Research 117, B03407.

Girina, O. A., 2012. Chronology of Bezymianny Volcano activity in 1956-2010. Journal of Volcanology and Geothermal Research, in review.

Gorshkov, G., 1959. Gigantic eruption of Volcano Bezymianny. Bull. Volc. 20 (1), 77–109.

Grapenthin, R., 2007. CrusDe: A plug-in based simulation framework for composable CRUStal DEformation simulations using Green's functions. Master's thesis, Berlin.

Grapenthin, R., Freymueller, J. T., Kaufman, A. M., 2012. Geodetic observations during the 2009 eruption of Redoubt Volcano, Alaska. Journal of Volcanology and Geothermal Research, Special Issue on the 2009 Redoubt Eruption, in press.

Grapenthin, R., Ofeigsson, B. G., Sigmundsson, F., Sturkell, E., 2010. Pressure sources versus surface loads : Analyzing volcano deformation signal composition with an application to Hekla volcano , Iceland. Geophys. Res. Lett. 37, L20310.

Gregorius, T., 1996. GIPSY OASIS II: How it works. self, University of Newcastle upon Tyne.

Johnson, D. J., Sigmundsson, F., Delaney, P. T., 2000. Comment on "Volume of magma accumulation or withdrawal estimated from surface uplift or subsidence , with application to the 1960 collapse of Kilauea volcano" by P. T. Delaney and D. F. McTigue. Bull. Volcanol. 61, 491–493.

Koulakov, I., Gordeev, E. I., Dobretsov, N. L., Vernikovsky, V. A., Senyukov, S., Jakovlev, A., 2011. Feeding volcanoes of the Kluchevskoy group from the results of local earthquake tomography. Geophys. Res. Lett. 38, L09305.

Koulakov, I., Gordeev, E. I., Dobretsov, N. L., Vernikovsky, V. A., Senyukov, S., Jakovlev, A., Jaxybulatov, K., 2012. Variable feeding regimes of the Kluchevskoy group volcanoes (Kamchtaka, Russia) derived from time-dependent seismic tomography. Journal of Volcanology and Geothermal Research, in review.

Lopez, T. M., Ushakov, S., Izbekov, P., Tassi, F., Werner, C., Cahill, C., 2012. Constraints on magma processes, subsurface conditions, and total volatile flux at Bezymianny Volcano in 2007-2010 from direct and remote volcanic gas measurements. Journal of Volcanology and Geothermal Research, in review.

Malyshev, A. I., 2000. Life of the volcano (in Russian). Ural Division of the Russian Academy of Sciences.

Mogi, K., 1958. Relations between eruptions of various volcanoes and the deformations of the ground surface around them. Bull. Earthquake Res. Inst. Univ. Tokyo 36, 99–134.

Okada, Y., 1992. Internal deformation due to shear and tensile faults in a half-space. Bull. Seis. Soc. Am. 82 (2), 1018–1040.

Pinel, V., Sigmundsson, F., Sturkell, E., Geirsson, H., Einarsson, P., Gudmundsson, M. T., Högnadóttir, T., 2007. Discriminating volcano deformation due to magma movements and variable surface loads: Application to Katla subglacial volcano, Iceland. Geophys. J. Int. 169, 325–338.

Pritchard, M. E., Simons, M., 2004a. An InSAR-based survey of volcanic deformation in the central Andes. Geochemistry Geophysics Geosystems 5 (2), Q02002.

Pritchard, M. E., Simons, M., 2004b. Surveying Volcanic Arcs with Satellite Radar Interferometry: The Central Andes, Kamchatka, and Beyond. GSA Today 14 (8), 4–11.

Rivalta, E., Segall, P., 2008. Magma compressibility and the missing source for some dike intrusions. Geophys. Res. Lett. 35, L04306.

Savage, J. C., 1983. A Dislocation Model of Strain Accumulation and Release at a Subduction Zone. Journal of Geophysical Research 88 (B6), 4984–4996.

Shestakov, N. V., Gerasimenko, M. D., Takahashi, H., Kasahara, M., Bormotov, V. A., Bykov, V. G., Kolomiets, A. G., Gerasimov, G. N., Vasilenko, N. F., Prytkov, A. S., Timofeev, V. Y., Ardyukov, D. G., Kato, T., 2011. Present tectonics of the southeast of Russia as seen from GPS observations. Geophysical Journal International 184, 529–540.

Thelen, W., West, M., Senyukov, S., 2010. Seismic characterization of the fall 2007 eruptive sequence at Bezymianny Volcano , Russia. Journal of Volcanology and Geothermal Research 194 (4), 201–213.

Turcotte, D. L., Schubert, G., 2002. Geodynamics. Cambridge University Press.

Turner, S. J., Izbekov, P., Langmuir, C., 2012. The magma plumbing system of Bezymianny Volcano: Insights from trace element whole-rock geochemistry and amphibole compositions. Journal of Volcanology and Geothermal Research, in review.

Wessel, P., Smith, W. H. F., 1995. New version of the Generic Mapping Tools released. Eos Trans. AGU 76 (33), 329.

West, M. E., 2012. Recent eruptions at Bezymianny volcano – a seismic comparison. Journal of Volcanology and Geothermal Research, in review.

Williams, S. D. P., 2008. CATS: GPS coordinate time series analysis software. GPS Solutions 12, 147–153.

Yamakawa, N., 1955. On the Strain Produced in a Semi-infinite Elastic Solid by an Interior Source of Stress. Zisin (J. Seis. Soc. Japan), 84–98.

Yang, X. M., Davis, P. M., Dieterich, J. H., 1988. Deformation from Inflation of a Dipping Finite Prolate Spheriod in an Elastic Half-Space as a Model for Volcanic Stressing. Journal of Geophysical Research 93, 4257–4549.

Zharinov, N. A., Demyanchuk, Y. V., 2011. Assessing the volumes of material discharged by Bezymianny Volcano during the 1955-2009 period. Journal of Volcanology and Seismology. Journal of Volcanology and Seismology 5 (2), 100–113.

Zumberge, J. F., Heflin, M. B., Jefferson, D. C., Watkins, M. M., Webb, F. H., 1997. Precise point positioning for the efficient and robust analysis of GPS data from large networks. J. Geophys. Res. 102 (B3), 5005–5017.
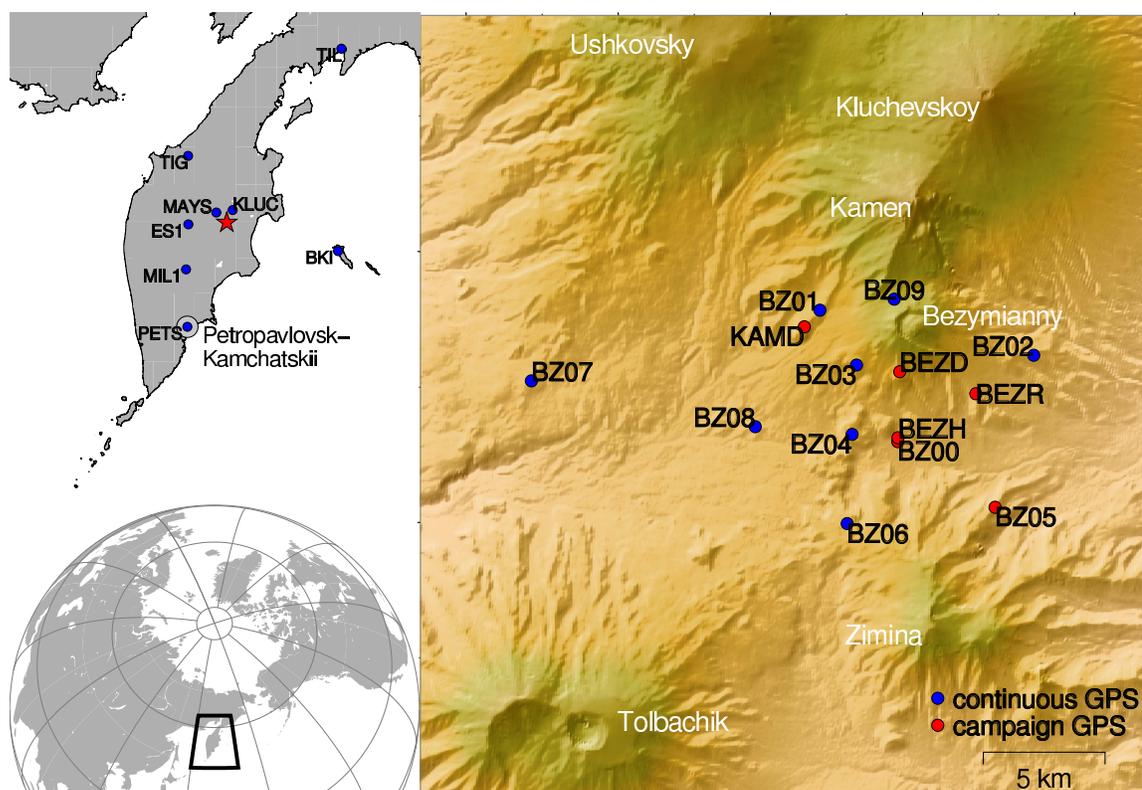
Figure 4.1: Regional setting and available GPS data from Bezymianny Volcano. World map (left bottom) outlines Kamchatka which is shown in the top left inset. Blue dots mark KAMNET continuous GPS stations. Red star marks location of the KGV. Right panel shows topographic map of the study region and location of PIRE GPS stations. Volcanoes are named in white text. Note the horseshoe-shaped crater with a new dome at Bezymianny.

Figure 4.2: Photos of continuous and campaign GPS installations. **(A)** Continuous site BZ08 in summer of 2010. In the background: Kluchevskoy with a small ash plume to the left, Kamen in the middle, and Bezymianny to the right and degassing. **(B)** Campaign site BEZR with spike mount setup and Trimble NetRS receiver in 2010. **(C)** Continuous site BZ06 with solar setup installed in 2010. The antenna is mounted on a concrete pylon, batteries and receiver are housed in the protective enclosure in the center, 4 solar panels were installed on 2 well anchored masts to keep them in place during high winds in that area. Bezymianny's dome steams in the background, which is the normal state.
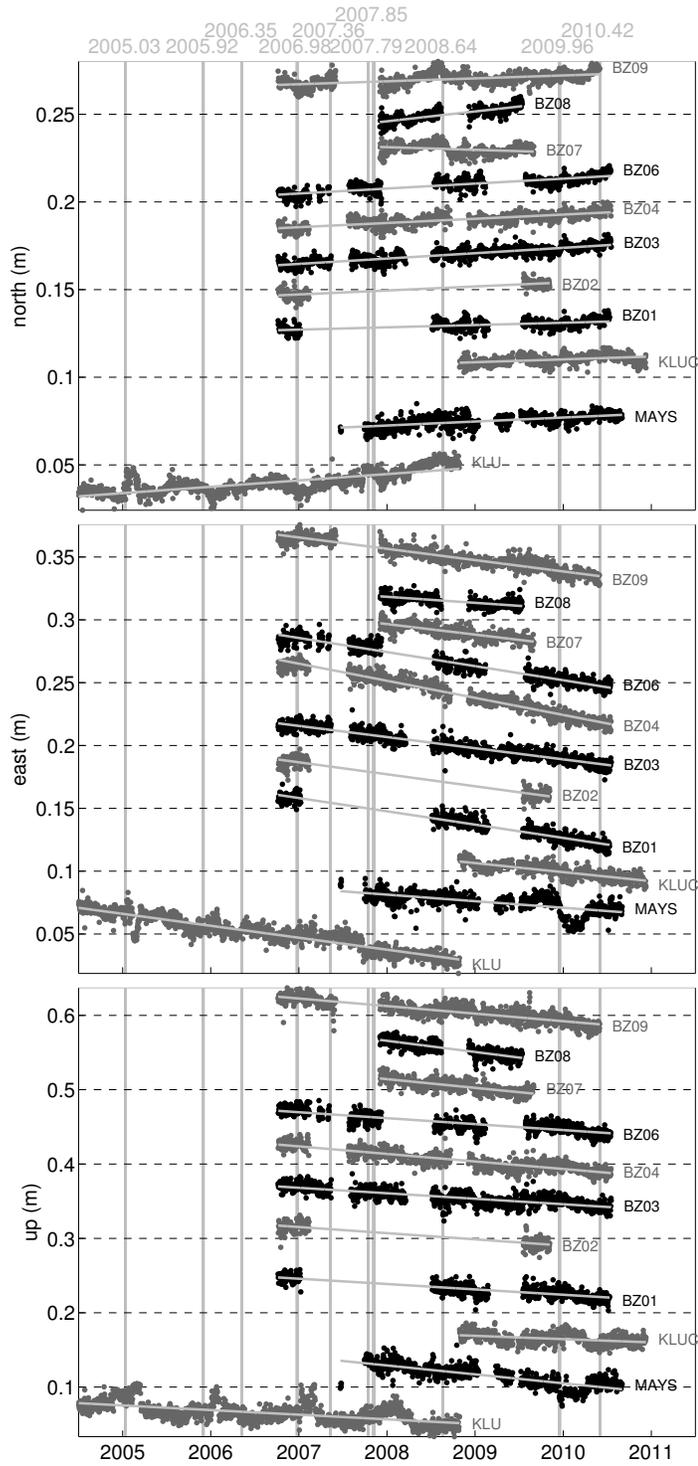
Figure 4.3: Time series relative to Eurasia (Argus et al., 2010) and linear trends of continuous GPS stations from 2005-2011 in the KGV. Vertical gray lines indicate eruptions of Bezymianny. Times for individual eruptions are given in decimal years above the top panel. Long-term trends in the north and east component are mostly due to motion of the Okhotsk plate and subduction of the Pacific plate to the east. Note the network wide subsidence in the vertical component. BZ09 deviates slightly from the long term trend around eruption times in the north component. BZ07 shows curious motion in the north component during and shortly after eruption 2008.64; likely not related to the eruptive activity. MAYS moves prior to and following the 2009.96 event, but it remains speculation whether the eruption actually induced motion at MAYS since KLUC does not show significant motion during this time period although it is an equal distance from the volcano.
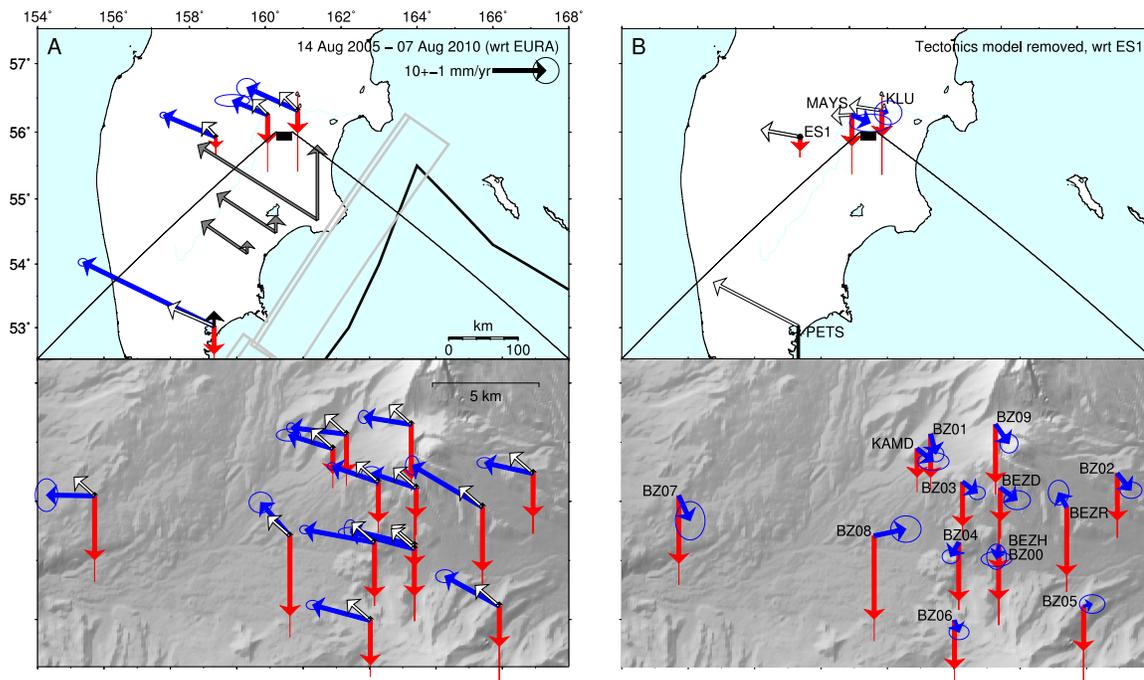
Figure 4.4: Velocities inferred from 2005-2010 time series for central Kamchatka and Bezymianny Volcano. **(A)** Colored vectors (blue: horizontal, red vertical) show site velocity calculated from 14 Aug 2005 – 07 Aug 2010 relative to stable Eurasia. Arrows are tipped with associated uncertainties given at the 95% level. White and black vectors are the tectonic model predictions due to subduction of the Pacific plate based on the model of Bürgmann et al. (2005, Table 2, model 5a and 5b). Gray vectors show tectonic motion for hypothetical stations, which illustrates the decay of deformation with distance from the trench. The Bürgmann et al. (2005) 2 plate model is outlined in gray, next to an approximation of the surface expression of the trench (black). Inset shows data for the Bezymianny region. White and black vectors are the tectonic model predictions. Note that vertical predicted motion due to tectonics is plotted but negligible at this distance from the trench. **(B)** White and black vectors are residuals of data minus model given in Panel A. Colored vectors station velocities with respect to stable ES1. Note that these values are only given for stations whose velocities are to be modeled later (PETS excluded). Data relative to ES1 show clear network wide subsidence extending northwards to KLU and westwards to MAYS. Horizontal velocities seem highly uncorrelated in the Bezymianny network.
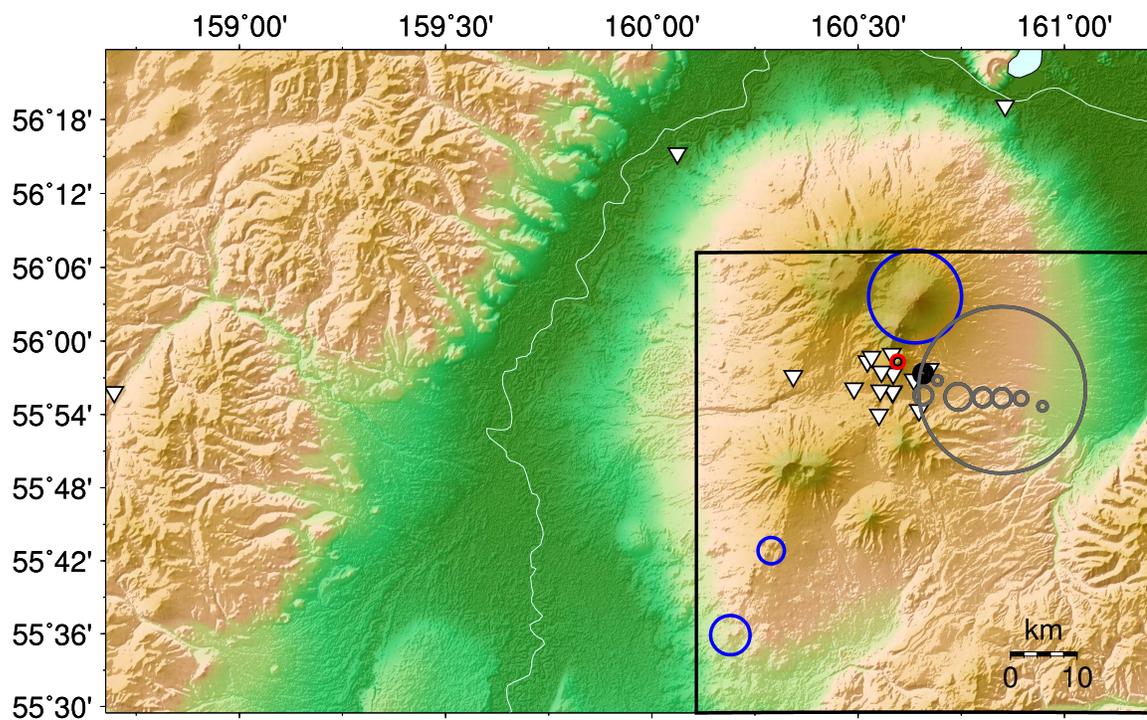
Figure 4.5: Spatial distribution of disks used to estimate velocities due to changes in surface loads listed in Table 4.4. Precise definitions of the disk values are given in Table 4.3. The map boundary corresponds to the area for which the Kluchevskoy and Tolbachik loads (blue circles) were modeled on a in 1×1 km grid. The black box outlines the area for which subsidence due to the Bezymianny loads (gray: 1956 deposits, red: 1956 edifice removal, black: post 1956 products) was modeled on a 0.5×0.5 km grid.
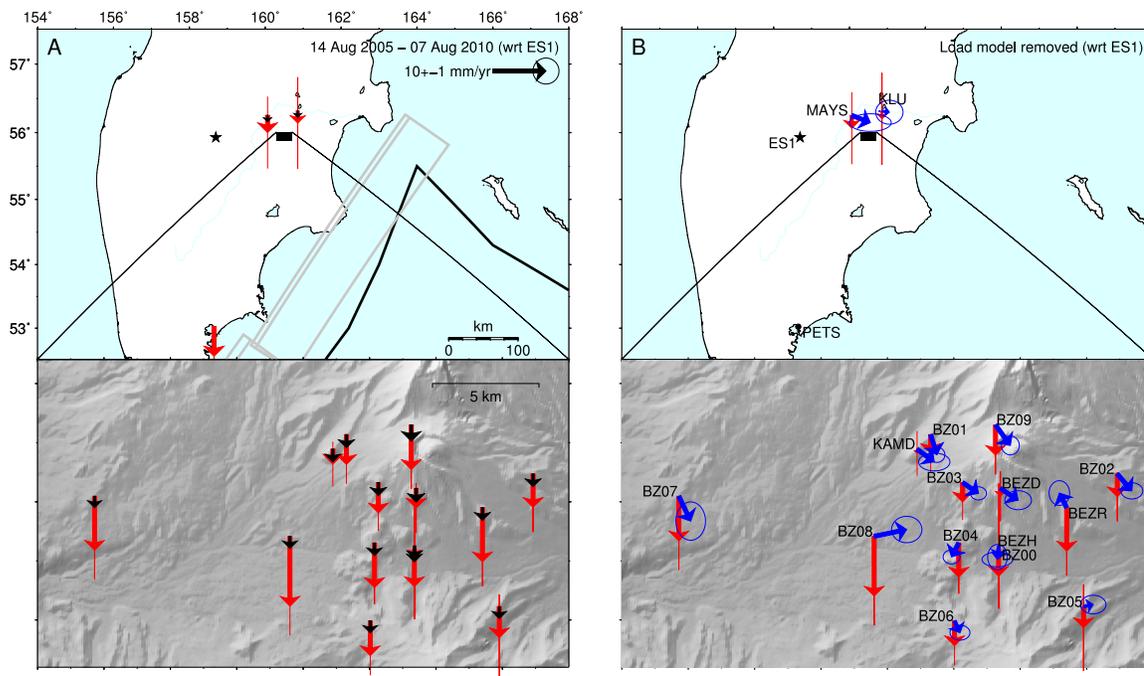
Figure 4.6: Load velocity model results. **(A)** Measured vertical velocities with tectonics model removed and relative to ES1 (star). Black vectors are prediction of vertical velocities due to load model as defined in Figure 4.5 (horizontals are negligible and not plotted for clarity, see Table 4.4). **(B)** Residual velocities after removal of load predictions (blue: horizontal, red: vertical).
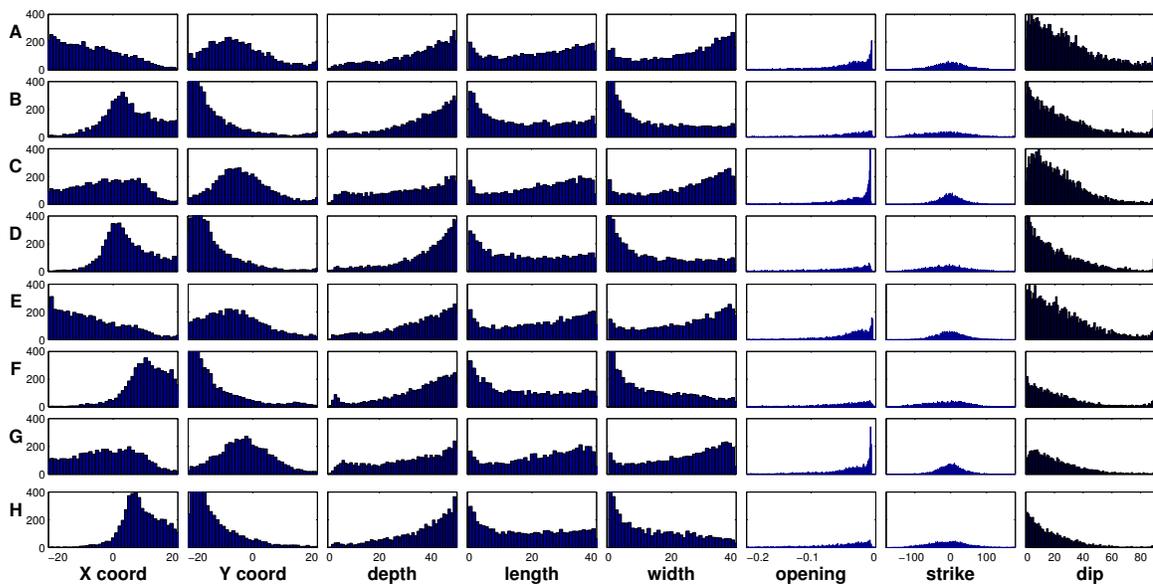
Figure 4.7: Histograms showing the distribution of best fitting parameters from 5000 simulated annealing experiments each using different input data. **(A)** South Bezymianny stations and vertical displacements used for fitting, load correction applied. **(B)** South Bezymianny stations and 3-D displacements used for fitting, load correction applied. **(C)** South Bezymianny stations and vertical displacements used for fitting, no load correction applied. **(D)** South Bezymianny stations and 3-D displacements used for fitting, no load correction applied. **(E)** All stations and vertical displacements used for fitting, load correction. **(F)** All stations and 3-D displacements used for fitting, load correction. **(G)** All stations and vertical displacements used for fitting, no load correction. **(H)** All stations and vertical displacements used for fitting, load correction applied.
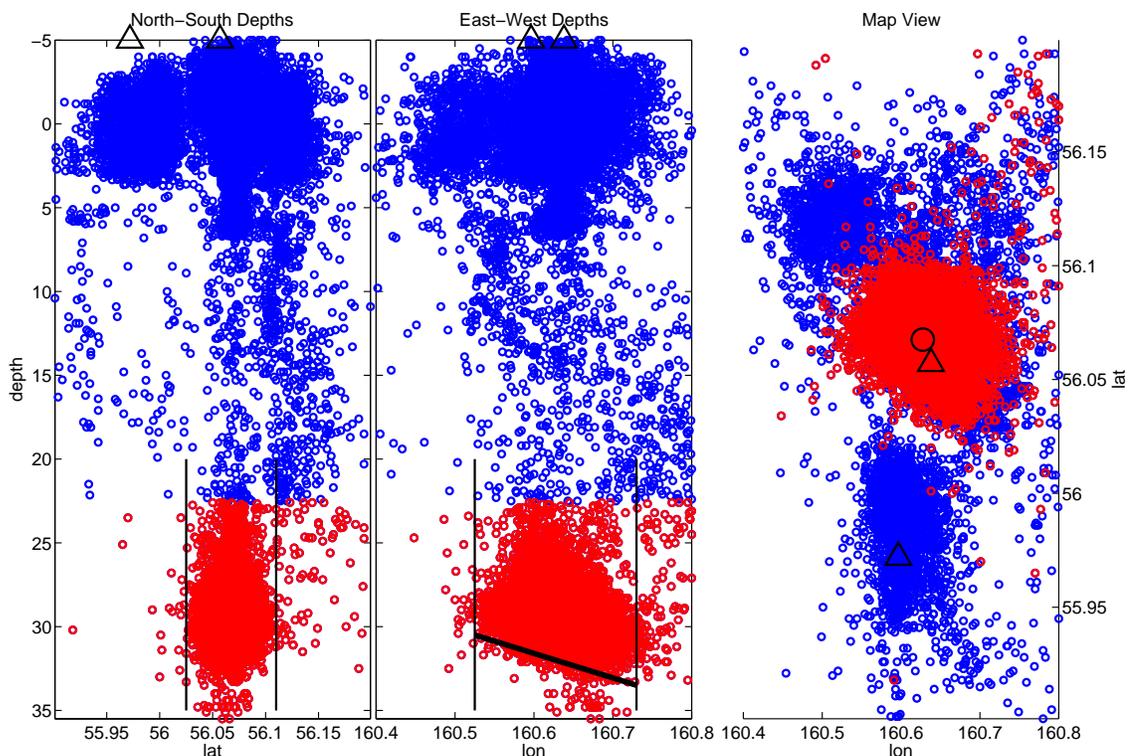
Figure 4.8: Seismicity under the KGV (KBGS catalog, 1999-2010). **Left** North-South section through the group and projection of earthquakes to a depth of 35 km onto one plane; earthquakes below 22 km are marked red. Triangles mark locations of Bezymianny (left) and Kluchevskoy (right). Several clusters of seismicity emerge. Black vertical lines mark the limits of the width of the sill we use in the forward model. **Middle** East-West section. Bezymianny is right triangle, Kluchevskoy is the left one. Black vertical lines mark the limits of the length of the sill we use in the forward model. The tilted gray line emphasizes an apparent dip in the bottom limit of seismicity. The dip of this line is about $13°$, which is used in our sill model. The deep end of this line is at 33.5 km, which constrains the depth of our sill. **Right** Map view of the seismicity. Triangles mark Kluchevskoy (north) and Bezymianny (south). Seismicity below 22.5 km is again colored red and clearly clusters under Kluchevskoy. The center point of the model sill is marked by the circle.
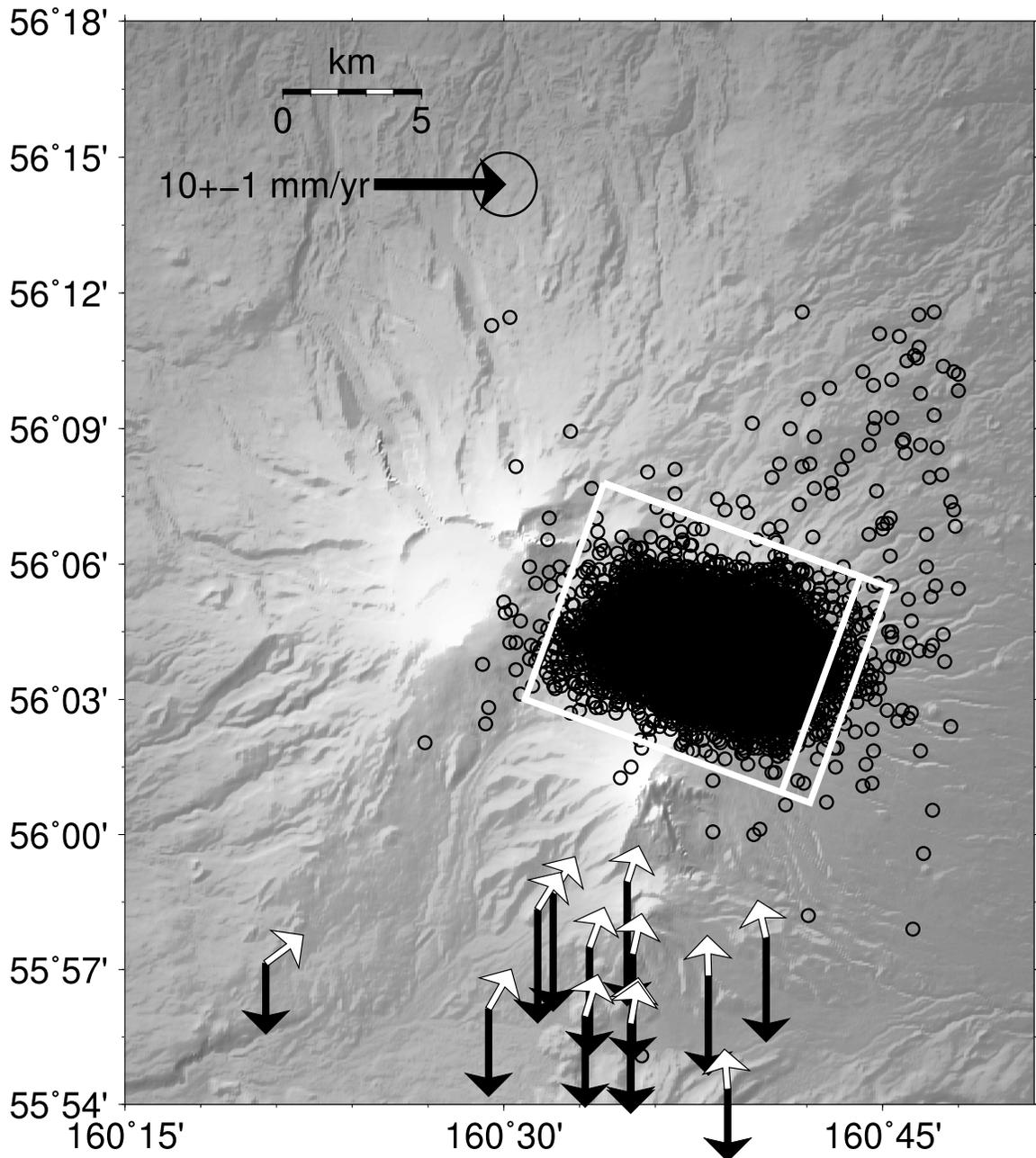
Figure 4.9: Sill model (white rectangle, double line indicates down dip end) inferred from seismicity below 22.5 km (black circles). Velocity predictions relative to ES1 for this model assuming a closing rate 0.22 m/yr for the sill are shown as white (horizontal) and black (vertical) vectors.
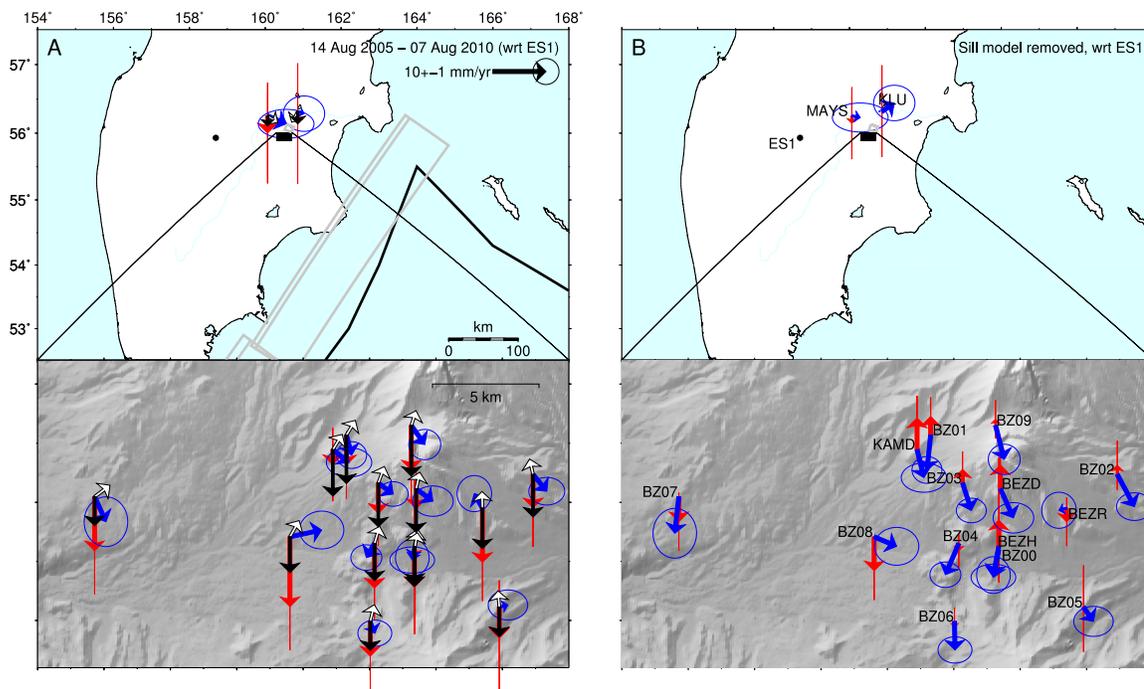
Figure 4.10: Site velocities and sill model predictions. **(A)** Velocities (blue: horizontal, red: vertical) with respect to ES1 (tectonics model removed, load model not removed) and predictions for a deflating sill under Kluchevskoy Volcano (white: horizontal, black: vertical). **(B)** Residuals after subtracting the model predictions from the data. The residual horizontal motion may be due to a mid-crustal volcanic source at Kluchevskoy or residual tectonic motion.
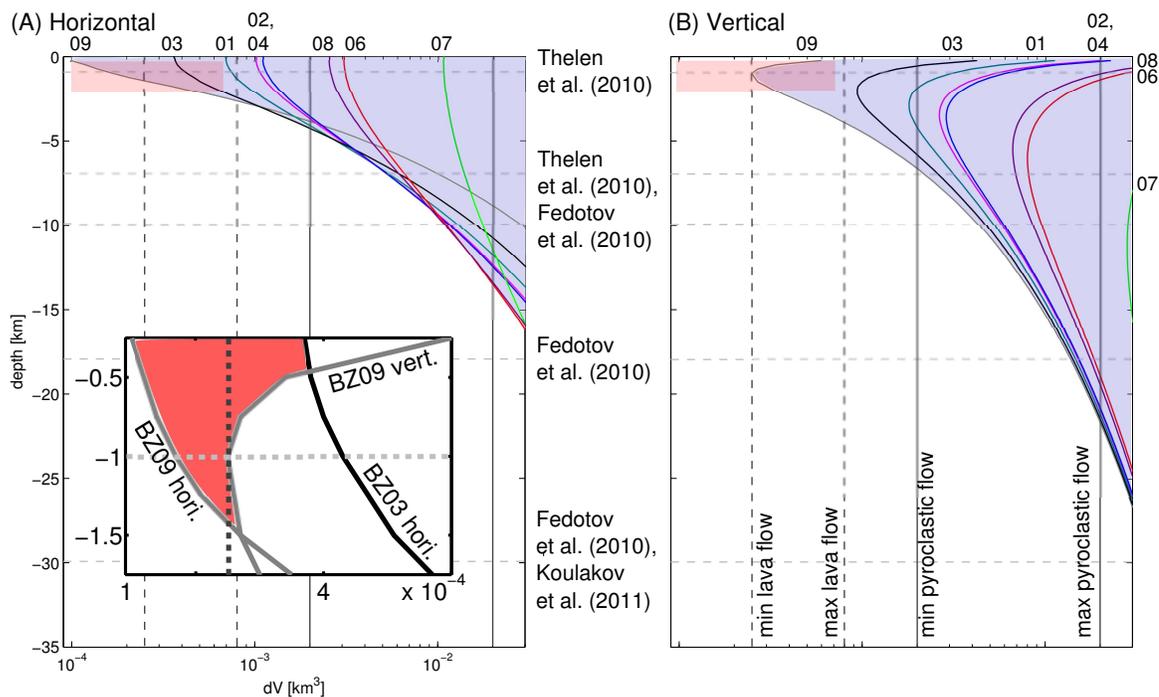
Figure 4.11: Network sensitivity assuming a Mogi source underneath Bezymianny's dome summit at 55.9719°N, 160.5965°E. Contours indicate volume change – depth combinations that would induce at least 1 cm of motion in horizontal (A) and vertical (B) at continuous GPS stations around Bezymianny. As station names only the two digit code is given, the leading "BZ" is left out for clarity. Note that volume change on horizontal axis is given on logarithmic scale. The horizontal gray dashed lines indicate depths of suggested sources; respective references are listed in between the panels. The vertical black dashed lines indicate a range of lava flow volumes extruded during eruptions (lava flows from 1984-2007 (Zharinov and Demyanchuk, 2011) $2.5 - 8.0 \times 10^{-4}$ km^3). The solid lines bracket a range of pyroclastic flow deposit volumes ($0.2 - 2.0 \times 10^{-2}$ km^3 (Girina, 2012, this volume)). **(A) Inset** Combination of vertical and horizontal contours for the region highlighted in pink in panels (A) and (B). The area highlighted in red shows the combinations of depth and volume change that would induce 1 cm or more motion in the horizontal at BZ09, but motion at or below the detection limit in the vertical at BZ09 and the horizontal at BZ03. A pressure point source at 0.25-1.5 km with a volume change of $1-4 \times 10^{-4}$ km^3 may be involved in the eruptions which falls in the region of a shallow source within the edifice as proposed by Thelen et al. (2010).
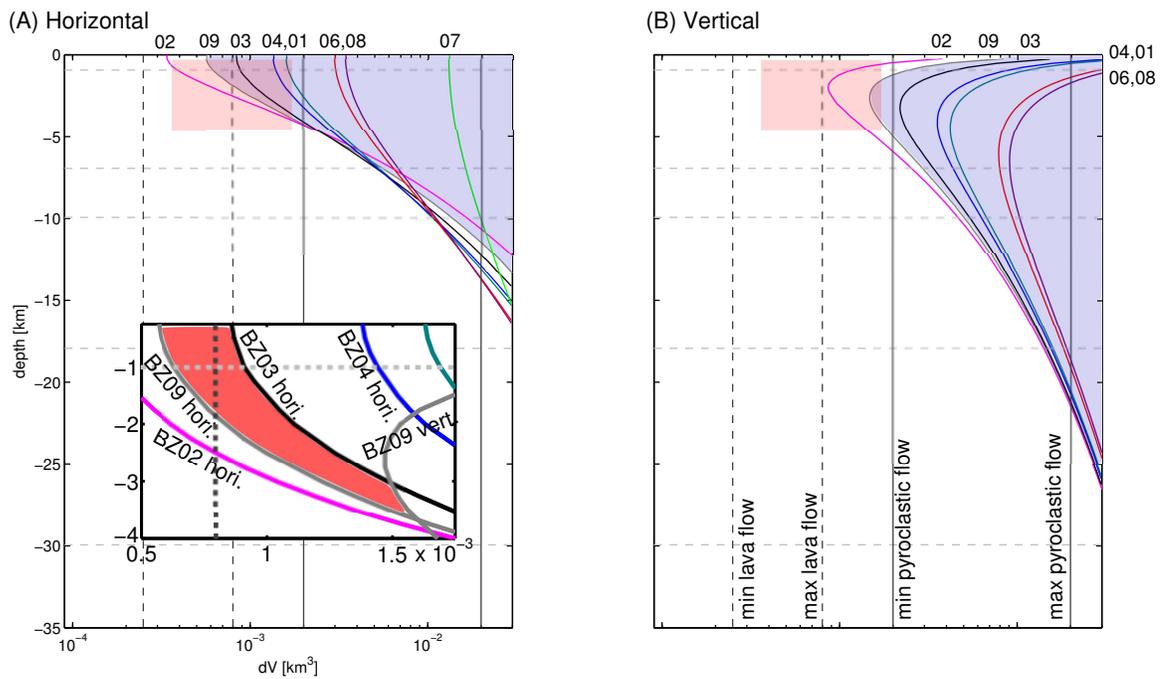
Figure 4.12: Similar to Figure 4.11, but for a source suggested by West (2012, this volume) in the blast zone about 2 km SE of the dome. Note that BZ02 was not operational during the two times (Dec. 16, 2009 and May 31, 2010) this source is assumed to have been active.
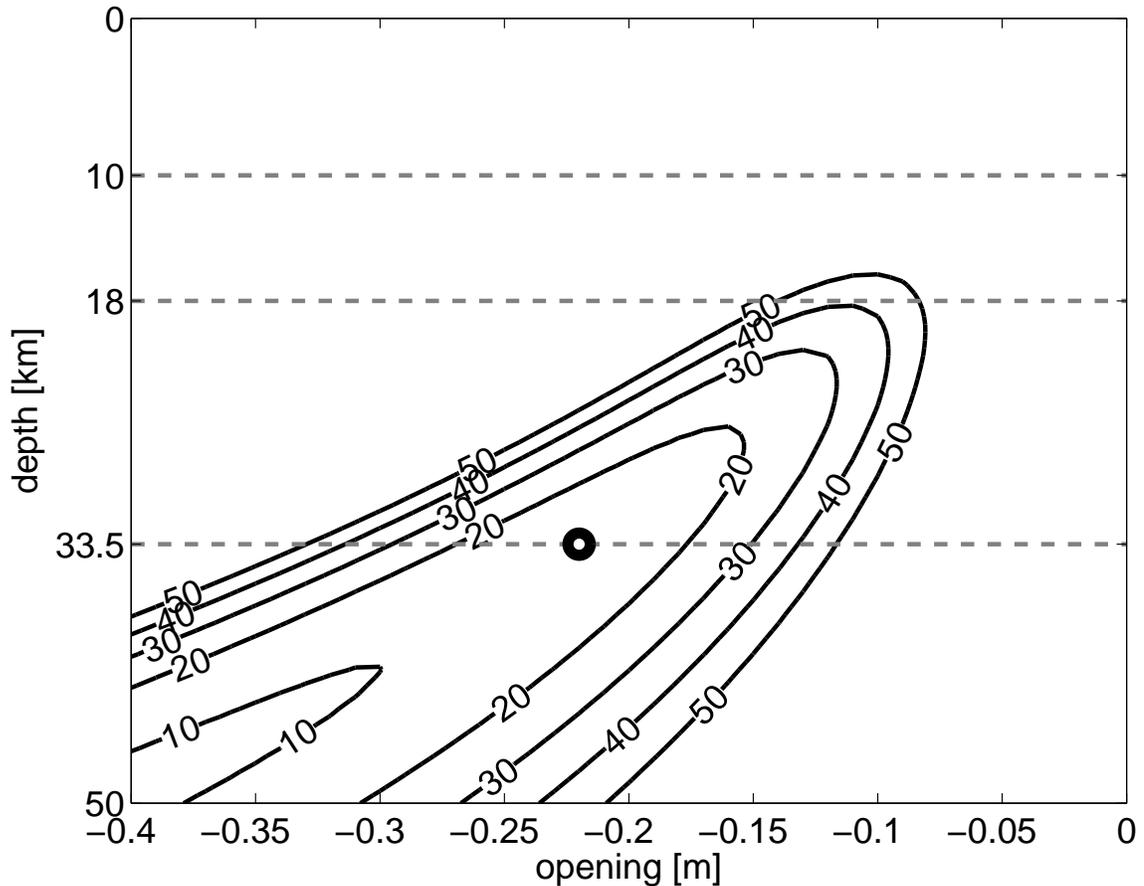
Figure 4.13: Sill depth–opening–trade-off in χ^2 misfit space. Bold circle marks the best opening derived for the sill we constrained from seismicity at 33.5 km depth. Other likely source locations are marked with dotted lines. If the width and length are kept fixed and we change just the opening, the shallower locations are unlikely sources for the deflation source. Note that the selected source does not provide the best fit to the data, which would be below 50 km; probably to accommodate the larger signal observed at BZ07. Stations used: BZ00, BZ01, BZ02, BZ04, BZ05, BZ06, BZ07, BEZR, MAYS, KLU.

Table 4.1: GPS benchmark coordinates and distance to Bezymianny dome (km). Installation dates (YYYY-MM-DD) represent the earliest available data.

4 Char ID	Lat (deg.)	Lon (deg.)	Height (m)	Installation Date	Dist to Dome (km)
Continuous sites					
BZ01	55.978379766	160.532566173	1998.7248	2006-10-06	4.0
BZ02	55.961769862	160.673119636	1615.8073	2006-10-07	4.9
BZ03	55.958141956	160.556598524	2071.6602	2006-10-06	2.9
BZ04	55.932567396	160.553716182	1671.3209	2006-10-07	5.2
BZ06	55.899598371	160.550529969	1715.9349	2006-10-06	8.6
BZ07	55.952326878	160.342916616	1497.2751	2007-12-02	16.0
BZ08	55.935400821	160.490028596	1472.6256	2007-12-02	7.8
BZ09	55.982467292	160.581416553	2539.8216	2006-10-06	1.5
Campaign sites					
BZ00	55.929872528	160.583754368	1445.8390	2007-07-21	4.8
BZ05	55.905622204	160.647691459	1552.9871	2007-07-21	8.1
BEZD	55.955679465	160.585075053	2126.5224	2005-08-22	2.0
BEZH	55.931323342	160.583882621	1453.8664	2005-08-21	4.6
BEZR	55.947547441	160.635012429	1638.5601	2005-08-22	3.6
KAMD	55.972258678	160.522331589	2016.3626	2005-08-21	4.6
KAMNET sites					
ES1	55.930500238	158.696605889	518.4864	1996-08-18	119
KLU	56.318416679	160.856016453	66.9442	1996-07-27	41.8
KLUC	56.318435566	160.856032316	66.8695	2008-08-27	41.8
MAYS	56.254257608	160.061819412	57.7978	2007-07-21	45.6
PETS	53.023299659	158.650134443	102.0694	1998-11-07	~360

Table 4.2: Velocities (mm/yr)

4 Char ID	wrt EURA (Figure 4.4A)			tectonics, ES1 removed[a] (Figure 4.4B)			load wrt ES1 removed[b]		
	N	E	U	N	E	U	N	E	U
Continuous sites									
BZ01	1.2±0.4	-10.4±0.3	-7.4±0.9	-3.7±0.6	1.0±0.6	-5.6±1.5	-3.8±0.6	1.2±0.6	-3.5±1.5
BZ02	2.0±0.4	-9.1±0.6	-8.1±1.3	-3.2±0.6	2.6±0.8	-6.3±1.9	-3.2±0.6	2.7±0.8	-4.3±1.9
BZ03	3.0±0.3	-8.7±0.3	-7.5±0.8	-2.1±0.5	2.8±0.6	-5.7±1.4	-2.0±0.5	3.0±0.6	-3.6±1.4
BZ04	2.4±0.3	-13.1±0.4	-10.2±0.7	-2.6±0.5	-1.5±0.7	-8.4±1.3	-2.6±0.5	-1.4±0.7	-6.4±1.3
BZ06	2.9±0.4	-10.8±0.5	-8.3±1.0	-2.2±0.6	0.9±0.8	-6.5±1.5	-2.2±0.6	1.0±0.8	-4.7±1.5
BZ07	0.1±1.3	-9.1±0.9	-12.0±1.7	-4.7±1.5	2.1±1.1	-10.2±2.2	-4.7±1.5	2.2±1.1	-8.4±2.2
BZ08	6.3±0.8	-5.5±0.9	-15.0±1.7	1.3±1.0	6.0±1.2	-13.2±2.3	1.3±1.0	6.1±1.2	-11.3±2.3
BZ09	1.4±0.5	-8.9±0.4	-10.2±0.9	-3.6±0.7	2.5±0.7	-8.4±1.5	-3.8±0.7	2.8±0.7	-5.7±1.5
Campaign Sites									
BZ00	3.2±0.3	-12.1±0.9	-8.8±0.7	-1.9±0.6	-0.4±1.2	-7.0±1.2	-1.9±0.6	-0.2±1.2	-5.0±1.2
BZ05	5.7±0.5	-10.2±0.7	-7.6±2.8	0.4±0.7	1.6±1.0	-5.8±3.3	0.4±0.7	1.8±1.0	-4.0±3.3
BEZD	2.8±0.5	-8.4±0.8	-5.5±1.4	-2.3±0.7	3.2±1.0	-3.7±1.9	-2.2±0.7	3.3±1.0	-1.5±1.9
BEZH[c]	3.0±0.8	-12.1±0.5	-3.8±4.3	-2.1±1.0	-0.4±0.8	-2.0±4.8	-2.1±1.0	-0.2±0.8	-0.0±4.8
BEZR	7.9±0.7	-13.2±0.5	-12.0±1.3	2.7±1.0	-1.5±0.8	-10.2±1.9	2.7±1.0	-1.4±0.8	-8.2±1.9
KAMD	2.6±0.5	-8.3±0.9	-4.6±1.2	-2.4±0.7	3.1±1.2	-2.8±1.7	-2.4±0.7	3.2±1.2	-0.8±1.7
KAMNET Sites									
ES1	4.1±0.2	-9.8±0.3	-2.1±0.6	0	0	0	0	0	0
KLU	4.3±0.7	-9.6±0.8	-4.2±3.0	-0.4±0.9	1.2±1.1	-2.3±3.5	-0.2±0.9	1.4±1.1	-1.5±3.5
MAYS	2.7±0.5	-6.7±1.3	-5.3±2.2	-1.5±0.7	3.5±1.6	-3.2±2.8	-1.4±0.7	3.5±1.6	-2.4±2.8
PETS	12.0±0.3	-24.7±0.4	-5.2±0.6	6.9±0.5	-8.6±0.6	-5.5±1.1		n/a	

[a]ES1 predicted subduction velocities (mm/yr): E=-2.5, N=2.8, U=0.4
[b]ES1 predicted load velocities (mm/yr): E=0.1, N=0.0, U=-0.4 (see Table 4.4)
[c]BEZH shows strong variation in the vertical for measurements in 2005 and 2006 which results in a lowered long term subsidence. As BZ00 is very close, we ignore measurements at BEZH.

Table 4.3: Loads used to estimate velocities listed in Table 4.4.

Load	Longitude (deg)	Latitude (deg)	radius (km)	height / growth rate	source
Kluchevskoy edifice	160.63809	56.06029	7.0	0.16 m/yr	Fedotov et al. (2010), this study
Tolbachik 1975 North	160.28928	55.71398	2.0	95 m	Fedotov et al. (2010)
Tolbachik 1976 South	160.19025	55.59816	3.0	35 m	
Bezymianny 1956					
Edifice	160.59590	55.97188	1.0	-159.2 m	Belousov et al. (2007)
Ash deposits	160.84885	55.93330	12.6	0.39 m	
Debris flows	160.65804	55.92613	1.4	11.59 m	
	160.69253	55.94633	0.7	23.19 m	
	160.74278	55.92406	2.0	8.52 m	
	160.80196	55.92321	1.4	17.39 m	
	160.84834	55.92252	1.4	17.39 m	
	160.89472	55.92182	1.0	11.36 m	
	160.94700	55.91112	0.7	23.19 m	
Bezymianny pyroclastic flows, 2007 and younger					
2007	160.65770	55.95579	1.1	4.47 m	Zharinov and Demyanchuk (2011)
2007			1.3	7.16 m	
2008			0.5	3.82 m	Girina (2012)
2008			0.5	3.82 m	
2009			0.6	1.77 m	
2010			1.4	3.74 m	
Bezymianny dome growth					
1956-1967	160.59590	55.97188	0.75	13.52 m/yr	Zharinov and Demyanchuk (2011)
1967-1976				7.02 m/yr	
1983-1994				1.61 m/yr	
1994-2006 (-2010)				4.06 m/yr	

Table 4.4: Modeled site velocities induced by surface loads

4 Char ID	East (mm/yr)	North (mm/yr)	Up (mm/yr)
Continuous sites			
BZ01	-0.1	0.0	-2.4
BZ02	-0.0	0.0	-2.4
BZ03	-0.1	-0.0	-2.4
BZ04	-0.1	-0.0	-2.3
BZ06	-0.1	-0.0	-2.2
BZ07	0.0	-0.0	-2.1
BZ08	-0.0	-0.0	-2.3
BZ09	-0.1	0.2	-3.1
Campaign sites			
BZ00	-0.1	-0.0	-2.3
BZ05	-0.1	-0.0	-2.2
BEZD	-0.1	-0.1	-2.6
BEZH	-0.1	-0.0	-2.4
BEZR	-0.0	-0.0	-2.4
KAMD	-0.1	0.0	-2.4
KAMNET sites			
ES1	0.1	-0.0	-0.4
KLU	-0.1	-0.2	-1.2
MAYS	0.1	-0.2	-1.2

Chapter 5

Conclusions

Considering that GPS can resolve dynamic motion at the 30 s to 1 Hz intervals (Chapter 2) it comes as no surprise that volcano source evolution is resolvable on the scale of weeks (Chapter 3) down to minutes or even seconds (Appendix C).

Operation on the scale of weeks in Chapter 3 allows us to track the evolution of the source region feeding the 2009 Redoubt eruption. The precursory activity prior to March 23, 2009 is due to a point source intrusion of $0.0194\,{}^{0.0092}_{0.0340}$ km^3 in volume at $13.50\,{}^{10.17}_{17.33}$ km below sea level (bsl, superscripts and subscripts refer to upper and lower ends of confidence intervals at the 95% level). During the explosive phase from March 23 to April 04, 2009 about $0.05\,{}^{0.028}_{>0.1}$ km^3 of magma was evacuated from a prolate spheroid with its centroid at $9.17\,{}^{6.92}_{15.17}$ km bsl, a semimajor axis of $4.50\,{}^{1.25}_{>10.00}$ km length and a semiminor axis of $0.475\,{}^{0.3}_{>4.0}$ km. The effusive activity lasted into June 2009 and is inferred to come from the same source, decreasing in volume by $0.0167\,{}^{0.0106}_{0.0228}$ km^3.

Combining these observations with results from seismology and petrology suggests a mid-crustal two reservoir system with material sourced from >20 km flowing in at about 13.5 km depth and reheating residual material in the proposed spheroid. The mixture migrated to shallower depth (2-4.5 km bsl) and reheated material there. As this residual magma erupted, it was replaced by the material from the spheroidal reservoir at 7 to 11.5 km depth, which renders the shallow source undetectable for geodetic instruments.

Chapter 4, however, clearly shows that network design and the individual characteristics of a volcano's plumbing system affect the ability to detect such motion on subdaily and even weekly time scales, which stresses the importance of network scale considerations. While explosive activity induces dynamic deformation at Bezymianny volcano (e.g., West, 2012), the scale of deformation is well below the detection limit of GPS at the distances it is being recorded. Future work should focus on the integration of broadband seismology and GPS geodesy to extend the spectrum of resolvable deformation and learn about transient signals related to explosions and conduit processes without the need for additional instrument installations (e.g., tiltmeters).

Volcanic plume traces are one example of a non-deformation signal that may be missed when GPS data are reduced to a daily average (Chapter 3, Appendix B). Systematic spikes

in subdaily positioning solutions indicate phase delays for station–satellite–pairs that cross dense parts of volcanic plumes. While the technique of detecting ash plumes with GPS has been described before by Houlié et al. (2005a,b), this possibility is not generally included in monitoring or data analysis efforts and is, in fact, not well explored. Plotting the phase residuals along the sky tracks of satellites provides easy visual access to plume azimuths and provides a useful monitoring tool. Kinematic solutions in near real-time could be used for plume sensing and verification and hence assist remote sensing efforts to fill some of the gaps created by slow satellite repeat times or cloud cover. Future work is necessary to determine ash concentrations and plume heights that affect the GPS signal quality significantly and hence determine detection limits.

Another useful monitoring tool coming out of this research is the presentation of deformation evolution in map-view animations rather than stacks of time series for individual stations. This maintains both spatial and temporal correlation of the data and displays it in an intuitive way, which – for the example of the 2011 Tohoku Earthquake – allows for instantaneous estimates of rupture duration (smaller than 217 s) and ruptured fault length (smaller than 530 km). The latter estimate is important to identify areas prone to large aftershocks as shown by the two strongest near coast aftershocks recorded within 30 minutes of the main event (Figure 2.2E,F). Automation of this manual assessment is possible and combined with a self-organizing ad-hoc network approach as described by Fleming et al. (2009) a displacement-based alarm system could be implemented. This would be useful not just in earthquake applications but also for volcano monitoring or other deformation monitoring problems.

In addition to the conclusions above which answer the main questions posed in Chapter 1, long-wavelength, long-term subsidence of the Bezymianny network at rapid rates between 8 and 12 mm/yr suggests that the Kluchevskoy Group of Volcanoes is subsiding due to the deflation of a deep sill under Kluchevskoy Volcano. The very localized sampling of GPS velocities described in Chapter 4 supports a wide range of geometries for this model. Deep seismicity underneath Kluchevskoy poses additional constraints on location and geometry and suggests a sill of 9.5 km width, 12.7 km length, and a $13°$ dip-angle to the south-east. The sill closing rate of 0.22 m/yr inferred from the GPS velocities suggests a volume loss of 0.027 km^3/yr (0.16 m/yr and 0.019 km^3/yr respectively, considering sur-

face loading). Additional stations in the near and far field are required to uniquely resolve the spatial extent and likely partitioning of this source.

Network sensitivity analysis limits the possible sources underneath the summit of Bezymianny that induce slight deformation only at the summit station BZ09 to a shallow reservoir at about 0.25–1.5 km depth with a volume change of $1\text{-}4 \times 10^{-4}\,\text{km}^3$, which is similar in location to that suggested by Thelen et al. (2010). Much of the material erupted at Bezymianny may be sourced from deeper mid-crustal reservoirs with co-eruptive volume changes at or below the detection limit of the GPS network. Installation of more sensitive instruments such as tiltmeters would lower the detection limit of the network and hence allow resolving more subtle co-eruptive motion.

Bibliography

Fleming, K., Picozzi, M., Milkereit, C., Kühnlenz, F., Lichtblau, B., Fischer, J., Zulfikar, C., Özel, O., 2009. The Self-organizing Seismic Early Warning Information Network (SOSEWIN). Seismological Research Letters 80 (5), 755–771.

Houlié, N., Briole, P., Nercessian, A., Murakami, M., 2005a. Sounding the plume of the 18 August 2000 eruption of Miyakejima volcano (Japan) using GPS. Geophys. Res. Lett. 32, L05302.

Houlié, N., Briole, P., Nercessian, A., Murakami, M., 2005b. Volcanic Plume Above Mount St. Helens Detected with GPS. Eos Trans. AGU 86 (30), 277–281.

Thelen, W., West, M., Senyukov, S., 2010. Seismic characterization of the fall 2007 eruptive sequence at Bezymianny Volcano , Russia. Journal of Volcanology and Geothermal Research 194 (4), 201–213.

West, M. E., 2012. Recent eruptions at Bezymianny volcano – a seismic comparison. Journal of Volcanology and Geothermal Research, in review.

Appendix A

Curiosities in the 1 Hz GPS Data for the 2011 Tohoku-oki Earthquake, Japan

A.1 Introduction

Few of the more than 1200 continuous GPS stations in Japan are openly available. The open sites are part of the global satellite tracking network of the International GNSS Service (IGS). In response to the 2011 M_w 9.0 Tohoku-oki earthquake in Japan we processed 1 Hz data of some of these stations shown in Figure A.1. Later we gained access to processed 1 Hz time series of a subset of the stations for central Japan published by GPS Solutions[1]. We animated these high-rate time series in a similar way as the 30 s time series presented in Chapter 2 (Animation S4).

A.2 Results

An interesting result that is completely missing in the 30 s movies is the variable motion rate at the GPS sites. The sites begin to move but then stall for a few seconds until they eventually move at similar velocity towards their final position, which they overshoot dynamically and then move back. This process, while obvious in Animation S4, is much better illustrated in the particle plots for two sample IGS stations (Figure A.2). These plots clearly show a slow, accelerating onset of motion which comes to a halt at approximately 5:47:40 UTC (at MIZU, later at USU3). This is about 77 seconds into the earthquake. The motion continues only several seconds later (see also Figure A.3).

Comparing the displacement record at USU3 to the velocity record of the nearby openly available Global Seismic Network (GSN) seismic station MAJO (Figure A.3) indicates that displacement in USU3's north component and velocity changes at MAJO are registered at about the same start time. USU3, however, does not move towards the east significantly in the first 30 s or so (Figure A.2). The velocity record at MAJO clearly clips but there does not seem to be much agreement between the pause of displacement at USU3 and a similar phase of zero velocity at MAJO. Differentiating the displacements at USU3 to velocities (Figure A.4) does not shed more light on this picture; likely because the record at MAJO is incomplete in amplitude.

---

[1]http://rtgps.com/rtnet_dl_eq.php

A.3 Discussion

Vigny et al. (2011) observe similar behavior at GPS stations for the 2010 M_w 8.8 Maule Earthquake in Chile. While they find a good model that fits the static offsets due to the earthquake well, their attempts to reproduce the observed particle motion with assumed variation in rupture velocity or a double source forward model fail. To address this problem fully, we need to perform time-step wise inversions of slip to infer the dynamics of the rupture process as done by (Miyazaki et al., 2004) for the 2003 Tokachi-oki earthquake in Japan.

Yue and Lay (2011) present one possible solution based on low-pass filtered GPS data eliminating data with frequencies higher than $1/25$ Hz (i.e., only periods > 25 s remain after filtering). Their inversion of ground motion to characterize the rupture process utilizes records of a subset of the high-rate GPS stations. This yields a two step function in moment release, which reflects the two step function in motion at the sites (e.g., Figure A.2).

Yue and Lay (2011) use a simple 1-D velocity structure of the Earth and fit the low-pass filtered GPS data very well (including predictions at sites not used in the inversion). However, higher frequency characteristics of the particle trajectories (Figure A.2) depend on more complex crustal structures, which would require the derivation and application of more sophisticated Earth models when deriving the slip during the earthquake. For example, Animation S4 shows some station vectors spinning after the surface waves have passed. This is not an error in the solution, but likely due to reverberations of seismic waves in sediment basins as shown by Hung and Rau (2011) for Tawain's 1 Hz GPS network for surface waves after the 2011 Tohoku earthquake.

Bibliography

Hung, H.-K., Rau, R.-J., 2011. Precision of surface wave displacement seismograms from the 2011 MW 9.0 Tohoku, Japan earthquake recorded by a dense high-rate GPS network in Taiwan, Abstract G51A-0864 presented at 2011 Fall Meeting, AGU, San Francisco, Calif., 5-9 Dec.

Miyazaki, S., Larson, K. M., Choi, K., Hikima, K., Koketsu, K., Bodin, P., Haase, J., Emore, G., Yamagiwa, A., 2004. Modeling the rupture process of the 2003 September 25 Tokachi-Oki (Hokkaido) earthquake using 1-Hz GPS data. Geophys. Res. Lett. 31, L21603.

Vigny, C., Soquet, A., Peyrat, S., Ruegg, J.-C., Metois, M., Madariaga, R., Morvan, S., Lancieri, M., Lacassin, R., Campos, J., Carrizo, D., Bejar-Pizarro, M., Barrientos, S., Armijo, R., Aranda, C., Valderas-Bermejo, M.-C., Ortega, I., Bondoux, F., Baize, S., Lyon-Caen, H., Pavez, A., Vilotte, J. P., Bevis, M., Brooks, B., Smalley, R., Parra, H., Baez, J.-C., Blanco, M., Cimbaro, S., Kendrick, E., 2011. The 2010 Mw 8.8 Maule Megathrust Earthquake of Central Chile, Monitored by GPS. Science 332, 1417–1421.

Yue, H., Lay, T., 2011. Inversion of high-rate (1 sps) GPS data for rupture process of the 11 March 2011 Tohoku earthquake (Mw 9.1). Geophys. Res. Lett. 38 (March), L00G09.
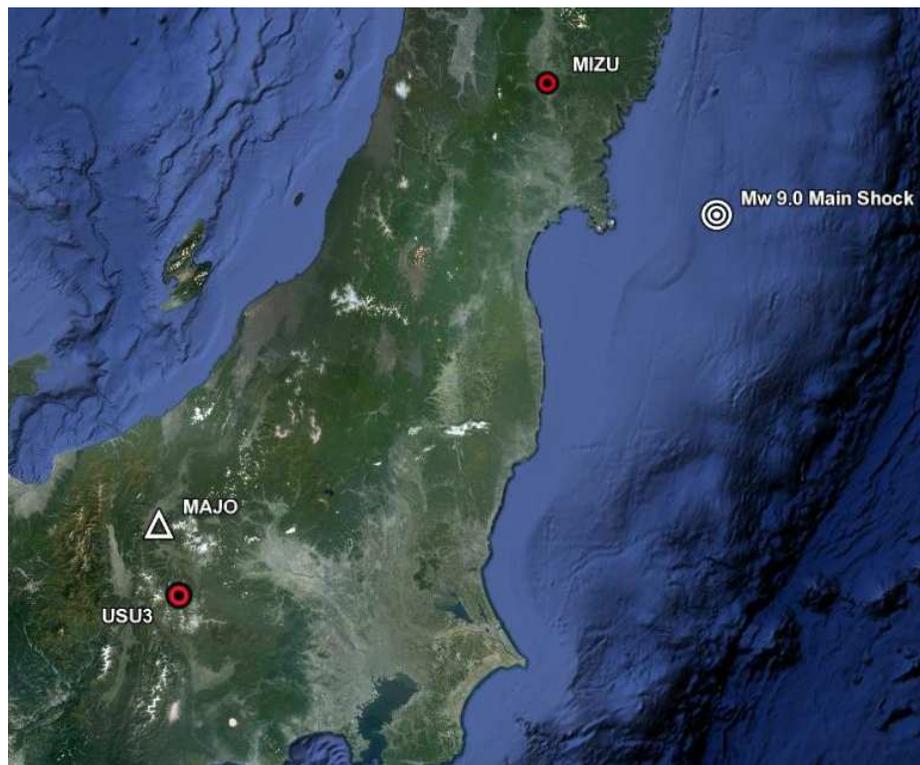
Figure A.1: Locations of IGS GPS stations USU3 and MIZU and GSN seismic site MAJO.
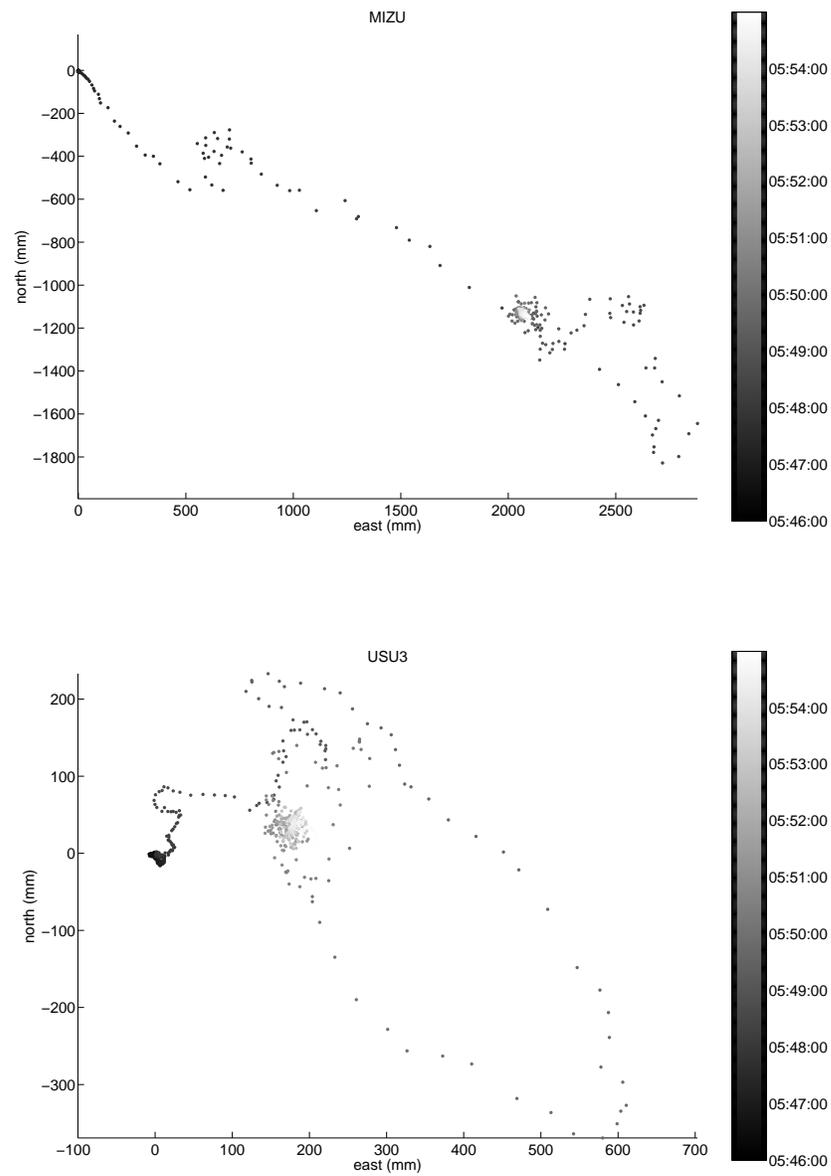
Figure A.2: Particle plots for MIZU and USU3. Color bar indicates UTC time.
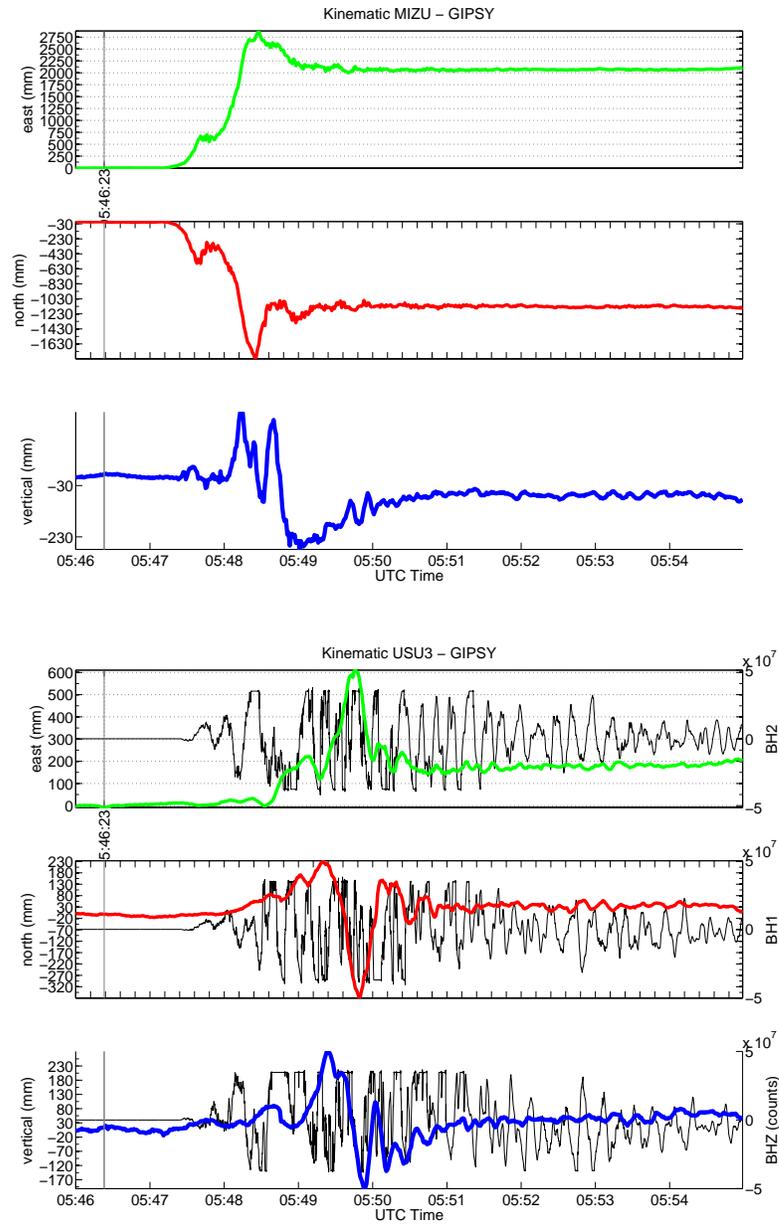
Figure A.3: **Upper panel** MIZU displacement time series in east (green), north (red) and up (blue) components. Vertical bar at 5:46:23 denotes time of main shock. **Lower panel** USU3 displacements and MAJO velocities in background (black).
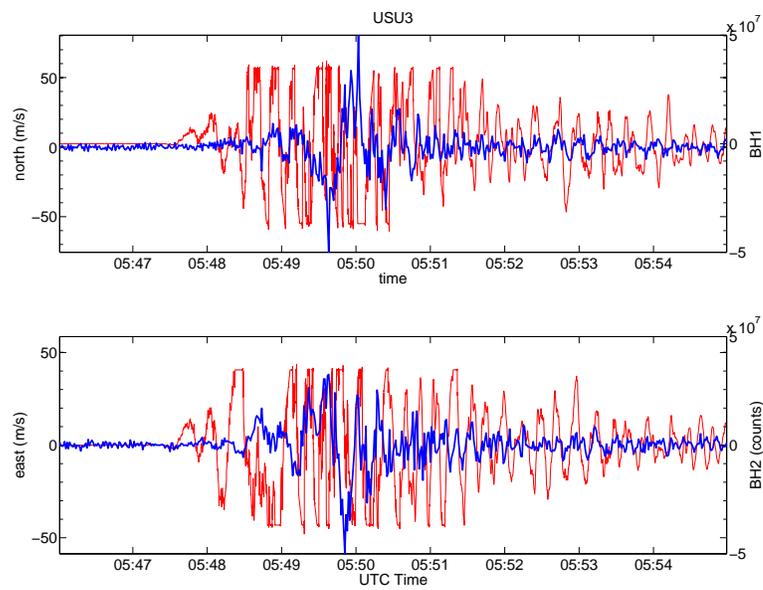
Figure A.4: USU3 velocities (blue) and MAJO velocities (red) in east and north components.

Appendix B

GPS and Volcanic Ash Plumes: The eruption of Okmok 2008, Alaska

B.1 Introduction

It is known that the injection of volcanic ash in the atmosphere induces phase delays not modeled by GPS analysis tools, which results in apparent displacements in GPS time series (Houlié et al., 2005a,b; Grapenthin et al., 2012). However, little work has been done on turning this problem into an effective volcano monitoring tool. Satellite based remote sensing techniques provide good spatial coverage for the detection of volcanic plumes, but slow satellite repeat times (>30 minutes) and cloud cover can prevent the detection entirely. GPS, in turn, provides excellent temporal coverage, but requires favorable satellite–station–geometry such that the signal propagates through the plume if it is to be used for plume detection.

The eruption of Okmok Volcano in 2008 (Larsen et al., 2009) produced significant ash plumes reaching over 15 km of altitude. This eruption was recorded by a sparse continuous GPS network (Figure B.1) recording at 10 second intervals, but telemetry failures caused many data dropouts. During the eruption only the sites OKFG and OKSO were operational. We analyze these records to investigate the use of GPS phase residuals for plume monitoring, sensing and tracking. Grapenthin et al. (2012) already present the straightforward derivation of plume azimuths from phase residuals plotted along the sky tracks of individual satellites. However, the phase residuals are not necessarily linearly related to the phase delay as some of it is mapped into station coordinates and likely other parameters in the least squares solution. The derivation of plume densities hence not only depends on how a plume effectively slows a signal at speed of light, but also how this error is mapped into the various parameters to be estimated when solving for a station position. To explore how a plume affects the GPS signal, we study station OKFG, which experiences little permanent displacement during the 2008 Okmok eruption (Freymueller and Kaufman, 2010) and fix GPS solution parameters to reasonable a-priori values.

B.2 Data and Processing

We use `teqc` (Estey and Meertens, 1999) in full quality check mode to extract observables for multipath (e.g., Larson et al., 2007) for L1 and L2 (MP1, MP2), signal to noise ratios

for L1 and L2 (SN1, SN2), ionospheric delay (ION), and its derivative (IOD) logged by the receiver (after conversion from receiver specific data format to the Receiver Independent Exchange format (RINEX, Gurtner and Estey (2007)). These files of GPS observables are plotted in skyplots as described in Section 3.2.3. In addition to this, we also try to extract signal-to-noise ratios using `RinexSNR`, a code provided by K. Larson, Univ. Colorado in Boulder. This code crashed on some RINEX files, however. These attempts to extract plume signatures from signal-to-noise ratios or multipath observables recorded directly by the receiver did not yield meaningful results.

Figure B.2 shows a time series produced from a standard kinematic solution (compare to Grapenthin et al., 2012). We mark the onset of the eruption, and the time the plume moves toward the North (Larsen et al., 2009). As the plume spreads (Larsen et al., 2009, their Figure 1C) and new explosions begin we see the position of OKFG drift. Grapenthin et al. (2012) explain this by increased signal travel time from the satellites to the receivers due to the ash plume.

We apply the method described by Grapenthin et al. (2012) to get satellite-by-satellite phase residuals for station OKFG (Figure B.3). To avoid mapping any of the phase delay into position or atmospheric estimates, we assume constant (dry) atmosphere and hold the station position fixed. The latter is reasonable considering that Freymueller and Kaufman (2010) give -96 ± 3 mm east, 5 ± 3 mm north, and -31 ± 4 mm vertical permanent displacement for the entire eruption. Dynamic motion due to individual explosions can be considered small (e.g., West, 2012; Grapenthin et al., 2012; Hreinsdóttir et al., 2012). The difference between the method described by Grapenthin et al. (2012) and our improvements is shown in Figures B.3 and B.4.

Unfortunately, the telemetry for OKFG data was very unreliable so we do not have a full record of data for this station during the eruption.

B.3 Discussion and Conclusions

Figures B.3 and B.4 show the difference the processing makes, which yields a significant increase in phase residuals during the later part of July 12, 2008 when the plume obscures the WNW skyview at OKFG (compare to Larsen et al. (2009, their Figure 1C)). While Figure B.3 shows some elevated phase residuals in the WNW sky toward the vent, it appar-

ently moves at the same time by more than 200 mm in the horizontal component. This exceeds the total permanent displacement at this site by a factor of 2 and is simply due to a delay of the signal when penetrating the volcanic plume.

Assuming a fixed position and dry atmosphere for OKFG results in much larger phase residuals (e.g., PRN 24, 26, 15 in Figure B.4 or Animation S5). Because the unmodeled change in atmospheric conditions (i.e., signal travel path) cannot be mapped into the position estimate, the misfit increases and becomes an actual measure of plume strength for this GPS site at this volcano.

Much of the data before July 12 has many extended gaps due to telemetry issues. To ensure the signal seen in Figure B.4 (especially PRN 24, which is low in the sky) is not due to multipath, we had to go back to July 02 to find a day with no data dropouts for comparison. Figure B.5 shows an overlay of the July 02 phase residuals (gray) on the July 12 phase residuals. Clearly the earlier solution is less noisier and the effect of the plume can be seen at many satellites, usually beginning slightly before 22:00 UTC.

Animation S5 shows the development of the phase residuals at OKFG over the course of July 12, 2008. We show an hour of data at a time and advance this window in 5 minute steps until 20:00 UTC, when we increment in 1 minute steps.

We processed data for the days after the onset of the eruption until July 20, 2008 and found similar data problems as prior to the eruption. Due to this sparseness of data from OKFG an in-depth study of the effect of eruption plumes on GPS is not possible using this station. Future work will analyze data from OKSO.

For near real-time applications we cannot assume that a station is stationary (see Figure C.1); at least not for an entire eruption. An iterative approach in which the actual station position is updated in pre-defined intervals and this processing takes the inferred atmospheric changes due to the plume into account would be easy to implement. The updated station position will then be the basis for plume monitoring until the next position change is to be estimated.

Bibliography

Estey, L. H., Meertens, C. M., 1999. TEQC: The Multi-Purpose Toolkit for GPS / GLONASS Data. GPS Solutions 3 (1), 42–49.

Freymueller, J. T., Kaufman, A. M., 2010. Changes in the magma system during the 2008 eruption of Okmok volcano, Alaska, based on GPS measurements. Journal of Geophysical Research 115, B12415.

Grapenthin, R., Freymueller, J. T., Kaufman, A. M., 2012. Geodetic observations during the 2009 eruption of Redoubt Volcano, Alaska. Journal of Volcanology and Geothermal Research, Special Issue on the 2009 Redoubt Eruption, in press.

Gurtner, W., Estey, L., 2007. RINEX The Receiver Independent Exchange Format Version 3.00.

Houlié, N., Briole, P., Nercessian, A., Murakami, M., 2005a. Sounding the plume of the 18 August 2000 eruption of Miyakejima volcano (Japan) using GPS. Geophys. Res. Lett. 32, L05302.

Houlié, N., Briole, P., Nercessian, A., Murakami, M., 2005b. Volcanic Plume Above Mount St. Helens Detected with GPS. Eos Trans. AGU 86 (30), 277–281.

Hreinsdóttir, S., Sigmundsson, F., Roberts, M., Bjornsson, H., Grapenthin, R., Arason, T., Arnadóttir, T., Hólmjarn, J., Geirsson, H., Bennett, R., Oddsson, B., Gudmundsson, M. T., Ofeigsson, B. G., Villemin, T., Sturkell, E., 2012. A High Rate Geodetic Magma Chamber Meter and the Evolution of the Grímsvötn 2011 Eruption, in prep.

Larsen, J., Neal, C., Webley, P., Freymueller, J. T., Haney, M., McNutt, S., Schneider, D., Prejean, S., Schaefer, J., Wessels, R., 2009. Eruption of Alaska Volcano Breaks Historic Pattern. Eos Trans. AGU 90 (20), 173–174.

Larson, K. M., Bilich, A., Axelrad, P., 2007. Improving the precision of high-rate GPS. J. Geophys. Res. 112, B05422.

West, M. E., 2012. Recent eruptions at Bezymianny volcano – a seismic comparison. Journal of Volcanology and Geothermal Research, in review.
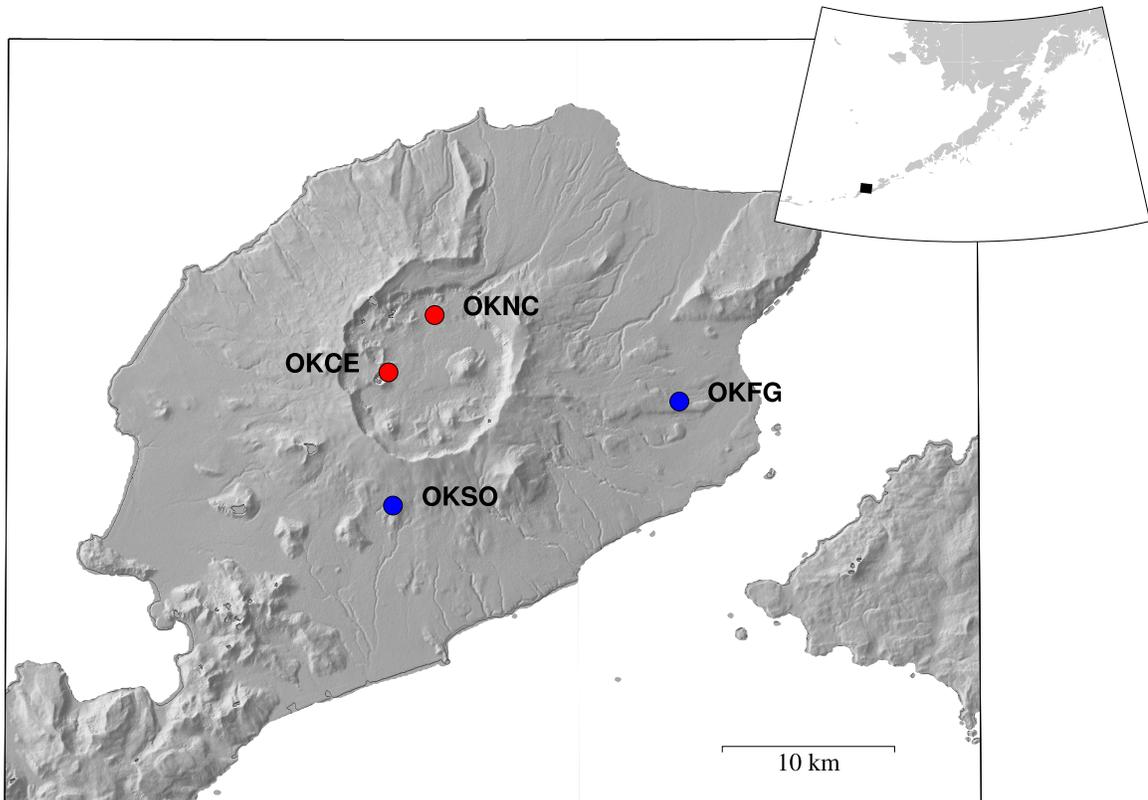
Figure B.1: Map of Okmok Volcano with continuous GPS stations. Blue dots: operational stations during the 2008 event. Red dots: OKNC was installed in 2010, and OKCE was not operational at the time of the eruption. Black square in inset indicates location of detail map.
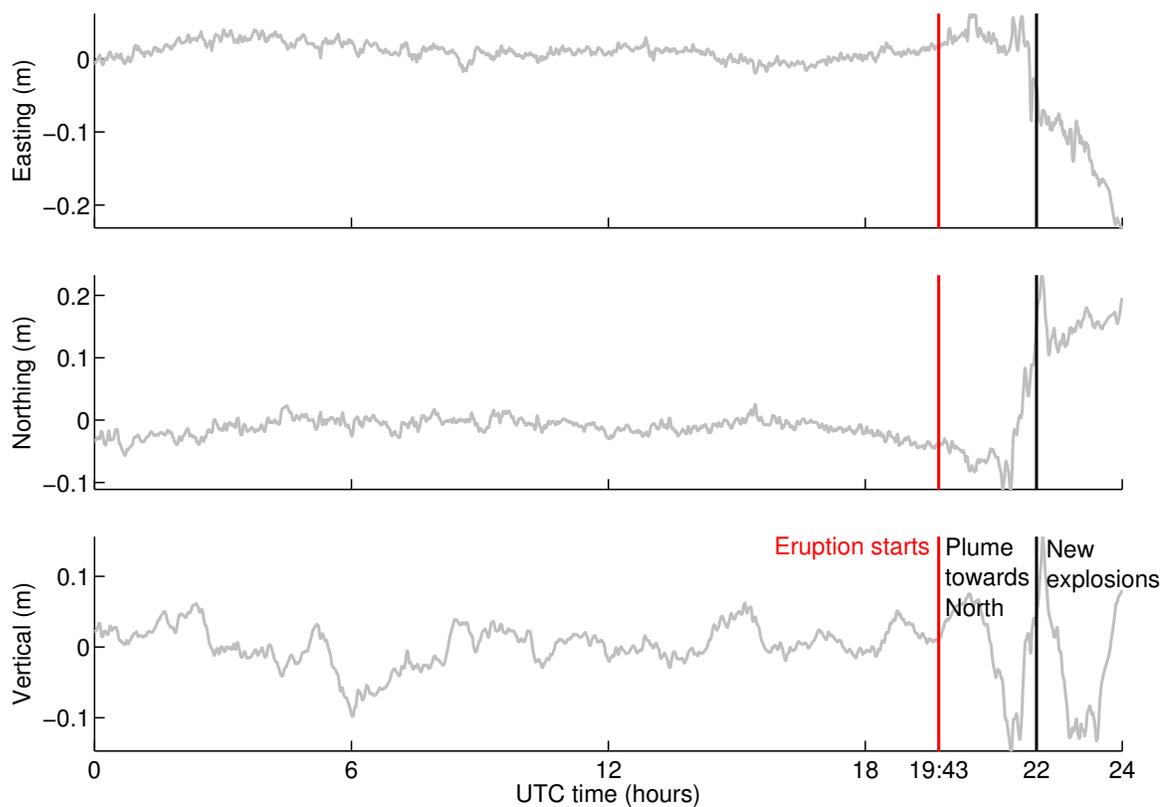
Figure B.2: Kinematic solution for OKFG (gray). Permanent displacements during entire eruption (Freymueller and Kaufman, 2010): -96 ± 3 mm East, 5 ± 3 mm North, -31 ± 4 mm Up are smaller than offsets shown in this time series. Red line marks time of first explosion with ash-rich plume (Larsen et al., 2009, their Figure 1C) drifting to North. Black line at 22:00 UTC shows time when water rich plume shows in GOES data. Significant position offsets show plume effects sooner than that, but not at onset of eruption as satellite signals do not penetrate the plume due to unfavorable satellite–station–geometry. A station located North of the vent would have improved the detection.
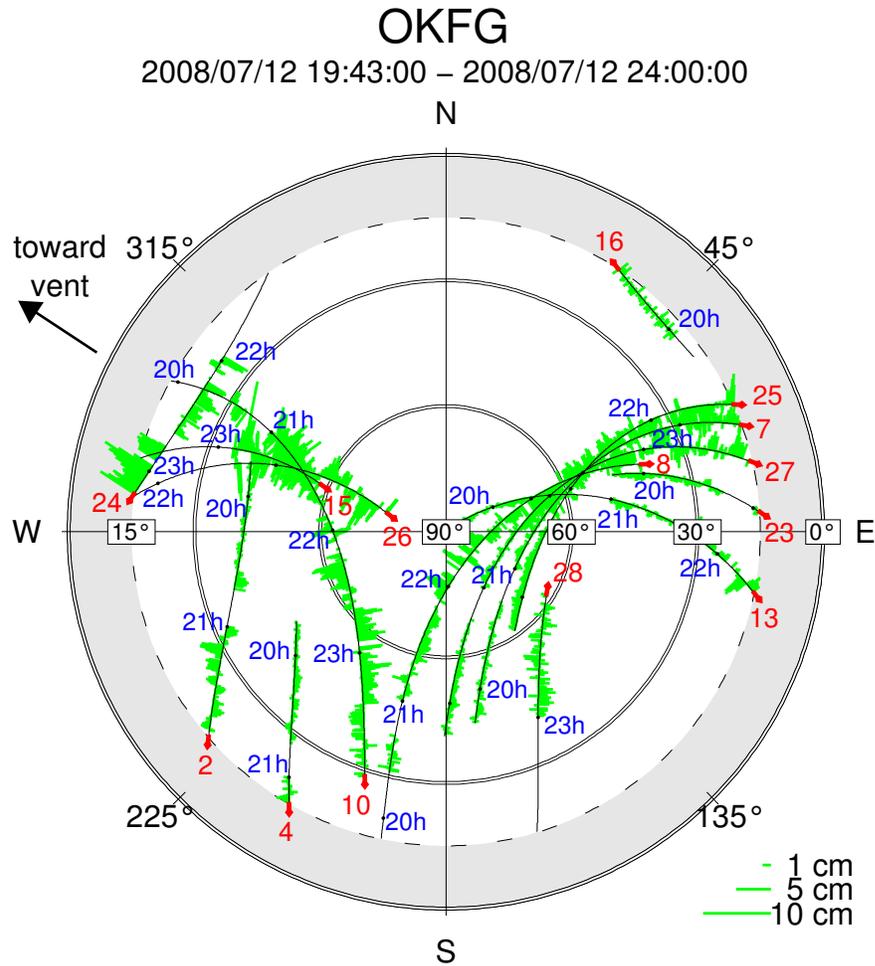
Figure B.3: Phase residuals from standard kinematic solution for OKFG (E of vent). Phase residuals (green) are plotted along satellite sky tracks. Satellite PRN is shown in red. Full UTC hours in blue are next to black dots. We show the time from onset of first explosion (19:43) to midnight on July 12, 2008. Data gaps due to loss of telemetry link. Distinct peaks of phase residuals in the WNW do not show up until after 22:00 UTC. Compare to Larsen et al. (2009, their Figure 1C): The initial plume drifts to North where we have no satellite coverage.
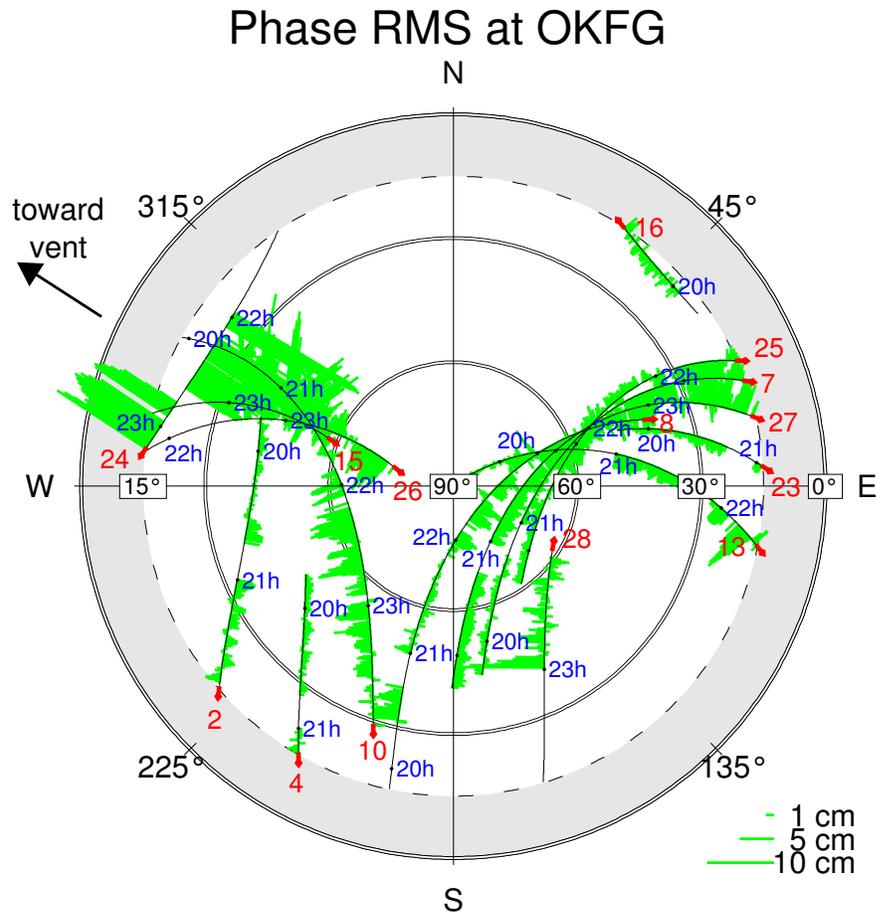
Figure B.4: Phase residuals for fixed OKFG (compare to Figure B.3). Noisy signal to WNW much more amplified as no phase delay can be mapped in the station position.
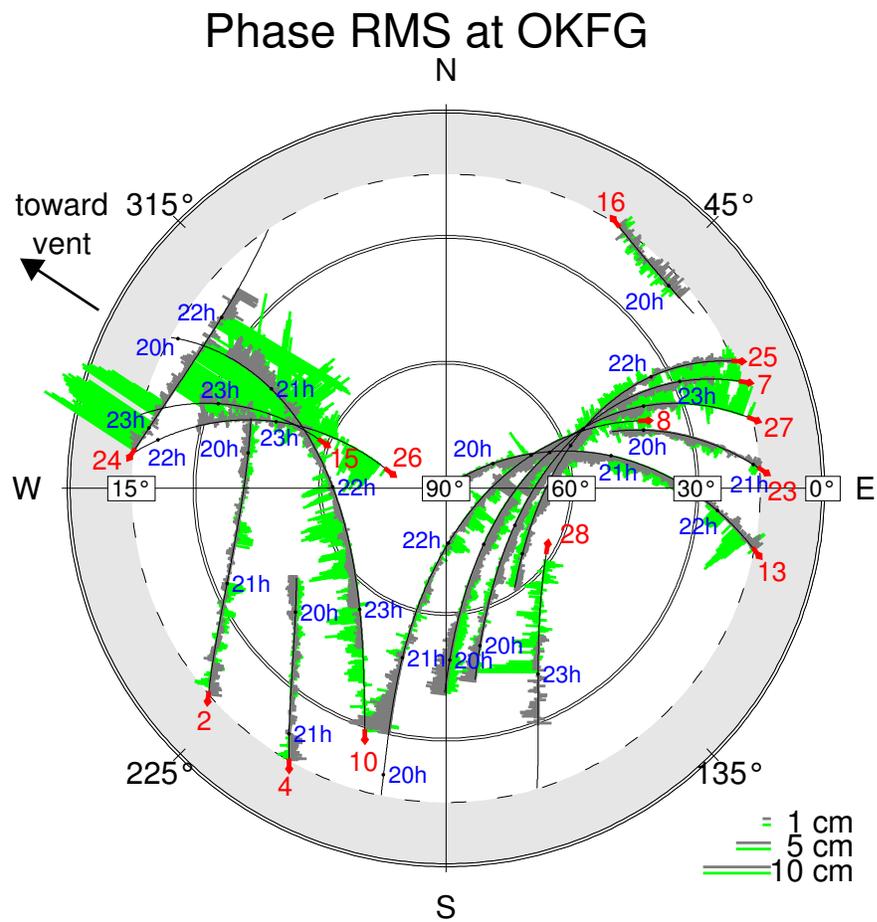
Figure B.5: Phase residuals for fixed OKFG on July 07, 2008 from 19:43 UTC until the end of day (green) and July 02, 2008 from 20:23 UTC until the end of day (gray). The July 02 data clearly shows that the phase residuals are much lower on a pre-eruptive day for the same satellite constellation than on the day when explosive activity starts.

Appendix C

Eruption Pre-warning with High-rate GPS: The Case of Grímsvötn Volcano, Iceland, 2011[1]

A GPS receiver at Mt. Grímsfjall, Iceland, recorded the May 21-28, 2011 eruption of Grímsvötn volcano. Co-located with the GPS site GFUM is an electronic tiltmeter. The GPS station GFUM is located about 6 km from the vent to the east on a nunatak surrounded by the Vatnajökull ice cap. Processing the data as detailed in Hreinsdóttir et al. (2012), we get the time series shown in Figure C.1 for the horizontal component of GFUM on May 21, 2011. The eruption started, i.e. magma breached the Earth's surface and erupted explosively, at about 18:56 to 19:00 as indicated by the red vertical bar in Figure C.1.

Interestingly, GFUM begins moving towards the north-west about 50 minutes before the surface is breached by the magma. This is consistent with a decrease in pressure of a shallow magma chamber which acts as an inflation source in between eruptions (Sturkell et al., 2011). A dike propagating from this reservoir effectively lowers the pressure as material is evacuated from the chamber into the dike, which agrees with the observations in the time series (Figure C.1).

Owen et al. (2000) report 8 hours of pre-eruptive baseline lengthening, i.e. rift extension, for two sites crossing a fissure that opened during an eruption at Kilauea Volcano, Hawaii, on January 30, 1997. Instead of solving for positions epoch by epoch, they solved for station positions in 48 minute intervals. They observe, similar to Figure C.1, rapid displacement rates at the onset and a decay of the rates even before the eruption, which suggests non-constant/decaying magma pressure during dike growth (Owen et al., 2000). At Grímsvötn this is consistent with a dike originating from a pre-exising, over-pressurized reservoir.

The co-located tilt meter shows similar motion (Figure C.2), including all observed rate changes. Having the GPS data rotated into source normal, i.e. radial, and transverse component shows that the major deformation source is the deflating magma chamber to the north-west. Due to the geometry and location of the dike, the GPS station GFUM is

---

[1]My analysis of the high-rate GPS data is part of a planned submission as Hreinsdóttir, S., F. Sigmundsson, M. Roberts, H. Björnsson, R. Grapenthin, Þ. Arason, Þ. Árnadóttir, J. Hólmjárn, H. Geirsson, R. Bennett, B. Oddsson, M. T. Guðmundsson, B. G. Ófeigsson, T. Villemin, and E. Sturkell, A High Rate Geodetic Magma Chamber Meter and the Evolution of the Grímsvötn 2011 Eruption

effectively blind to deformation caused by this source, or picks up only very little displacements as reflected in the transverse component. In a multi-source scenario, the transverse component would show a greater signal.

Combining the tilt and deformation data enables Sigmundsson et al. (2011) to solve for the free parameters of a deflating pressure point source from one single observation point. They estimate a depth of 1.8±0.2 km and a horizontal distance of 3.6±0.3 km between GPS station and source. Considering that the GPS station is about 6 km from the source, we can estimate the horizontal distance between source and vent as roughly 5.3 km, which results in a distance of about 5.6 km from the pressure source to the surface at the vent. If the dike traveled on a straight line during the roughly 50 min of precursory deformation, it propagated at about 110 m/min. However, one would assume a slightly curved propagation path following the local stress field, which would yield a slightly slower propagation velocity.

Bibliography

Hreinsdóttir, S., Grapenthin, R., Sigmundsson, F., Roberts, M. J., Holmjarn, J., Geirsson, H., Arnadottir, T., Bennett, R. A., Villemin, T., Ofeigsson, B. G., Sturkell, E. C., 2011. The 2011 Grímsvötn Eruption From High Rate Geodesy, Abstract V34B-02 presented at 2011 Fall Meeting, AGU, San Francisco, Calif., 5-9 Dec.

Hreinsdóttir, S., Sigmundsson, F., Roberts, M., Bjornsson, H., Grapenthin, R., Arason, T., Arnadóttir, T., Hólmjarn, J., Geirsson, H., Bennett, R., Oddsson, B., Gudmundsson, M. T., Ofeigsson, B. G., Villemin, T., Sturkell, E., 2012. A High Rate Geodetic Magma Chamber Meter and the Evolution of the Grímsvötn 2011 Eruption, in prep.

Owen, S., Segall, P., Lisowski, M., Miklius, A., Murray, M., Bevis, M., Foster, J., 2000. January 30, 1997 eruptive event on Klilauea Volcano, Hawaii, as monitored by continuous GPS. Geophys. Res. Lett. 27 (17), 2757–2760.

Sigmundsson, F., Hreinsdóttir, S., Bjornsson, H., Arason, T., Grapenthin, R., Roberts, M. J., Holmjarn, J., Geirsson, H., Arnadottir, T., Bennett, R. A., Oddsson, B., Gudmundsson, M. T., Ofeigsson, B. G., Villemin, T., Sturkell, E., 2011. Grímsvötn 2011 Explosive Eruption, Iceland: Relation between Magma Chamber Pressure Drop inferred from High Rate Geodesy and Plume Strength from Radar Observations, Abstract V41E-08 presented at 2011 Fall Meeting, AGU, San Francisco, Calif., 5-9 Dec.

Sturkell, E., Sigmundsson, F., Einarsson, P., Hreinsdottir, S., Villemin, T., Geirsson, H., Ófeigsson, B. G., Jouanne, F., Bjornsson, H., Gudmundsson, G. B., Pálsson, F., 2011. Deformation cycle of the Grímsvötn sub-glacial volcano, Iceland, measured by GPS, Abstract V31H-04 presented at 2011 Fall Meeting, AGU, San Francisco, Calif., 5-9 Dec.
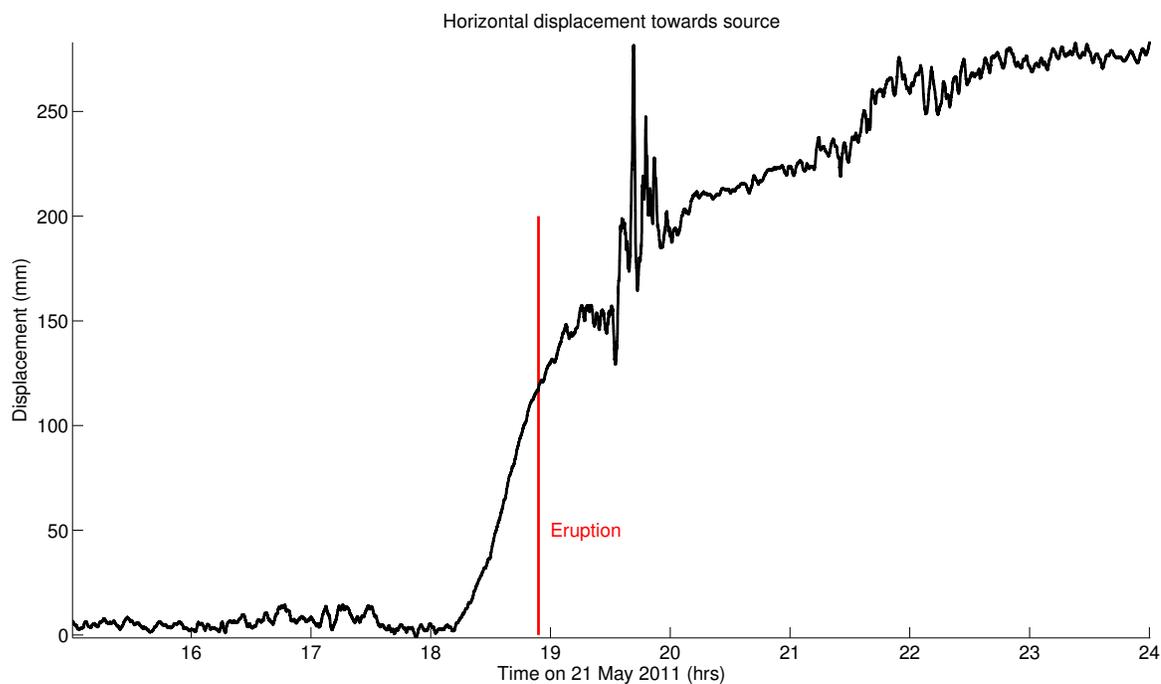
Figure C.1: Figure from Hreinsdóttir et al. (2011) – Horizontal displacement towards shallow magma reservoir at Grímsvötn as recorded by GPS. Motion suggests quick pressure drop about 50 minutes before the magma reaches the surface. Increased noise in the time series after the onset of explosive activity suggests plume interference with the GPS signal coming from the satellites.
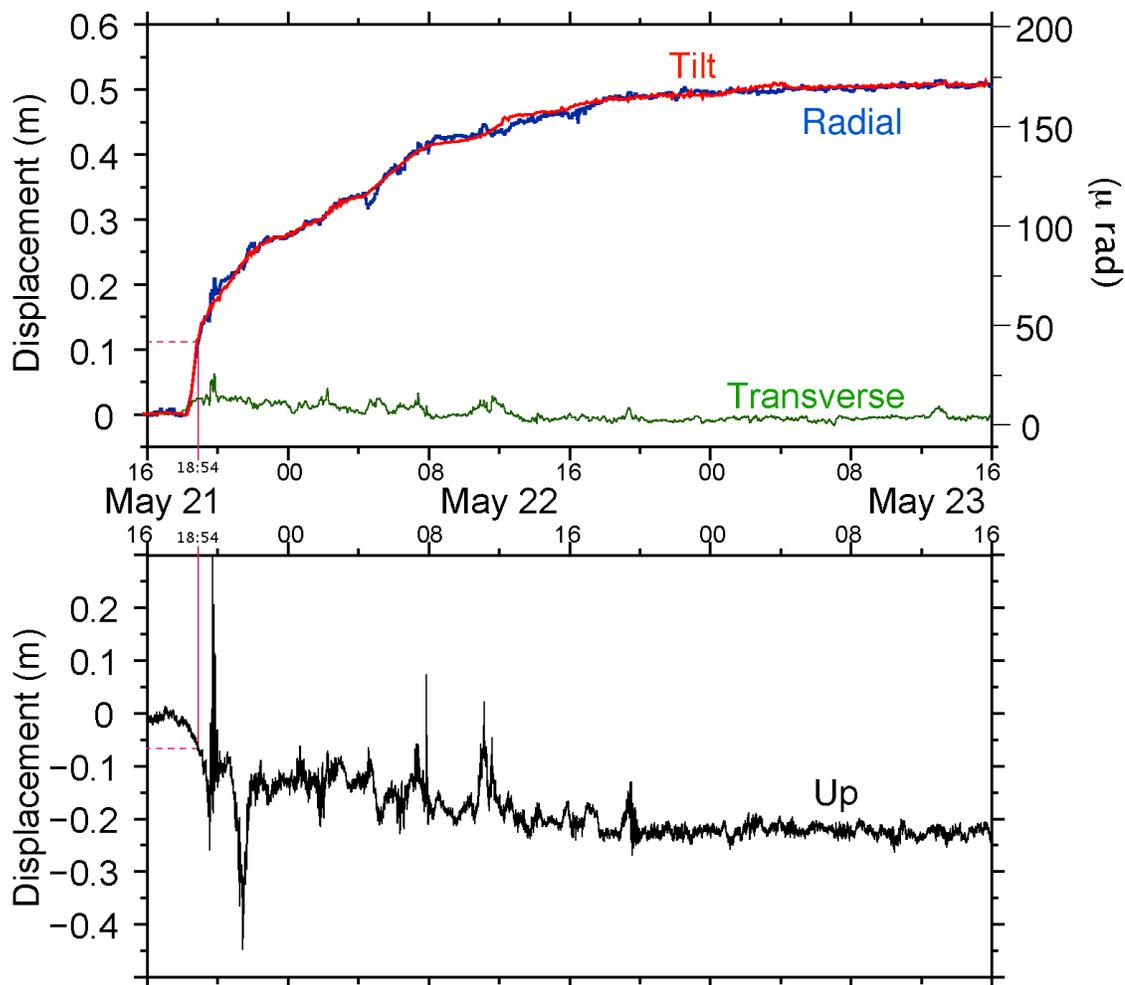
Figure C.2: Figure from Hreinsdóttir et al. (2011) – GPS timseries (blue, green, black) with 15 s smoothing filter applied and Tilt (red) rotated into radial and transverse components (source is at N38.4±0.5° W (Hreinsdóttir et al., 2012)). Tilt and GPS agree well in terms of deformation rate changes. Transverse GPS component shows little deformation suggesting the station suffers from very little to no deformation due to the dike extrusion. The time of the eruption is marked by the vertical red bar.

Appendix D

Computer Programming for Geosciences: Teach Your Students How to Make Tools[1]

When I announced my intention to pursue a Ph.D. in geophysics, some people gave me confused looks, because I was working on a master's degree in computer science at the time. My friends, like many incoming geoscience graduate students, have trouble linking these two fields. From my perspective, it is pretty straightforward: much of geoscience evolves around novel analyses of large data sets that require custom tools –computer programs– to minimize the drudgery of manual data handling; other disciplines share this characteristic.

While most faculty adapted to the need for tool development quite naturally, as they grew up around computer terminal interfaces, incoming graduate students lack intuitive understanding of programming concepts such as generalization and automation. I believe the major cause is the intuitive graphical user interfaces of modern operating systems and applications, which isolate the user from all technical details. Generally, current curricula do not recognize this gap between user and machine. For students to operate effectively, they require specialized courses teaching them the skills they need to make tools that operate on particular data sets and solve their specific problems. Courses in computer science departments are aimed at a different audience and are of limited help.

In 2009, my adviser, Jeff Freymueller, and I began to experiment with a course on programming for geoscience graduate students in our department at the University of Alaska Fairbanks. This emerged from a fortunate mix of people in one room: a graduate student in need; me, already thinking about such a course; and supportive and aware faculty. We now have gone through three iterations of this experiment. Our course goals are ambitious for a one-semester, two-credit course. We learned a lot from our many mistakes, and I want to share some of our experiences and encourage other institutions to follow along. Specific programming languages and tools vary by discipline and department, but the general ideas from our course could be applied widely. The overarching main points we believe such a course should touch on are as follows:

Repetitive work is for machines. Students need to realize that a problem is worth being

---

[1]Published as EOS Forum Article: Grapenthin, R. (2011), Computer programing for geosciences: Teach your students how to make tools, Eos Trans. AGU, 92(50), 469, doi:10.1029/2011EO500010.

solved once. Exactly once. Yet there are students manually laboring through identical procedures on a daily basis. We want them to understand that breaking down a complex problem into simple tasks, writing out the respective steps, testing them individually, and finally bundling them into one command is of great value and is time well invested. From this we advance to generalizing specific solutions such that their tool tackles an array of problems. For example, suppose one has a tool that analyzes a day's worth of data for one sensor. We want students to ask how this tool can be used to treat all available sensors on all days. Trying to think of such a configuration is a worthwhile yet challenging exercise. The solution to questions like this is abstract and entirely free of code, but it establishes the fundamental concept of having computers do the work while you are out for an afternoon run.

Understand fundamental principles. No single programming language is the ultimate tool for all problems. Handing your students one tool to solve a specific task will be a great quick fix until a different kind of problem emerges, rendering this tool a poor fit. Exposing students to a small variety of programming languages and the connecting fundamental principles loosens the tension a new syntax brings and hands them abilities they crave. Comprehension of the concepts of variables, functions, and flow control gives students sufficient momentum and the ability to transition to whatever shiny new language comes around in the future. While object-oriented programming certainly deserves consideration because it enables wonderful software design, it seems impossible to teach such advanced concepts well in a few lectures and labs, so we decided against including it in our course.

Organize data consistently. Data-related programming revolves around traversing directories, picking files, reading data, processing data, and writing out results. To have a computer operate effectively and keep coding efforts under control, a consistent naming scheme for files and directories is crucial. Imagine needing all available data for 23 May 2012. It's easy if all files carry the date in their name in a consistent format, say, 20120523. Consistent data archiving allows your program to find files in a minimal number of steps. Admittedly, this is pretty straightforward, but students are so accustomed to the fact that they can easily recognize a multitude of date formats that they do not realize how hard it is for a machine to do so.

Create legible, reproducible figures. In many disciplines the figure is the ultimate conveyor

of achievements, summarizing findings (we think) in an accessible way. A lot of effort goes into figure creation. Yet this should not be repeated whenever new data come around. Once created, a figure is a solved problem. Hours wasted on re-creating it indicate the use of the wrong tool. Similarly, illegible axis labels or poor color schemes should prompt everyone at least to wonder about a tool's capabilities and, if necessary, switch to a tool that offers the required level of freedom. Sadly, more often than not, this is not done. Conveying these thoughts is not unique to us; we join the choir of people like Edward Tufte and Jon Claerbout, scientists who are calling for sensible and reproducible visualization of data.

The course has been well received by both students and faculty in our department. Several biology students have taken the class in the last two iterations, which shows that the demand for the class extends beyond geoscience. Apart from classic lecture settings, three core ideas are responsible for this success:

Provide guided practical application. Probably the biggest mistakes we made were to assume too much prior knowledge and to provide too little individualized guidance. We assumed we were instructing experienced students, but in reality they were entering a new field and were beginners on this topic. Although banging your head against a wall is an integral part of computer programming, it is necessary to keep a healthy balance between frustration and gratification; this makes a controlled lab environment indispensable. It is of great help to demonstrate individually how to solve the mostly minor problems encountered when working through problem sets. Most of this knowledge seems so deeply ingrained in the mind of experienced programmers that it appears natural. Conveying these techniques and simple concepts is critical and is impossible in a pure lecture setting.

Solve student-specific problems. We assign projects that are ideally related to a student's thesis work so that they include course concepts in their daily routine. Here the key to success is heavy mentoring, which includes time-intensive code review. Given the diversity of student research, this is hard, but it comes with the tremendous gratification of engaging education that sticks with the student.

Demonstrate problem solving. A final point that inspires significant progress is "live coding." I pick a simple problem and think it through but write the actual program with the students in class. Naturally, this brings embarrassment and high entertainment po-

tential. Between bouts of laughter, students break down complex problems into simpler tasks, learn to read error messages, see the value of search engines in debugging, and get a feeling for connecting the dots.

As a result of the course, our students make enormous strides in their programming skills and their confidence to take on problems that require those skills. We see them apply these techniques in their research and in other courses. Other course instructors will be able to assume that students who have taken our class have basic programming knowledge. This allows those instructors to use computational exercises to teach geoscientific concepts rather than programming. Our experience gives us confidence that our students will leave behind a trace of useful tools. Some already advance their community by making their work freely available; some consider publishing papers about their tools. This is surely more desirable than stacks of sticky notes. The hope is that these ideas will be fresh in your mind as you consider coming curriculum changes.